

Dissertation  
submitted to the  
Combined Faculties for the Natural Sciences and for Mathematics  
of the Ruperto-Carola University of Heidelberg, Germany  
for the degree of  
Doctor of Natural Sciences

presented by  
Shyamal Chatterjee, MSc  
born in: Burdwan, India  
Oral examination: 17.01.2007



**Measurement of the Wavelength of the  
Lyman- $\alpha_1$  Transition of  $^{208}\text{Pb}^{81+}$  Using  
FOCAL Spectrometers**

Referees:

Prof. Dr. Dieter Liesen  
Prof. Dr. Joachim Ullrich



**Measurement of the Wavelength of the Lyman- $\alpha_1$  Transition of  $^{208}\text{Pb}^{81+}$  Using FOCAL Spectrometers** - The goal of the experimental study is the determination of the 1s Lamb shift of a one-electron, very heavy ion with high precision by an accurate spectroscopy of the corresponding Lyman- $\alpha$  transitions. Unlike low- $Z$  systems the quantum electrodynamical (QED) calculations using perturbation theory based on the expansion parameter  $Z\alpha$  are no longer applicable for high  $Z$  systems and therefore all orders of  $Z\alpha$  are included in the calculations. The present accuracy of the calculations is of the order of 1 eV. Thus the measurements of the Lyman- $\alpha$  transitions aim to achieve an uncertainty, which is sensitive to 1 eV or below. Such accurate measurements require high resolution in the techniques of x-ray spectroscopy. For this purpose a couple of "FOcusing Compensated Asymmetry Laue (FOCAL)" spectrometers has been developed at GSI and they have been employed in the first production run in March 2006. The FOCAL spectrometers are optimally adapted to the experimental conditions at the Experimental Storage Ring (ESR) at GSI, including intrinsic Doppler corrections, a trade off between resolution and efficiency as well as incorporating latest detection technology with two large-area position-sensitive microstrip germanium detectors. This PhD thesis includes the physics of the FOCAL spectrometer and the results obtained after a preliminary analysis of the experimental data.

**Messung der Wellenlänge des Lyman- $\alpha_1$  Übergang in  $^{208}\text{Pb}^{81+}$  mit den FOCAL Spektrometern** - Ziel der experimentellen Untersuchung ist die Bestimmung der 1s-Lambverschiebung in sehr schweren Ein-Elektron Ionen durch eine sehr genaue Messung der Wellenlänge der Lyman- $\alpha_1$  Übergänge. Im Gegensatz zu Ionen mit niedriger Kernladungszahl  $Z$  können quantenelektrodynamische Rechnungen für sehr schwere Ionen nicht mehr in Störungstheorie mit dem Parameter  $Z\alpha$  durchgeführt werden, vielmehr ist eine Rechnung in allen Ordnungen dieses Parameters erforderlich. Die Genauigkeit solcher Rechnungen liegt zurzeit in der Größenordnung von 1 eV und darunter. Dementsprechend zielen die Experimente letztendlich auf solch eine Genauigkeit ab. Zu diesem Zweck wurde an der GSI ein Paar von "FOcusing Compensated Asymmetry Laue (FOCAL)" Spektrometern entwickelt, die zum ersten Mal bei einer Strahlzeit im März 2006 eingesetzt wurden. Die FOCAL-Spektrometer sind optimiert für die experimentellen Bedingungen am Speicherring ESR bei der GSI, namentlich für Doppler-Korrekturen und den Kompromiss zwischen Nachweiswahrscheinlichkeit und Auflösungsvermögen. Sie bedingen den Einsatz von unlängst entwickelten, großflächigen, zwei-dimensional ortsauflösenden Röntgendetektoren. Diese Doktorarbeit beinhaltet die Physik der FOCAL-Spektrometer und den Zwischenstand der Auswertung der bisher am ESR gewonnenen experimentellen Daten.



# Contents

<b>1</b>	<b>Introduction</b>	<b>3</b>
<b>2</b>	<b>The Structure of One-electron System</b>	<b>5</b>
2.1	The Atomic Structure . . . . .	5
2.1.1	The Classical Lamb Shift . . . . .	7
2.1.2	The Consequences of the Lamb-Retherford Experiment . . . . .	8
2.2	The Status of 1s Lamb Shift . . . . .	14
<b>3</b>	<b>The Accelerator Facility and Experimental Environment at GSI</b>	<b>19</b>
3.1	The ESR . . . . .	19
3.1.1	The Electron Cooler . . . . .	22
3.1.2	The Internal Gas-jet Target . . . . .	22
3.1.3	X-ray Spectroscopy at the Internal Gas-jet Target of the ESR . . . . .	25
3.1.4	Charge Exchange Processes in Gas Target . . . . .	25
3.2	Aspects of 1s Lamb Shift Measurement at the Gas Target . . . . .	30
<b>4</b>	<b>The FOCAL Spectrometer</b>	<b>33</b>
4.1	The FOCAL Geometry . . . . .	33
4.2	The Technical Lay-out of FOCAL . . . . .	39
4.2.1	The X-ray Sources . . . . .	39
4.2.2	The Background Shielding . . . . .	42
4.2.3	The Crystal Component . . . . .	42
4.2.4	The Polychromatic Focus . . . . .	44
4.2.5	The Detection Systems . . . . .	45
4.2.6	The Two-dimensional Microstrip Detector . . . . .	45
4.2.7	The One-dimensional Microstrip Detector . . . . .	49
<b>5</b>	<b>The Experiment, Data Analysis and Interpretations</b>	<b>51</b>
5.1	The Spectrometer Alignment . . . . .	51
5.1.1	The Doppler Color Mixing Rule . . . . .	51
5.2	The Experimental Arrangement . . . . .	55
5.3	The Data Analysis of FOCAL1(2D) Spectrometer . . . . .	57
5.3.1	The Analysis of the Calibration Spectrum . . . . .	57

5.3.2	The Analysis of the Online Measurement . . . . .	62
5.4	The Data Analysis of FOCAL2(1D) Spectrometer . . . . .	73
5.5	The Energy Centroid . . . . .	77
5.5.1	The FOCAL1(2D) Spectrometer . . . . .	79
5.5.2	The FOCAL2(1D) Spectrometer . . . . .	80
5.5.3	The Mean Energy Centroid . . . . .	80
5.6	The Estimation of Errors . . . . .	81
5.6.1	The FOCAL1(2D) Spectrometer . . . . .	81
5.6.2	The FOCAL2(1D) Spectrometer . . . . .	82
5.6.3	The Total Error of the Ly $\alpha_1$ Energy . . . . .	83
5.7	The Energy Dispersion . . . . .	84
<b>6</b>	<b>Conclusion and Outlook</b>	<b>85</b>

# Chapter 1

## Introduction

Hydrogen like ions are the simplest atomic systems. Transitions in these one-electron ions give precise information on the atomic structure and the fundamental principles involved in the theory of the interaction between electrons and electromagnetic fields. Beside the relativistic effects the quantum electrodynamic (QED) and the nuclear effects have to be included for an exact description of the atomic structure. In light systems, like atomic hydrogen, the influence of QED effects has been tested with unprecedented accuracy [1, 2]. In such systems the coupling constant  $Z\alpha$  is the expansion parameter, where  $Z$  is the nuclear charge number and  $\alpha$  the fine structure constant. However, for high- $Z$  systems, where ordinary perturbation theory is no longer acceptable since the parameter  $Z\alpha$  approaches unity, therefore, all orders of  $Z\alpha$  are incorporated into the calculation and for such systems the validity of the QED theory is yet to be tested precisely. Thus the 1s Lamb shift, which is the difference between the real binding energy (including the QED and nuclear effects) and the energy eigen value obtained from the Dirac theory for a point-like nucleus of the 1s-energy level of high- $Z$  ions can give direct access to probe the QED contributions in the presence of the strong electromagnetic field of the nucleus.

With the advent of generous heavy ion sources like the Experimental Storage Ring (ESR) at GSI [3, 4] and Super-Electron Beam-Ion-Trap (SuperEBIT) at Livermore [5] such measurements are feasible and parallel rapid progress in theoretical calculations are giving it a challenging edge. High precision Lamb shift experiments have been carried out at these facilities for a number of hydrogen-like ions. So far the most accurate 1s Lamb shift determination for uranium ( $Z = 92$ ) has been carried out at the electron cooler at the ESR using x-ray spectroscopic techniques and yielded a value of  $460.2 \pm 4.6$  eV [6], which showed a 2% sensitivity to the first order in  $\alpha$  of the QED contributions. However, the second order in  $\alpha$  contributes only of about 1 eV. Therefore, to be sensitive to the second order one needs an uncertainty in 1s Lamb shift determination of 1 eV or below. An accurate knowledge about the validity of QED in very heavy systems is also necessary for the exploration of new physics beyond QED.

In order to achieve an uncertainty of  $\pm 1$  eV in the Lamb shift experiment an improved resolution in the x-ray spectroscopy is essential. For this purpose two different set-ups, namely a pair of FOCAL spectrometer and a calorimeter detector, have been developed and employed at the gas-jet target in the ESR. In a production run in March 2006 both the instruments have been exploited. The FOCAL spectrometers are optimally adapted to the experimental conditions at the ESR, including intrinsic Doppler corrections, a trade off between resolution and efficiency as well as incorporating latest detection technology with two large-area position-sensitive microstrip germanium detectors. In this thesis work the physics of the FOCAL spectrometer and the results obtained in a preliminary analysis of the experimental data are included. The chapters are arranged in the following way.

In **Chapter 2** a brief review of the historical developments of the theory of atomic structure and the experimental facts leading to a more refined theory of QED is discussed. The QED corrections (the self energy and the vacuum polarization) in the first order and the second order in  $\alpha$  and the nuclear effect corrections to the Lamb shift are depicted. Finally the status of 1s Lamb shift experiment and theory is presented. In **Chapter 3** an overview about the accelerator facilities of GSI is given. The FOCAL experiment was performed at gas-target in the Experimental Storage Ring (ESR). A brief description of the two experimental sections, the Electron Cooler and the gas-target is presented. The different mechanisms leading to electron capture from gas-targets to highly charged ions are discussed. Finally, the aspects of a 1s Lamb shift experiment at the gas-target are discussed. The **Chapter 4** includes the detailed physics and design concepts of the FOCAL spectrometer. In the first section of this chapter, the physics of a bent crystal geometry is described and in the following section the special design of the FOCAL spectrometer to cope up with the experimental environment at the gas-target is accounted. The FOCAL spectrometers have been equipped with recently built position-sensitive microstrip germanium detectors. A brief description of the detectors and the charge sharing phenomenon are given at the end of this chapter. In **Chapter 5** the experiment, data analysis and interpretations are presented. The data analysis for the two FOCAL spectrometers are given in two separate sections. Due to the relativistic speed of the ion-beam, the spectral lines show strong Doppler rotations, which is explained in the data analysis section of the FOCAL1(2D). For both the detectors (the one-dimensional and the two-dimensional) the reconstruction of the split events are shown. Finally from the dispersion relation of the spectrometer the determination of the energy centroid of the Lyman- $\alpha_1$  is given and the errors are tabulated. A conclusion and outlook is the content of **Chapter 6**.

# Chapter 2

## The Structure of One-electron System

### 2.1 The Atomic Structure

In the year 1911, Ernest Rutherford developed the first coherent explanation of the structure of an atom from the famous experiment of the alpha particle scattering from a gold foil. However, it had the serious problem of the stability of the atomic structure due to the continuous electromagnetic radiation emitted by the orbiting electron. This difficulty was solved by Niels Bohr (1913), who applied the quantum theory developed by Max Planck and Albert Einstein to the atomic structure problem. Bohr proposed that electrons could circle a nucleus without radiating energy only in orbits for which their orbital angular momentum was an integral multiple of Planck's constant  $h$  divided by  $2\pi$ . The discrete spectral lines emitted by an atom were produced by electrons jumping from allowed orbits of higher energy to those of lower energy, the frequency of the photon emitted being proportional to the energy difference between the orbits. For the first time the energy of an atomic level was given by this theory by  $E_n = -Z^2hcR/n^2$ , where  $Z$  is the nuclear charge number of a point like nucleus,  $n$  the principle quantum number,  $R$  the Rydberg constant and  $c$  the speed of light. Although Bohr's theory accounted for many of the observed lines in the hydrogenic spectrum, it could not explain the close doublets in the spectrum, the so called "fine structure". In 1916, Sommerfeld introduced the relativistic variation of mass with velocity, which gave rise to a dependence of the energy on the eccentricity of the orbit. For example for the  $n = 2$  level the circular ( $l = 1$ ) and elliptical orbit ( $l = 0$ ) differed by  $\Delta E = \alpha^2 Z^4 hcR/16$  [8], where  $\alpha = e^2/\hbar c$  is the fine structure constant. This energy difference however agreed only qualitatively with the doublet separation but not quantitatively. There were several other drawbacks: The Bohr-Sommerfeld theory does not tell how to calculate the rate at which a transition occurs between two states and the intensity of the spectral lines. When

applied to the atoms, the theory was only partly successful for one-electron atoms but failed badly even when applied to the neutral He atom.

Much effort was expended in attempts to develop a quantum theory, which would be free of these problems. In 1925, Erwin Schroedinger developed the theory of quantum mechanics (the wave mechanics) incorporating the de Broglie postulate. The stationary Schroedinger equation is written as

$$-\frac{\hbar^2}{2m} \nabla^2 \psi(\vec{r}) + V(\vec{r})\psi = E\psi(\vec{r}) \quad (2.1)$$

where  $\psi$  is the wave function of a particle of mass  $m$  which is in the potential  $V$  (in an atom it is the Coulomb potential). This theory without electron spin accounted for the energy levels of the atom that are observed in spectroscopic measurements of moderate resolution. The fine structure can be explained almost completely by adding to this equation corrections for the spin-orbit interaction and for the relativistic dependence of mass on velocity. Besides one-electron systems the Schroedinger theory is accurate enough to explain every important features of multielectron atoms. The atomic transition rates and selection rules are partially explained by this theory. Note that an independent and parallel work was done by Heisenberg, who formulated matrix mechanics, which ultimately led to the same result as the Schroedinger theory. In spite of a major success of the Schroedinger theory, it is not invariant under the Lorentz transformations of Special Relativity.

A break thorough came in 1928, when Dirac successfully formulated the relativistic equation for an electron moving in a Coulomb field, which automatically guaranteed the correct mass variation, spin and magnetic moment of the electron. The Dirac equation is given by

$$[c\vec{\alpha} \cdot \vec{p} + \beta mc^2 + V(\vec{r})]\psi(\vec{r}) = E\psi(\vec{r}) \quad (2.2)$$

where  $\vec{p}$  is the linear momentum of the electron,  $V(\vec{r})$  the Coulomb potential of the nucleus,  $\vec{\alpha}$  and  $\beta$  are the  $4 \times 4$  Dirac matrices. For a point like nucleus the analytical solution of this equation yields the energy of a bound state with the quantum numbers  $(n, j)$

$$E_{nj} = mc^2 \left[ 1 + \left( \frac{\alpha Z}{n - (j + 1/2) + \sqrt{(j + 1/2)^2 - (\alpha Z)^2}} \right)^2 \right]^{-1/2} \quad (2.3)$$

$$= mc^2 \left[ 1 - \frac{(\alpha Z)^2}{2n^2} - \frac{(\alpha Z)^4}{2n^2} \left( \frac{n}{j + 1/2} - \frac{3}{4} \right) + \dots \right] \quad (2.4)$$

where  $j = l \pm 1/2$  is the total angular momentum quantum number of the electron,  $\alpha$  the fine structure constant and  $mc^2$  the rest energy of the electron. Eq. 2.3 gives the same energy eigen value for the states with the same  $n$  and  $j$  values. The Dirac equation explains successfully the fine structure observed in atomic spectral

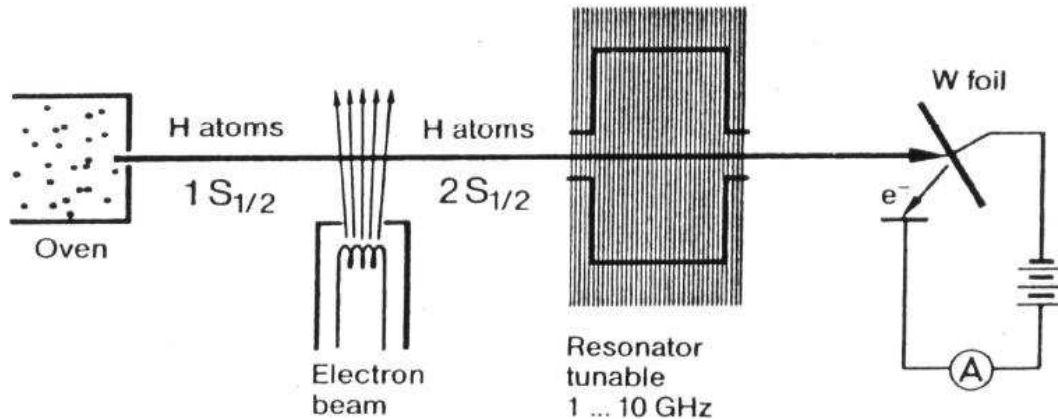


Figure 2.1: Configuration of the Lamb-Retherford experiment (1947).

lines. It also provides the theoretical underpinning for the Uhlenbeck-Goudsmit model of the spin of the electron. Two of the four solutions of the equation correspond to the two spin states of the electron. The other two solutions make the prediction that there exists an infinite set of quantum states in which the electron possesses negative energy. This strange result led Dirac to predict, via a remarkable hypothesis known as "hole theory," the existence of positively-charged electrons, which was verified by the discovery of the positron in 1932 [10].

### 2.1.1 The Classical Lamb Shift

An enormous amount of effort was spent during the 30s and 40s in spectroscopic work to establish the extent of agreement of the observational data with the prediction of the Dirac theory. In between 1932 and 35 Betz [11] and Hasse [12] independently measured the transition between the  $2s_{1/2}$  or  $2p_{1/2}$  and the  $2p_{3/2}$  states of the hydrogen atom, which confirmed the degeneracy of the  $2s_{1/2}$  and  $2p_{1/2}$  states and failed to show any difference because of the insufficient experimental arrangements or techniques. During 1946 and 1947 Lamb and Retherford performed a similar measurement using more refined techniques. The scheme used in their advanced experiment in 1947 is shown in Fig. 2.1 [13]. They prepared a beam of hydrogen atoms in the  $1s_{1/2}$  ground state. The beam was bombarded with electrons and as a result some of the atoms are excited to the  $2s_{1/2}$  state. Electric dipole transitions from this state that go directly to the  $1s_{1/2}$  ground state are prohibited by selection rules resulting in a very long (approximately 0.1 second) lifetime of the  $2s_{1/2}$  state. The atoms then passed through a region where they were exposed to electromagnetic radiation of a tunable frequency. If

the energy of the radiation equals a possible energy difference between the  $2s_{1/2}$  and  $2p_{1/2}$  states, transitions between these states would be induced and once an atom is in the  $2p_{1/2}$  state it decays by an E1-transition to the ground state with a lifetime of  $10^{-9}$  s. After passing through the region with electromagnetic radiation in the microwave region, the atoms struck a tungsten foil. Upon striking the foil, the atoms which were still in the  $2s_{1/2}$  state decayed to the ground state and in doing so they liberated electrons from the foil by Auger emission. By measuring the emission current from the foil with the electromagnetic radiation turned on (fewer electrons liberated) and with the radiation turned off (more electrons liberated), Lamb and Retherford were able to determine the energy difference between the  $2s_{1/2}$  and  $2p_{1/2}$  states. Their measurements indicated this difference to be close to 1000 MHz, which corresponds to an energy of about  $4.4 \mu\text{eV}$  and that represented a relative correction of  $10^{-6}$  to the binding energy of  $2s_{1/2}$ . This shift is termed as classical Lamb shift.

### 2.1.2 The Consequences of the Lamb-Retherford Experiment

The above mentioned experiment showed that although the  $2s_{1/2}$  and  $2p_{1/2}$  levels had the same  $n$  and  $j$  values, still they made a departure from Dirac's prediction. The impact of the result was tremendous and led to a re-shaping and re-evaluation of the theory of the interaction between an electron and electromagnetic radiation. In the same year Bethe tried non-relativistic calculations to explain this splitting by the electron self-interaction [14]. This was the first QED correction. Followed by that successful relativistic calculations were formulated by Dyson, Feynman, Schwinger and Tomonaga.

In general the Lamb shift is defined as the shift of an atomic energy level due to the quantum electrodynamical (radiative corrections) and nuclear effects beyond the prediction of Dirac's theory for a point-like nucleus (see Fig. 2.2). The main radiative corrections to the binding energy of an electron are self-energy and vacuum polarization and they depend on the parameters  $\alpha$  and  $Z\alpha$ . The above mentioned corrections are discussed in the following subsections.

#### The Self-energy

Part (a) of Fig. 2.3 shows the Feynman diagram for the self-energy of an electron moving in the field of a nucleus. The self-energy in QED means the emission and re-absorption of a virtual photon by an electron (fermion in general) in accordance with Heisenberg's uncertainty relation. While the photon is present, the electron can be in any energy state without violating energy conservation. After re-absorption, the original state is present again. As long as the electron is in the intermediate state, its interaction with the external field results in an energy shift of the original state. The most accurate calculations of the self

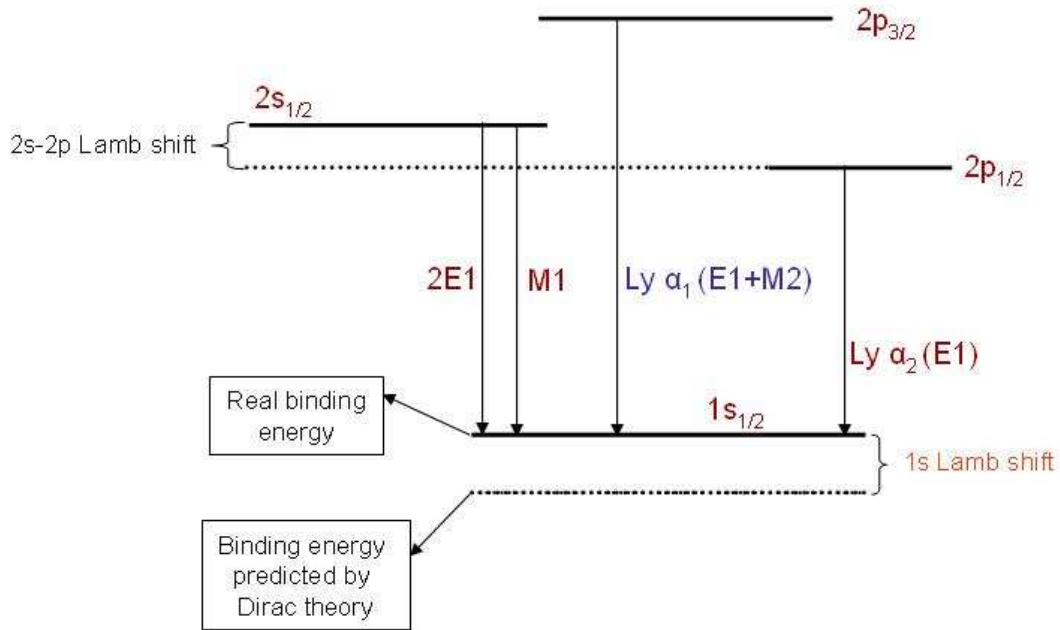


Figure 2.2: A level scheme of a H-like system as predicted by the Dirac theory together with energy level shifts which are subsumed as Lamb shifts. The very small Lamb shifts of p-states are ignored. In addition, the different types of transition modes are indicated. The electric dipole (E1) rate is proportional to  $Z^4$ , the magnetic dipole transition (M1) rate proportional to  $Z^{10}$ , 2E1 transition rate to  $Z^6$  and the magnetic quadrupole (M2) rate scales with  $Z^8$ . For hydrogen-like uranium ( $Z = 92$ ) the E1 transition rate amounts to  $3.92 \times 10^{16} s^{-1}$ , whereas the M2 rate of  $2.82 \times 10^{14} s^{-1}$  contributes less than 1% to the total decay rate [15]. For the same ion the M1 rate is  $1.95 \times 10^{14} s^{-1}$  [16] and the 2E1 rate of about  $5 \times 10^{12} s^{-1}$  [17].

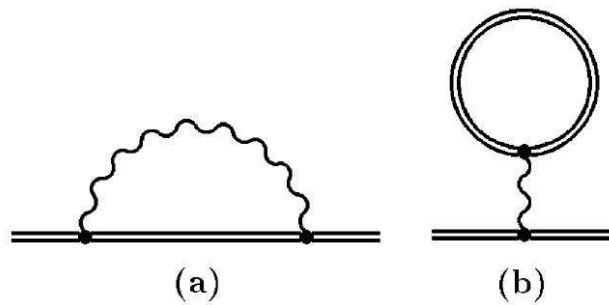


Figure 2.3: The self-energy (SE) (a) and vacuum polarization (VP) (b) diagrams of order  $\alpha$ . The double lines indicate electrons and positions in the field of a nucleus and wavy lines the virtual photons.

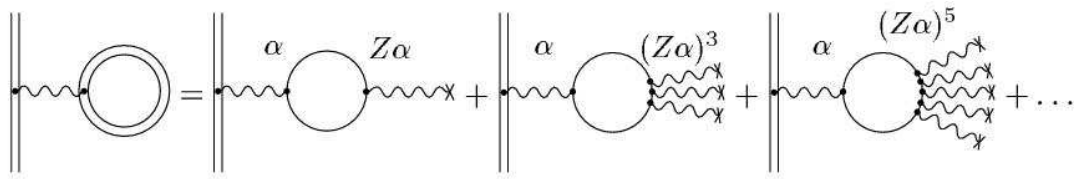


Figure 2.4: Expansion of the vacuum polarization loop into different powers of  $Z\alpha$  [24].

energy contribution have been performed by Mohr [18, 19] and by Indelicato and Mohr [20] for point-like nuclei, and by Mohr and Soff [21] for extended nuclei. A highly efficient procedure for the evaluation of the self-energy correction suitable for arbitrary electron states was developed in Ref. [22].

### The Vacuum Polarization

Part (b) of Fig. 2.3 shows the Feynman diagram for the vacuum polarization. It describes the interaction of an electron with virtual electron-positron pairs, which can be thought to be present in the vacuum for short times without violating Heisenberg's uncertainty relation. If external fields are present, these virtual pairs act like a polarized medium. Therefore, the Coulomb interaction of the nucleus with the electron is modified which leads to an energy shift compared to the pure Coulomb potential energy eigenvalue. The bound electron loop in (b) of Fig. 2.3 can be expanded into powers of  $Z\alpha$  as shown in Fig. 2.4. The first term of the expansion is called the Uehling contribution and all higher order terms as Wichmann-Kroll contribution. Only loops with an even number of photon lines contribute to the expansion according to the Furry theorem [24]. The dominating Uehling potential causes the vacuum polarization effect to be attractive, therefore, the binding energy of the electron increases. However, the Wichmann-Kroll contribution shows an opposite behavior. The Wichmann-Kroll part was first calculated by Soff and Mohr [25] for extended nuclei. Persson et al. [26] calculated this effect for some specific ions to higher precision.

In light systems, the standard theoretical approach to calculate QED contribution is perturbation theory with the coupling constant  $Z\alpha$  being the expansion parameter. This method was extremely successful for systems like hydrogen and

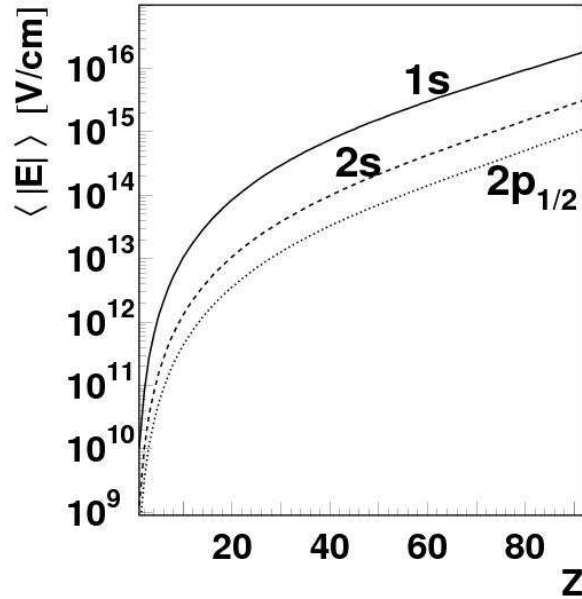


Figure 2.5: Expectation value of electric field strength for the lowest lying bound states in H-like atoms with nuclear charge number  $Z$  [24].

helium. However, rapid progress of experimental spectroscopy makes nowadays an accurate experimental investigation of heavy one- and few-electron systems up to uranium possible. In such heavy ions the parameter  $Z\alpha$  approaches unity. Thus, a theoretical treatment for high- $Z$  ions is necessary, which includes all higher orders in  $Z\alpha$  simultaneously [29].

An approximate estimate gives that the electron-positron pair production becomes considerable if the critical electric field strength is on the order of  $10^{16}$  V/cm, which can occur only in the atomic systems. For example, in case of uranium, the electric field strength close to the nuclear surface is about  $2.48 \times 10^{19}$  V/cm, which is 1800 times more than the critical field strength and a factor of 2 less than the field strength in superheavy systems with  $Z \geq 170$ , where spontaneous pair production is predicted to take place if the total charge is confined in a sufficiently small volume for sufficiently long time [30]. Therefore, the size of radiative corrections strongly increases for high  $Z$  ions. The electric field strength for different  $Z$  and atomic levels are shown in Fig. 2.5. The graph shows the increment of the electric field strength with  $Z$ . Also with decreasing distance between electron and nucleus, the QED contributions become large. The radial probability density of an electron in an atom is proportional to  $r^{2l}$  [9], where  $l$  is the orbital quantum number. Hence for s-states (i.e.,  $l = 0$ ) the probability that the electron will be near to nucleus is large. Therefore, radiative corrections for s-state electron are the most significant ones.

### Nuclear Mass and Size Correction

In the interaction between an electron and a nucleus, one needs to consider it as a two-body system, which can be treated in the Dirac theory in the following way: The mass of the nucleus enters the Dirac equation and leads to a quasipotential equation in the center-of-mass system [28]

$$(E - \sqrt{p^2 + M^2} - \alpha p - \beta m)\psi_{nlj}(p) = \int V(E, p, q)\psi_{nlj}(q)d^3q \quad (2.5)$$

where  $V$  is a quasipotential. Here,  $p$  and  $q$  are the momentum and spatial coordinate of one of the particles in the center-of-mass frame, and  $M$  and  $m$  denote the masses of the nucleus and the electron, respectively. Solving the above equation yields the total energy shift of the state due to the nuclear mass correction.

An important nuclear size and shape correction results from the deviation of the potential of an extended nucleus from the point like one. In order to determine this correction the radial Dirac equation for a given electron state (e.g.,  $1s_{1/2}$ ) with the potential of an extended nucleus has to be solved and thereby the difference of this energy eigen value from the energy for a point like nucleus is obtained. The uncertainty in the finite size correction comes from the uncertainty in the nuclear radii. For heavy elements this uncertainty dominates the total error of the Lamb shift [36].

### QED Corrections of Second Order in $\alpha$

As it was mentioned before, QED is formulated as a perturbation theory with  $Z\alpha$  and  $\alpha$  being the expansion parameters. The  $n$ th order in perturbation expansion of  $\alpha$  is represented by  $2n$  vertices. For example the Fig. 2.3 shows two vertices of first order in  $\alpha$ . With the advent of high precision Lamb shift experiments it is necessary to evaluate corrections due to  $\alpha^2$ . The radiative corrections of the order of  $\alpha^2$  contribute to the Lamb shift of the  $1s_{1/2}$  state to about 1 eV for uranium [6]. The QED corrections of second order in  $\alpha$  are defined by 10 Feynman diagrams shown in Fig. 2.6 and each of them indicates two photon lines. The first row in Fig. 2.6 shows pictures with the two loop self-energy. These diagrams are the ones most difficult to evaluate in all orders in  $Z\alpha$  [24]. For the  $1s_{1/2}$  state of uranium this diagrams contribute -0.971 eV [31]. The second set of diagram represents the two loop vacuum polarization (VPVP). For an extended nucleus charge distributions these diagrams yield -0.72 eV for  $1s_{1/2}$  state of uranium [32]. The third set of diagrams (SEVP) are mixed self energy-vacuum polarization. The calculations for the  $1s_{1/2}$  state of uranium by taking into account both Uehling and Wichmann-Kroll terms yields 1.14 eV [33]. The remaining S(VP)E has been evaluated in the Uehling approximation in Ref. [34] and yielded 0.13 eV for the  $1s_{1/2}$  state of uranium. For all the diagrams of  $\alpha^2$  the calculations are done non-perturbatively in  $Z\alpha$  series.

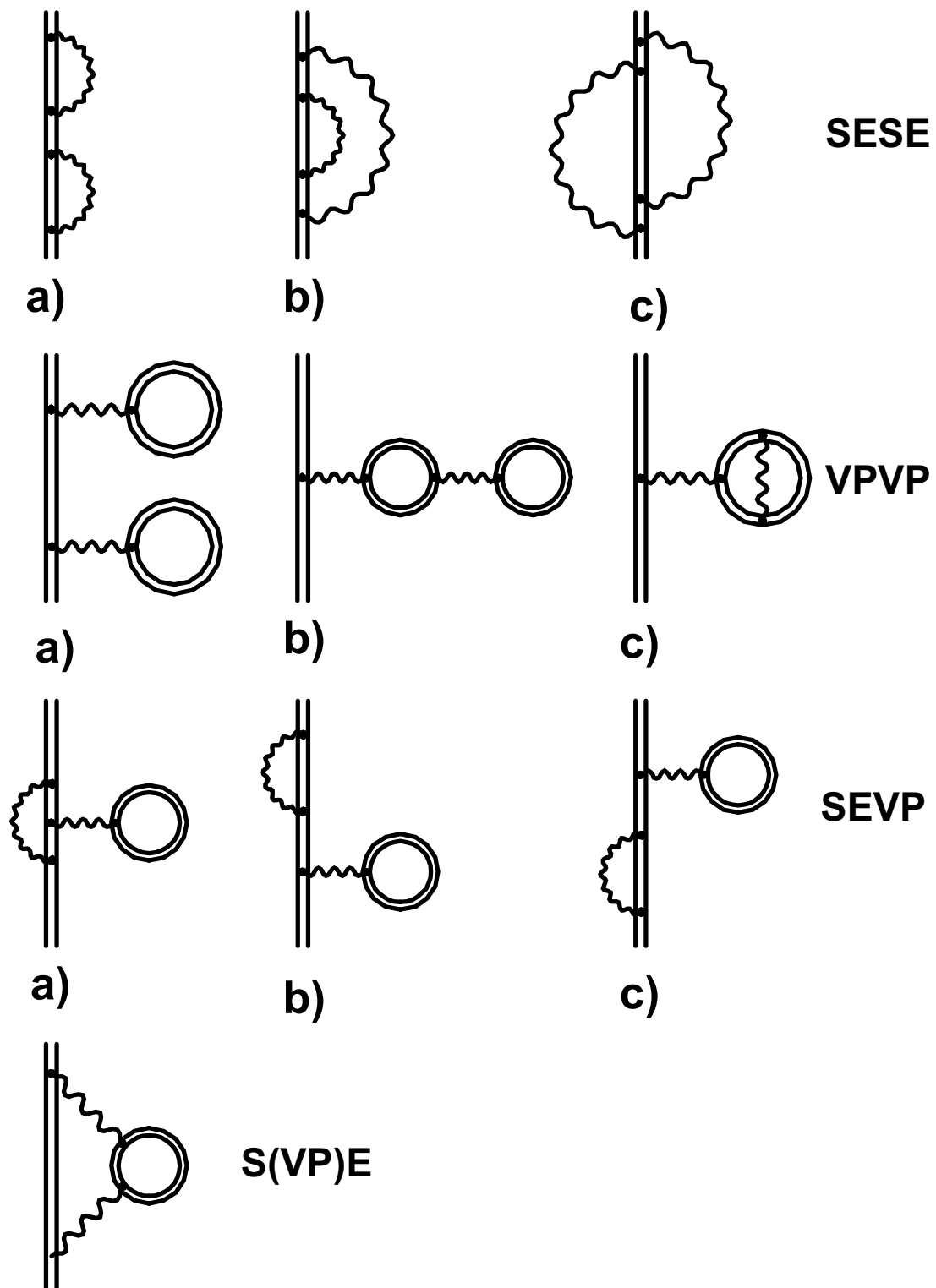


Figure 2.6: One-electron QED corrections of second order in  $\alpha$  [29].

### Other Corrections to the Lamb Shift

The recoil corrections take the nuclear motion into account and this reflects a deviation from the theory for an infinitely heavy nucleus. They depend on the mass ratio  $m/M$  and on  $Z\alpha$ . The total contribution due this effect reads as [35]

$$\Delta E_r = -\left[\frac{m}{m+M}E_{nj} + \frac{m_r c^2 (Z\alpha^4)}{8(m+M)n^4}\right] \quad (2.6)$$

This corrections for extended nuclei have been calculated in [39].

Finally, the nuclear polarization effect has to be taken into account, which arises from interactions of the electron with the nucleus where intermediate states of the nucleus are excited. The energy shift due to this effect has been evaluated by Plunien and Soff [40] and by Nefiodov et al. [41].

In one-electron systems the Lamb shift for  $s$ -states is commonly presented by the following equation [42, 43]:

$$L = \frac{\alpha (Z\alpha)^4}{\pi n^3} \cdot F(Z\alpha) \cdot mc^2 \quad (2.7)$$

where  $F(Z\alpha)$  is a slowly varying function of  $Z$ . This function considers all the radiative contributions and includes in addition the effect caused by the finite size of the nucleus. Since the Lamb shift scales approximately with  $Z^4/n^3$ , all these corrections are largest for the ground-state and for the strong fields at high- $Z$ . For light systems the self-energy gives the most important Lamb shift correction. With increasing nuclear charge, however, the influence of nuclear size effects and of the vacuum polarization increases continuously. In Fig 2.7 the different contributions to the Lamb shift in hydrogen-like ions are given separately as a function of the nuclear charge and energy. For light one-electron systems as atomic hydrogen, the theory of QED is now well confirmed with extraordinary precision [1]. Here, the experiments are sensitive to the lower orders of the function  $F(Z\alpha)$  which for low- $Z$  systems, can be calculated by an  $\alpha Z$  expansion. However, for a test of higher order terms, which are not accessible using low- $Z$  ions, the heaviest species such as hydrogen-like uranium are required.

## 2.2 The Status of 1s Lamb Shift

The most accurate Lamb shift measurement has been performed on atomic hydrogen, where the 1S-2S transition was measured with an accuracy of 1.8 parts in  $10^{14}$  [44]. For  $Z = 18$  and 28, relative uncertainties of 1.5 % and 2 % have been obtained [45]. For high- $Z$  hydrogen-like ions, the most direct experimental approach is a precise determination of the x-ray energies emitted by transitions from bound (and/or continuum) states into the ground state of the ion. In particular, the Lyman transitions are used in this kind of experiments as they appear

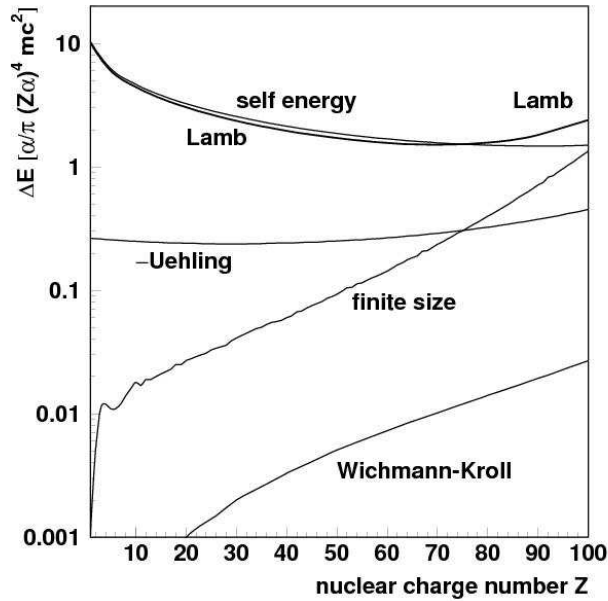


Figure 2.7: The different contributions to the ground state Lamb shift of H-like ions as a function of nuclear charge [43]. The energy shift presented in the indicated units gives the dimensionless function  $F(Z\alpha)$ .

most intense and well resolved in the x-ray spectra. The goal of the experiments is to achieve a precision which probes QED contributions which are beyond the one-photon exchange corrections.

The  $^{208}\text{Pb}$  nucleus is the ideal choice for the test of QED, because the charge-radius of this nucleus is very well known compared to the other high- $Z$  ions. For example the theoretical nuclear size uncertainty of  $^{208}\text{Pb}$  is 0.02 eV compared to 0.10 eV for  $^{238}\text{U}$  and 0.16 eV for  $^{197}\text{Au}$  [36]. Therefore,  $^{208}\text{Pb}$  is preferable to test QED to the uncertainty of 1 eV or below.

In Fig. 2.8 the experimental results for the ground state Lamb shift in hydrogen-like ions are given and compared with the theoretical predictions [43] (solid line). The solid symbols depict the results from the SIS/ESR facility [49, 50, 51, 52, 53]. Over the whole range of nuclear charges an excellent overall agreement between experiment and theory is observed. For the regime of the high- $Z$  ions ( $Z > 54$ ) most of the results provide a test of the ground-state Lamb shift contribution at the level of 30%. Only the results from the gas-jet target for uranium [49] and from the electron cooler (for gold [50] and uranium [51]) have a considerably higher accuracy. Up to now most of the Lamb shift experiments for high- $Z$  ions were performed for hydrogen-like uranium. The Table 2.1 shows separately the theory of the ground state Lamb shift in  $^{238}\text{U}^{91+}$  together with the most recent experimental result [6]. All the values are given in eV. This result shows that the present status of theory and experiment provides a test of the QED effects at the

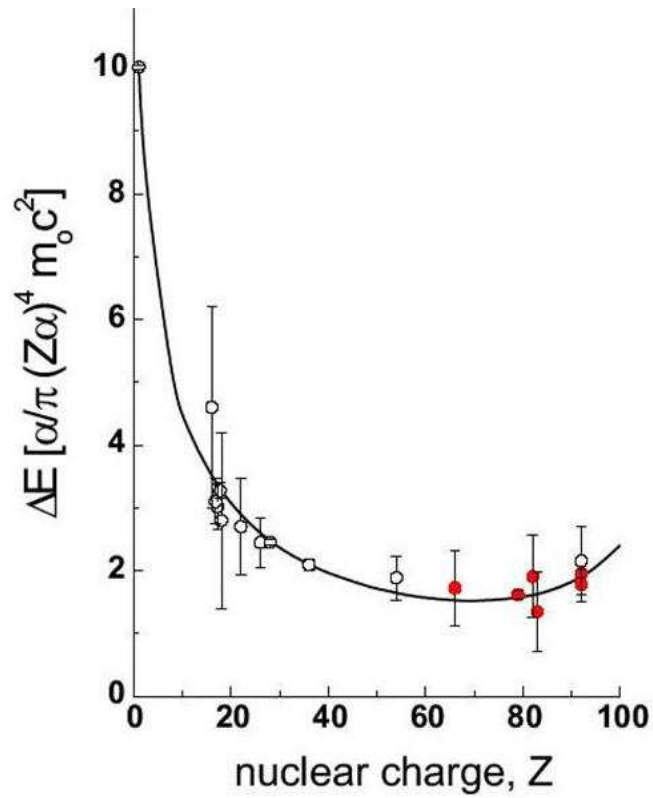


Figure 2.8: The experimental results [49, 50, 51, 52, 53] for the  $1s$  Lamb shift in high- $Z$  ions in comparison with theoretical predictions [43]. The energy shift is presented in the indicated units gives the dimensionless function  $F(Z\alpha)$ . The solid circles represent the results from the SIS/ESR facility.

first-order in  $\alpha$  on the level of 2% [6].

Finite nuclear size	198.81
Nuclear Recoil	0.46
Nuclear Polarization	-0.19
VP (see Fig 2.3)	-88.60
SE (see Fig 2.3)	355.05
SESE (see Fig 2.6)	-1.87
VPVP (see Fig 2.6)	-0.97
SEVP (see Fig 2.6)	1.14
S(VP)E (see Fig 2.6)	0.13
<b>Total Lamb shift</b>	$464.26 \pm 0.5$
<b>Experiment</b>	$460.2 \pm 4.6$

Table 2.1: Comparison of the total ground state Lamb shift value of  $^{238}\text{U}^{91+}$  obtained in the cooler experiment [6, 54] with the theoretical prediction [55] obtained from the various individual contributions.



## Chapter 3

# The Accelerator Facility and Experimental Environment at GSI

GSI is operating an accelerator facility which consists of the UNiversal Linear ACcelerator (UNILAC), the heavy ion synchrotron (SIS) and the Experimental Storage Ring (ESR) with ions ranging from  $H^+$  up to  $^{238}U^{92+}$ . The present accelerator facility is shown in Fig. 3.1. In the 110 m long UNILAC, low charge state ions from different kinds of ion sources are accelerated, stripped to higher charge states and again accelerated up to a maximum energy of 11.4 MeV/u. Behind the UNILAC the beam can be distributed within the low energy experimental areas or can be transferred into the SIS. The charge state is further increased in a stripping target placed before the injection point of the SIS. The light ions up to  $Z \simeq 28$  can be stripped fully in this target. The SIS with 217 m circumference has a magnetic rigidity of  $B\rho = 18$  Tm, which allows a maximum beam energy of about 1 GeV/u for  $U^{73+}$  and 2.1 GeV/u for  $q/A = 0.5$ . After acceleration and extraction (slow or fast) the beam can be transferred to the ESR or to the experimental caves. The transfer is possible directly from the SIS or through the FRagment Separator (FRS). In the transfer line between the SIS and the ESR again stripper foils are placed, which can strip all electrons from the ions depending on the beam energy.

### 3.1 The Experimental Storage Ring

The Experimental Storage Ring (ESR) with a circumference of approximately 108 m enables to store ion species ranging from  $Li^+$  to  $U^{92+}$  from a minute up to longer than a day. The ring contains important components for experiments as the electron cooler and the gas-jet target. The ESR is shown schematically in Fig. 3.2. The maximum bending power of 10 Tm enables to store uranium

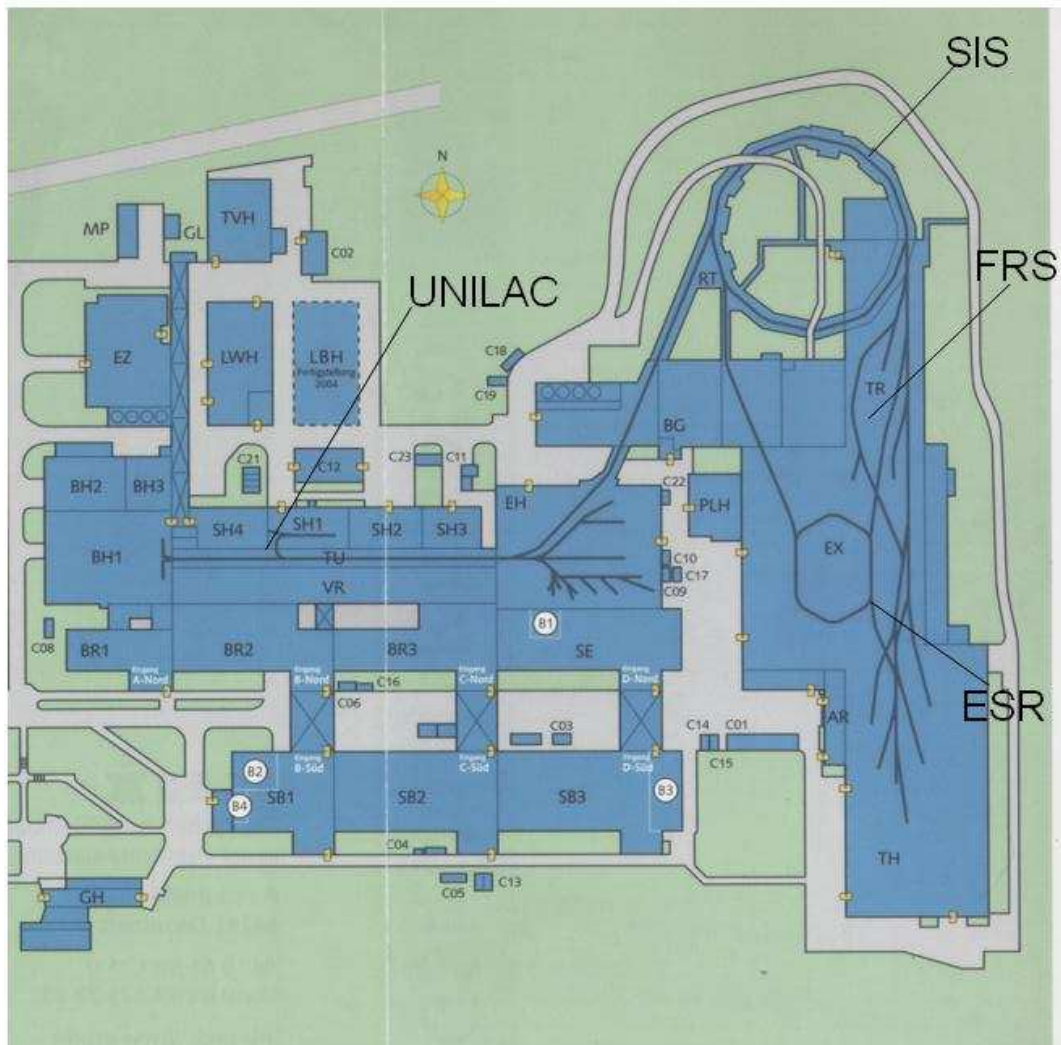


Figure 3.1: The layout of the present accelerator facility at GSI.

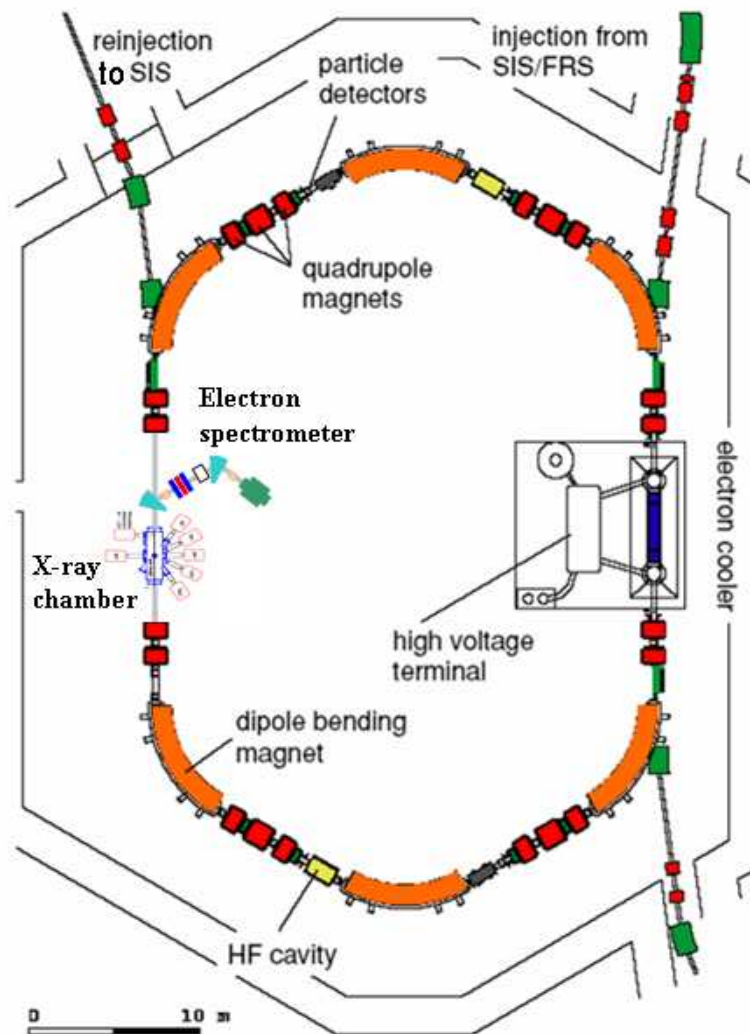


Figure 3.2: The Experimental Storage Ring (ESR). The ring consists of 6 dipoles (maximum bending power of 10 Tm), 4 triplets, 4 duplets and 8 sextupoles, rf acceleration cavities and beam-diagnosis components. The two experimental areas are the electron cooler and the gas-target. There are windows through which the target area can be accessed. An electron spectrometer is also installed close to the target area.

ions with energies up to 556 MeV/u. Actually the beam energy is limited to 370 MeV/u due to the maximum stable cooler voltage of about 210 keV. An ultra high vacuum pressure of about  $5 \times 10^{-11}$  mbar is maintained inside the ring, which helps to increase the lifetime of the beam by reducing the interaction with the residual gases.

### 3.1.1 The Electron Cooler

The ESR offers the unique possibility to store and cool fully stripped heavy ions up to uranium. The cooling is based on the Coulomb interaction of the circulating ions and the cold electrons in the cooler. The electrons are continuously produced in an electron gun with a heated cathode and are accelerated to a velocity equal to the ion beam velocity. The electron beam is guided and combined with the ion beam by a solenoid in a 2.5 m long straight section in the cooler. At the end of the section, the electrons are separated again from the ion-beam and sent to collector.

A hot ion beam implies that the ions have random motion in all directions in the co-moving frame. This heat is transferred to the cold (monoenergetic) electrons through the Coulomb interaction and the random motions of the ions are reduced. For cooling purposes the electron current is generally 100 to 300 mA. The cooling leads to an emittance of the stored beam of less than  $0.1 \pi$  mm mrad and to a small beam size with a typical diameter of less than 5 mm. In particular, electron cooling guarantees a well defined constant beam velocity of the order of  $\Delta\beta/\beta \simeq 10^{-5}$ . It reduces the relative longitudinal momentum spread of the injected ion beam of  $\Delta p/p \simeq 10^{-3}$  to about  $10^{-5}$  [54], which can be read from the signal of a pickup via the Schottky noise spectrum of the circulating ions. The electron cooler is shown schematically in Fig. 3.3. The momentum spread of a hot and a cooled ion beam is shown in Fig. 3.4.

The ESR is capable to store about  $10^8$  ions of different species with different charge states. In case of bare uranium theoretically the number of ions, which can be stored is  $9.3 \times 10^9$  at 556 MeV/u and  $4.4 \times 10^8$  at 50 MeV/u and the limitations to these numbers come from the space-charge of the ions [17].

### 3.1.2 The Internal Gas-jet Target

Besides the electron cooler, the internal gas jet target is an important component for experiment in the ESR. The target is able to deliver various gases like He,  $H_2$ ,  $N_2$ ,  $CH_4$ , Kr, Xe, etc, with particle density of about  $10^{12} - 10^{14}/cm^3$ . The gas-jet is operated with a differential pumping system in both the injection and dump part in order to make the the system compatible with the ultra-high vacuum of the ESR. The gas is injected into the target area through a "Laval nozzle" with a diameter of 0.1 mm, which can be cooled with liquid  $N_2$  in order to increase the density especially of a  $H_2$  target gas. A schematic diagram of the gas-jet target

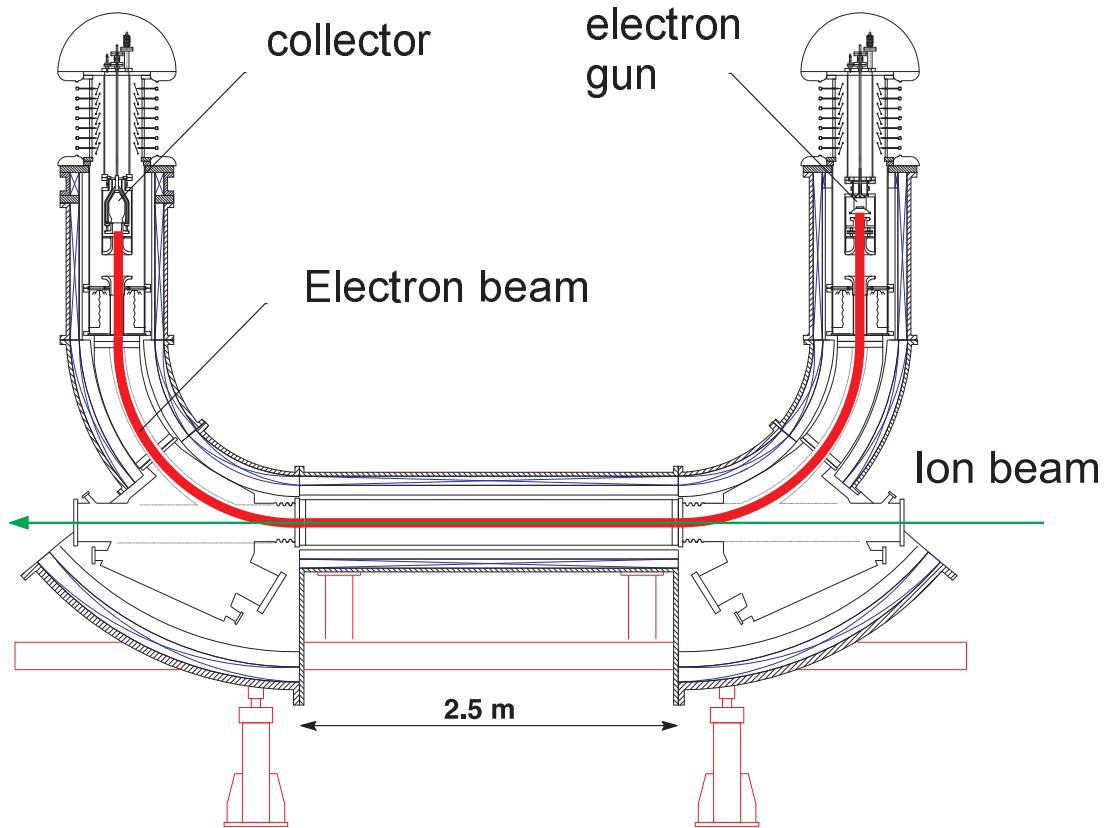


Figure 3.3: The electron cooler consists of main components as the electron gun, the collector, the toroids and the solenoid.

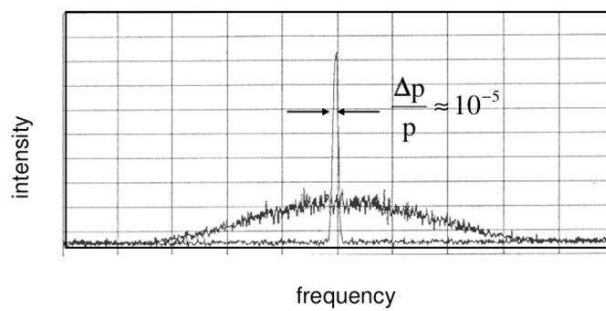


Figure 3.4: The Schottky frequency spectrum for a circulating beam of  $U^{92+}$  ions at 295 MeV/u. The broad distribution refers to the hot injected beam and the narrow distribution is momentum profile of the cooled beam [56].

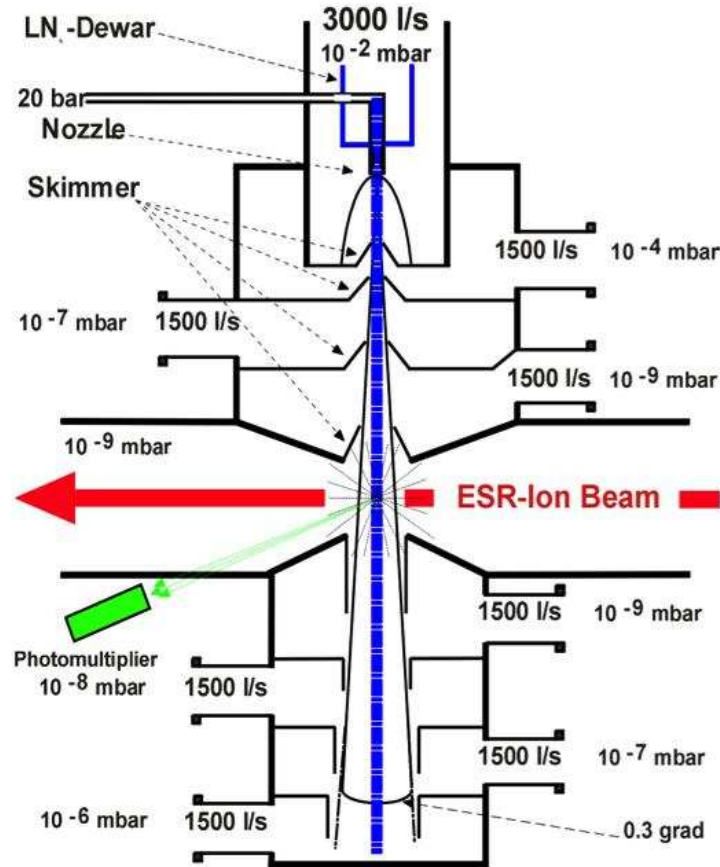


Figure 3.5: The ESR internal gas-jet target.

is shown in Fig. 3.5. The first stage of the injection part with nozzle and first skimmer is pumped by a system of roots pumps, with pumping speeds of  $12000 \text{ m}^3/\text{h}$ ,  $2000 \text{ m}^3/\text{h}$ ,  $500 \text{ m}^3/\text{h}$ ,  $200 \text{ m}^3/\text{h}$  and  $40 \text{ m}^3/\text{h}$  for oil-free compression to atmosphere pressure [57]. The maximum gas load to this stage is  $300 \text{ mbar l/s}$  for all gas species in use. The remaining three stages of the injection part and the four stages of the gas-jet dump are pumped by a differential pumping system of turbo pumps. To perform standard services without breaking the ESR vacuum, the injection part and gas-jet dump can be separated from the interaction chamber by the use of two UHV compatible valves. The distance between the nozzle and the interaction point is optimized to  $500 \text{ mm}$  in order to provide the space for the installation of large pumping speed at the injection part. The gas-jet has diameter of typically  $5 \text{ mm}$ . To optimize the overlap between the ion beam and the target the counting rate of photons detected from the interaction point, by a photomultiplier is maximized by shifting the position of the ion beam in the ESR.

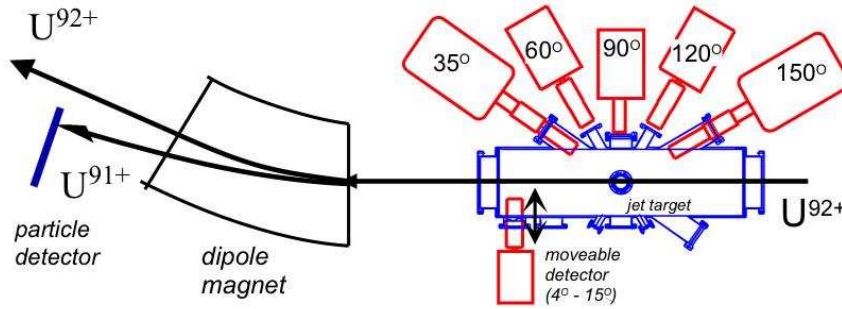


Figure 3.6: Layout of the experimental arrangement at the internal jet-target. X-ray detectors view the target interaction zone at observation angles of  $4^\circ - 15^\circ$ ,  $35^\circ$ ,  $60^\circ$ ,  $90^\circ$ ,  $120^\circ$ , and  $150^\circ$ . All detectors are separated from the UHV system of the storage ring either by  $50 \mu\text{m}$  thick stainless steel ( $4^\circ$ ,  $60^\circ$ , and  $120^\circ$ ) or by  $100 \mu\text{m}$  thick Be windows. Photon emission is usually observed in coincidence with the down-charged ions, detected in the particle counter located behind the dipole magnet.

### 3.1.3 X-ray Spectroscopy at the Internal Gas-jet Target of the ESR

The internal gas-jet target provides the unique opportunity to perform x-ray spectroscopy at different observation angles shown in Fig. 3.6. The accessible angles are  $4^\circ - 15^\circ$ ,  $35^\circ$ ,  $90^\circ$ ,  $120^\circ$  and  $150^\circ$ . The x-ray detectors are separated from the vacuum system of the ESR by  $50 \mu\text{m}$  thick stainless steel or  $100 \mu\text{m}$  thick Be windows.

### 3.1.4 Charge Exchange Processes in Gas Target

The collisions between highly charged ions and atoms or molecules of the gas targets in the ESR opened up many possibilities to study charge exchange processes, which result in the production of x-rays. The two main processes which dominate the charge exchange processes are Radiative Electron Capture (REC) and Non-Radiative Capture (NRC). There are also other mechanisms such as Radiative Transfer Excitation (RTE) and Non-resonant Transfer Excitation (NTE), which lead to projectile excitation simultaneous with capture of an electron by the projectile during the collision.

#### Radiative Electron Capture

The radiative electron capture is the analogue of the Radiative Recombination (RR) in ion-electron collisions. While in RR a free electron is captured into a

projectile bound state, the REC occurs by capturing an electron from a bound state of the target atom into some state in the projectile ion. The charge exchange process leads to the emission of a photon in concurrence with the energy and momentum conservation of the interacting particles. If  $E_{bt}$  is the initial binding energy of the target electron,  $E_b$  the final binding energy of that electron in projectile, and  $E_{kin}$  the relative kinetic energy between projectile and target then the energy of the photon emitted in this process can be written as  $\hbar\omega = E_{kin} + E_b - E_{bt}$  [58]. If the binding energy of the target electron is much less than the relative kinetic energy between ion and target, these electrons are considered to be quasi-free electrons. In practice the target electron has a momentum distribution (the Compton profile), which leads to a characteristic width in the energy distribution of the REC spectrum [59]. The REC can give direct access to the investigation of the photoionization process near the threshold, which is the time-reversed process of the REC. The cross section for the REC can be scaled from the non-relativistic dipole approximation of Stobbe as [57, 58]

$$\sigma_{REC} \simeq \frac{Z_T \cdot Z_p^5}{v^{5/2} \cdot n_f^3} \quad (3.1)$$

where  $Z_T$  and  $Z_P$  are atomic numbers of target and projectile respectively,  $v$  is the relative velocity and  $n_f$  the principle quantum number of the final state of the electron. If an electron is captured directly from the target atom into the K-shell of the projectile by REC process, then it's called a K-REC process and similar processes are L-REC, M-REC etc. At high projectile velocities the REC is the dominant process as shown in Fig. 3.7, and with decreasing projectile velocity, the intensity of the K-REC photons decreases and the NRC processes increases. Therefore, the electron cascades down from an upper level to the K-shell, which gives rise to increased Lyman intensities, as shown in Fig. 3.8.

### Non-radiative Capture

This is a Coulomb capture process, where energy and momentum are distributed among the interacting particles namely the target atom, the ion and the captured electron. If  $E_f$  and  $E_i$  represent the final and initial energy of the bound electron, then resulting kinetic energy gained among the collision partners is  $E_{kin} = E_f - E_i$ . The cross section for NRC scales as [57, 58]

$$\sigma_{NRC} \simeq \frac{Z_T^5 \cdot Z_p^5}{v^{12} \cdot n_f^3} \quad (3.2)$$

Fig. 3.9 shows the dependence of the REC and NRC cross sections on the target atomic number  $Z_T$  for 220 MeV/u He-like uranium ions. It is apparent that for target atoms heavier than argon NRC is the most dominant process at this collision energy.

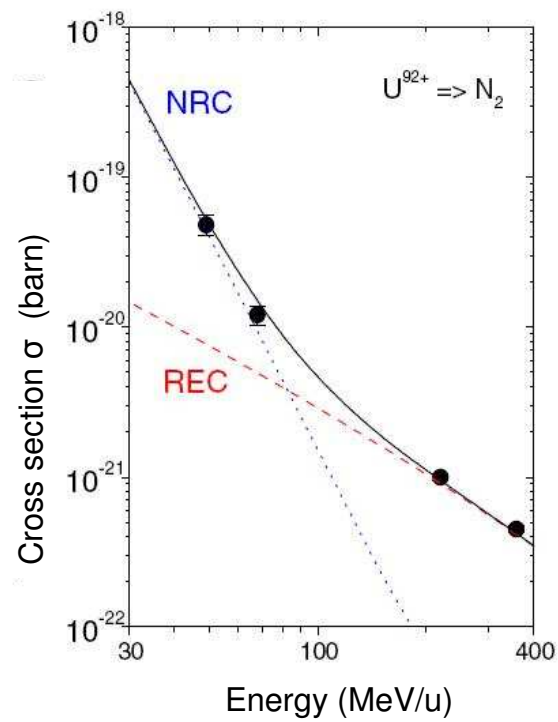


Figure 3.7: The cross sections for REC and NRC as a function of the projectile energy in the interaction between  $U^{92+}$  and  $N_2$ . The solid line represents the total estimated cross section of REC and NRC processes and the experimental data points are in good agreement with theory [60].

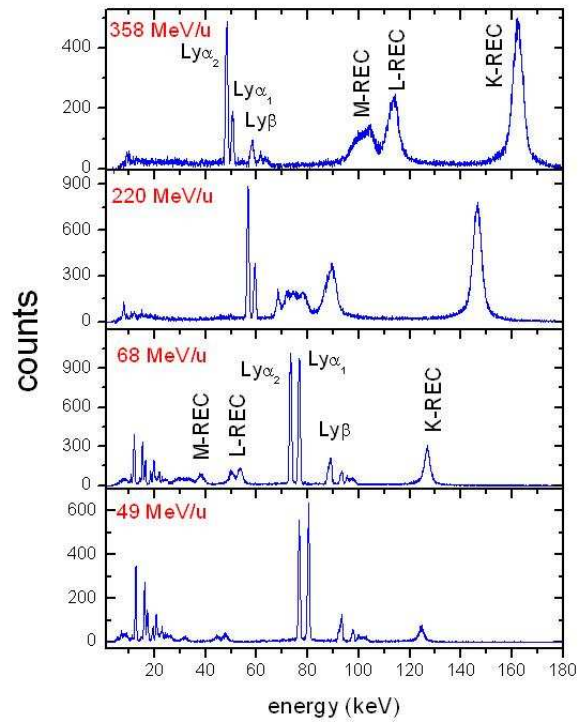


Figure 3.8: X-ray spectra observed in collisions between bare uranium ions and  $N_2$  molecules at the gas-jet target in the ESR at an observation angle of  $132^\circ$  [61]. The intensity of the REC lines decreases with decreasing beam energy and the Lyman-line intensities increase.

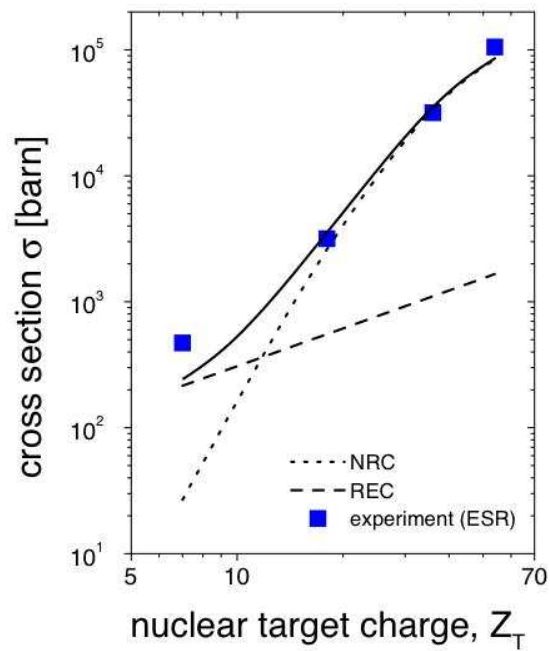


Figure 3.9: The electron capture cross sections of bare uranium at energy of 220 MeV/u interacting with different gas targets of nuclear charge  $Z_T$ . The dashed lines are theoretical prediction for both the REC and NRC processes. The solid line is the prediction for the sum of both processes. The experimental points [62] (square) are in good agreement with the theory [63, 64].

### Other Processes

Besides the REC and NRC processes there are other processes like Resonant Transfer Excitation (RTE) and Non-resonant Transfer and Excitation (NTE). In the RTE an electron is transferred from the target into the projectile and simultaneously an electron in the projectile is resonantly excited into a higher level. Thus RTE is the time reversed Auger effect. A schematic representation of the different processes is shown in Fig. 3.10. For example in the KLL-RTE (lowest case) an electron from a target bound state is transferred to the L-shell of the projectile and the transfer energy excites one K-shell electron of the projectile into the L-shell. The resonance energy can be written as  $E_e = -E_K + 2(E_K - E_L) \simeq 0.5RZ_p^2$ , which is therefore the kinetic energy of the electron in the target,  $E_K$  and  $E_L$  are the K and L-shell binding energies of projectile.  $R$  is the Rydberg constant and  $Z_p$  is the atomic number of the projectile. The cross section for RTE scales as  $\sigma_{RTE} \sim Z_p^{-1}$  [65]. NTE is the non-resonant electron capture by simultaneous projectile excitation. Within NTE, two uncorrelated processes occur: projectile excitation simultaneous with a kinematic electron capture during the collision, leading to a doubly excited state of the projectile by simultaneous charge exchange.

## 3.2 Aspects of 1s Lamb Shift Measurement at the Gas Target

As it was discussed in the previous chapter, the 1s Lamb shift is the deviation of the binding energy of the 1s level from the prediction of the Dirac theory for a point like nucleus. In order to probe the real binding energy of a 1s level, one can measure the transition energy from some upper state to the 1s level of that ion and if one subtracts this transition energy from the energy difference obtained from the Dirac theory the Lamb shift of 1s state is obtained (provided the influence of QED-effects on the upper level is extremely small). A suitable transition has been chosen for the 1s Lamb shift measurement out of many possibilities resulting from the interaction between the gas-target atoms and the ions. The K-REC photons are not suitable for this purpose, because the transition energy depends on the relative velocity of the ion and the target atom and the initial energy of that electron in the target atom, which are not possible to determine. Another possibility is the Ly  $\alpha_2$  transition i.e., the transition from  $2p_{1/2}$  to  $1s_{1/2}$  (for lead ions used in the FOCAL experiment, the transition probability is  $2.95 \times 10^{16} \text{ s}^{-1}$  [16]). However, there is a M1 transition (see Fig. 2.2) from  $2s_{1/2}$  to  $1s_{1/2}$  (for lead ion the transition probability  $5.34 \times 10^{13} \text{ s}^{-1}$  [16]), which has a transition energy of 39.2 eV larger than the Ly  $\alpha_2$  energy. This is due to the fact that in  $Pb^{81+}$  the  $2s_{1/2}$  level has a Lamb shift of 43.10 eV and the  $2p_{1/2}$  level of 3.90 eV [36]. The blending of these two transitions with a energy difference of 39.2 eV

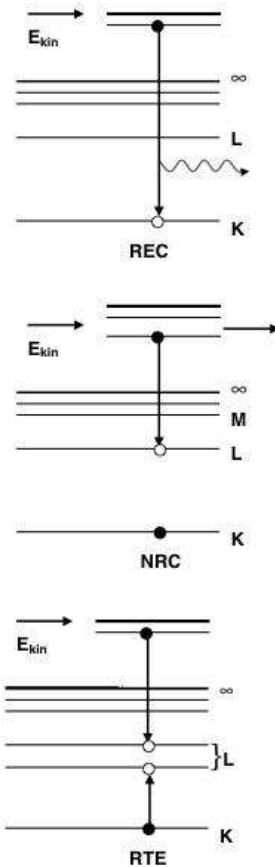


Figure 3.10: A schematic representation of the different dominant processes during the interaction between bare and hydrogen like ions and atoms in the gas target in the ESR. In the first case (REC) an electron is transferred from a bound state of a target atom into the K-shell of the projectile, resulting in the emission of a K-REC photon. In the second case (NRC) the energy transfer is shared by the colliding partners. In the last case (RTE) an electron in the projectile is resonantly excited due to the transfer of the electron from the target [58].

can't be resolved by our spectrometer, which has resolution of about 100 eV at energies around 60 keV [66, 68]. The best possibility left is to measure the Ly  $\alpha_1$  transition, i.e., the transition between  $2p_{3/2}$  and  $1s_{1/2}$  (the transition probability is  $2.57 \times 10^{16} \text{ s}^{-1}$  [16]). This transition is the combination of an electric dipole transition (99%) and a tiny amount of a magnetic quadrupole transition (1%) [15] (see Fig. 2.2).

# Chapter 4

## The FOCAL Spectrometer

An accurate determination of quantum-electrodynamical (QED) contributions to the K-shell binding energy of H-like ions can be obtained from high precision measurements of the energies of transitions into the K-shell. For very heavy ions the accuracy aimed at is almost about  $\pm 1$  eV at transition energies of 50-100 keV [67]. The development of a system of two crystal spectrometers at GSI has provided us an edge to this experimental challenge. Each of the spectrometers is working in the FOcusing Compensated Asymmetric Laue (FOCAL) mode along with high performance position sensitive micro-strip Ge detectors. For the experiment two such set-ups have been aligned along the same optical axis facing each other at the gas-jet-target in the ESR. The alignment of the spectrometers will be discussed in the next chapter. The components and principle of the crystal spectrometer will be discussed in the next sections of the present chapter.

### 4.1 The FOCAL Geometry

The FOCAL geometry essentially involves a modified Cauchois geometry, which is an optimization of the spectrometer in order to cope up with measurements done with fast ion beams and limited source strength [68, 69]. In a standard Cauchois geometry an extended x-ray source is placed on the convex side of a cylindrically bent crystal. The configuration follows the Laue case, where the reflected beam leaves the layer through the surface, which is opposite to the entrance surface. The x-ray diffraction occurs by the crystal lattice satisfying the Laue-Bragg condition

$$2 \cdot d \cdot \sin\theta = \lambda \quad (4.1)$$

where  $\lambda$  is x-ray wavelength,  $\theta$  the Bragg angle and  $d$  the lattice spacing of the crystal. A schematic diagram of the bent crystal geometry is shown in Fig.4.1.

It is apparent from Fig. 4.1 that higher wavelength x-rays will be diffracted into larger angles according to Eq. 4.1. Therefore, they will show up in the

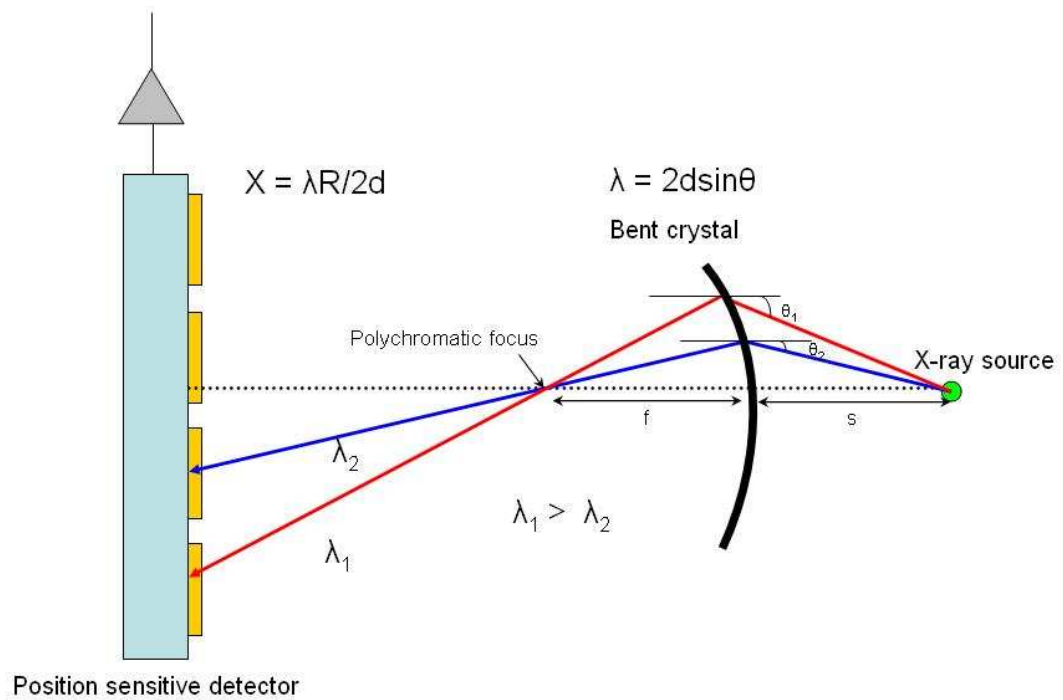


Figure 4.1: The basic principle of a bent crystal geometry. The source is placed on an axis intersecting the crystal at its apex.  $s$  is the distance between crystal apex and the source and  $f$  the distance of the polychromatic focus from the crystal apex.

detector plane farther down compared to the small wavelength x-rays. Furthermore, it is also noticeable that for a fixed source-to-crystal separation the higher wavelength x-ray is reflected into larger Bragg angles and this requires that bigger wavelength  $\lambda_1$  will be reflected somewhere up from the crystal compared to a small wavelength x-ray  $\lambda_2$ . The spot, where the x-rays of a particular wavelength hit the crystal, is called footprint on the crystal and is measured from the optical axis, which is passing through the apex of the crystal. Clearly, the larger the wavelength, the larger is the distance of the footprint. In fact the locations of these spots i.e., the footprints on the crystal depend on the bending radius  $R$ , source-to-crystal separation  $s$  and the lattice spacing  $d$  as well and can be formulated as [68, 69]

$$t_x = \frac{Rs}{R+s} \cdot \frac{\lambda}{2d} \quad (4.2)$$

All the diffracted wavelengths pass through a common focal point on the optical axis. This focal point is called "polychromatic focus", and its distance from the crystal depends on  $R$  and  $s$  and can be parameterized as [68, 69]

$$f = \frac{Rs}{R+s} \quad (4.3)$$

An x-ray after diffraction from the crystal hits the detector plane at some distance from the optical axis and this distance is approximately proportional to the wavelength of that x-ray. This is called the dispersion of the x-rays. If a detector is placed at the radius of curvature  $R$  of the crystal (shown in Fig. 4.1), then for small Bragg angles (about  $2^\circ - 3^\circ$ ) the approximate vertical distance of the spot of an x-ray of wavelength  $\lambda$  on the detector plane from the optical axis is given by [68, 69]

$$X \simeq R \frac{\lambda}{2d} \quad (4.4)$$

This is the dispersion relation of the spectrometer [68, 69], which will be exploited in detail for the wavelength determination by knowing the position of the x-rays on the detector plane. The position can be very accurately determined by using a position-sensitive detector mounted at a position, which is equal to the radius of curvature of the crystal. In the FOCAL spectrometers two types of position-sensitive microstrip germanium detectors have been used and they will be discussed later in this chapter.

In this context I would like to introduce the so called *energy-dispersion*, which is similar to the wavelength dispersion. The mathematical details of this parameter will be given in data analysis section. However one can understand energy dispersion qualitatively by taking an example. For the FOCAL spectrometer the energy dispersion is estimated to be 1.63 mm/keV [68, 69]. That means, if two spectral lines are emitted from a source having an energy difference of 1 keV, then they will show up on the detector plane with a distance of 1.63 mm. Therefore,

the two lines are well resolved, which is the great advantage of such spectrometers. For the FOCAL spectrometer the anticipated resolution (i.e, the full width at half maximum) is about 100 eV at 63 keV x-ray energy, which is 10 times better than normal semiconductor detector at the same x-ray energy [66, 68]. The improved resolution means reduced FWHM of the spectral lines, that yields an improved statistical uncertainty of the mean centroid of the spectral line, because the statistical uncertainty on the mean is defined by  $(\frac{FWHM}{2.35 \times \sqrt{Counts}})$ .

Unfortunately with such an improved resolution this kind of spectrometers possess very low efficiency. In order to cope up with the limited x-ray source strength in the experiment the geometry of the spectrometer was modified to increase the efficiency by increasing the area of the rocking curves. At this point one may think that increasing the area of the rocking curves could worsen the resolution. But the Lyman lines in our experiment have an intrinsic line width of approximately 17 eV [16]. Therefore, we do not gain anything by making the resolution of our spectrometer below this width. The crystal itself acts like a wavelength filter, i.e., only those x-rays, which satisfy the Bragg's equation of diffraction, are focused on the detector plane. Such a selected photon transmission gives an efficiency of about  $10^{-5}$  [68]. In addition, the solid angle subtended by the crystal to the source gives an efficiency on the order of  $10^{-4}$ , which is obtained from the crystal area of  $40 \times 120 \text{ mm}^2$  and the crystal-to-source separation of 600 mm. The above two efficiencies yield a total efficiency on the order of  $10^{-9}$ , which is 5 orders of magnitude less compared to a germanium detector for same solid angle! The efficiency has been increased by a factor of 20 by introducing an asymmetry angle of  $2^\circ$  in the geometry of the FOCAL spectrometer, which yields an efficiency on the order of  $10^{-8}$  [68, 69] and this is illustrated below.

The diffraction of x-rays from crystal lattice points can occur in following way. Classically when an x-ray wave of frequency  $\nu$  hits the collection of electrons in a lattice point of the crystal, the electrons oscillate with the same incident frequency and as a consequence, the oscillation leads to the re-emission of the x-ray with the same frequency but in a different direction in compliance with conservation of momentum and energy, which can be described by Bragg's equation 4.1. But the electrons in the lattice points don't have a sharp momentum, rather they possess a distribution of momentum, which is called the *Compton profile*. Therefore, the diffracted x-rays have a distribution of wavelengths instead of a single wavelength. This distribution is called the *rocking curve* of the crystal. Now bending a crystal can impart stress to the electrons in the lattice points, which in addition, affects the momentum distribution of the electrons and finally leads to a further broadening (piezoelectric materials are nice examples of a stress effect, where applying stress changes the electron distribution inside the material and as a result they develop electric potential across the solid). We used this property in the FOCAL geometry to broaden the rocking curve.

In order to implement the above mentioned feature in the FOCAL geometry, one has to be careful in choosing the orientation of the crystal planes with respect

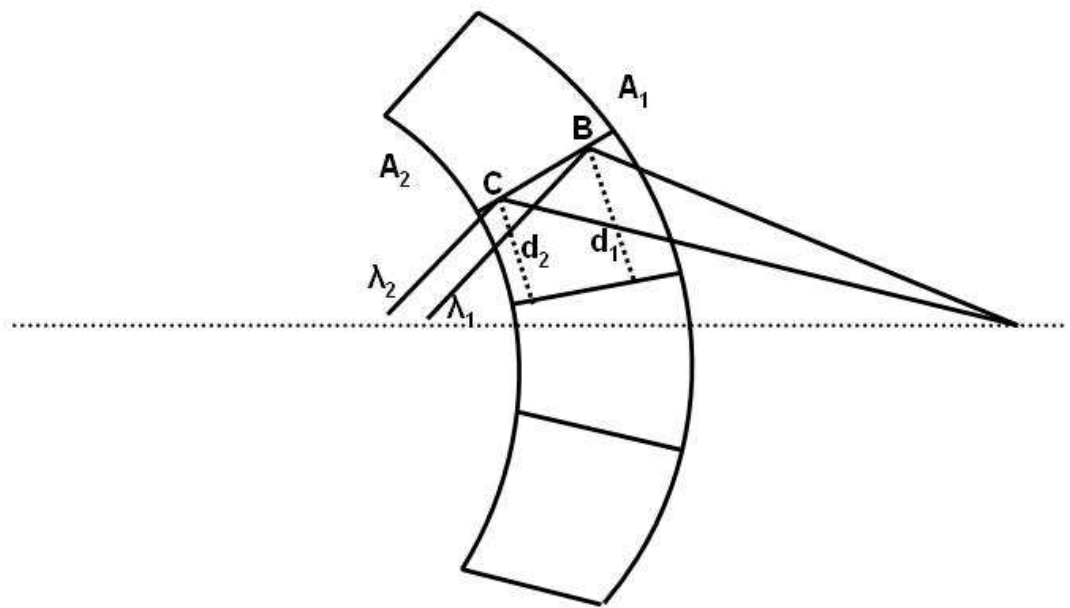


Figure 4.2: In this bent crystal geometry the reflections of x-rays from two different lattice points in the same crystal plane are shown. The lattice planes are perpendicular to the crystal principle surface, which results in a converging structure of the planes due to the bending.

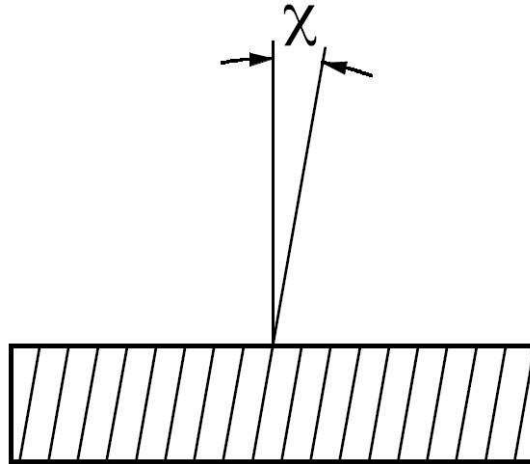


Figure 4.3: The definition of an asymmetry angle [69].

to the crystal surface. This is elaborated in Fig. 4.2. Due to the bending moment applied on the crystal the tangential forces ( $F$ ) are equal on the two opposite surfaces, but the effective areas are now different due to the bending. From this figure it's apparent that the area  $A_1 > A_2$ . So the stress on convex side ( $\frac{F}{A_1}$ ) is less than that of concave side (i.e.,  $\frac{F}{A_2}$ ). Hence the stress in point B is less than in point C, which yields, the broadening of a spectral line in point B is less than that in point C. Let us denote this gradient of broadening as  $\Delta\lambda$  between point B and C. Now let's look at the geometry of the crystal planes, which are taken perpendicular to the crystal surface in this case as shown in Fig. 4.2. Due to the bending, the crystal planes take a converging structure as it is apparent from the figure. The lattice spacing ( $d_1$ ) at point B is larger than that in point C ( $d_2$ ), which yields that the reflected wavelength ( $\lambda_1$ ) from point B is greater than that ( $\lambda_2$ ) from point C for very close Bragg angles. Let us take the gradient of this wavelength variation due to the decreasing lattice spacing from point B to C as  $-\Delta\lambda'$  (negative sign is because, this gradient is just opposite to that of stress effect). It was observed that these two opposite effects almost cancel each other leading to no line broadening [68, 69]. This cancellation can be removed if the planes are tilted such that they remain parallel even after bending the crystal. This provides the desired broadening of the curve. The angle at which the planes are tilted is called an "asymmetry angle ( $\chi$ )" and this is achieved by cutting the crystal in special way (see the Fig. 4.3). Inclusion of this angle  $\chi$  gives a special geometry to our spectrometers and this is called an asymmetry Laue configuration. The effect of introducing an asymmetry angle  $\chi$  is apparent from Fig. 4.4, which shows the increasing area of the rocking curve with asymmetry angle. We used an asymmetry angle of  $\chi = 2^\circ$  in FOCAL geometry. For an

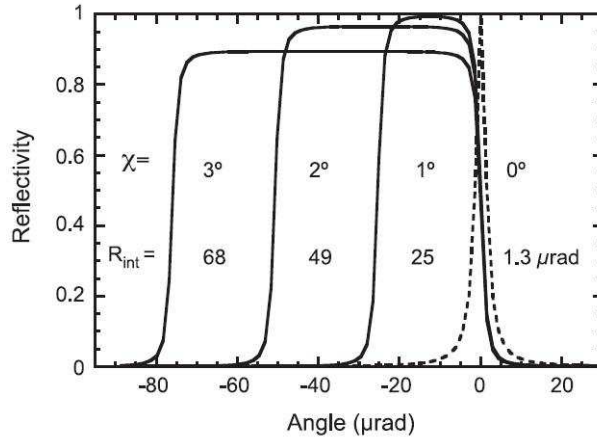


Figure 4.4: Calculated rocking curves for the asymmetry Laue case [69]. The example is for a  $t = 1.5$  mm thick Si (220) crystal with radius of curvature of 2 m, an x-ray energy of 63 keV and an asymmetry angle  $\chi = 0^\circ, 1^\circ, 2^\circ$  and  $3^\circ$  respectively.  $R_{int}$  is the integrated reflectivity in  $\mu\text{rad}$ .

asymmetry Laue case the angular width can be parameterized as

$$\Delta\theta = W\chi\frac{t}{R}(\text{deg}) \quad (4.5)$$

where the constant  $W = 0.034$  rad,  $t$  and  $R$  are the crystal thickness and the radius of curvature respectively [69].

In Fig. 4.5, a symmetric reflection in the Laue case has been considered, this means the crystal reflection planes are perpendicular to the surface. The spectra for both upper and lower reflections from the crystal appear symmetrically with respect to the optical axis. Now, if an asymmetry angle in the crystal is introduced, this symmetry of the spectral lines will be lost. This can be compensated if the source is kept off-axis at the same angle  $\chi$ . This is the reason the spectrometer was baptized as FOCusing Compensated Asymmetry Laue (FOCAL). In our experiment since we cannot tilt the source (i.e., the gas-jet target), the crystal is tilted to the same angle. The schematic view of FOCAL geometry is shown in Fig. 4.6.

## 4.2 The Technical Lay-out of FOCAL

### 4.2.1 The X-ray Sources

The spectrometer has been designed to adapt to both stationary as well as to the fast moving x-ray sources. In order to position a radioactive sample for calibration purposes on the optical axis, a source-positioner was mounted which

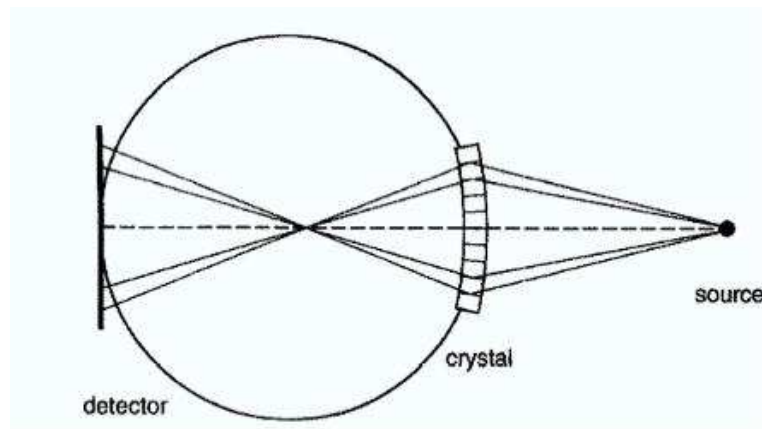


Figure 4.5: A symmetric reflection in the Laue case is shown. Reflections of two different wavelengths are indicated [68].

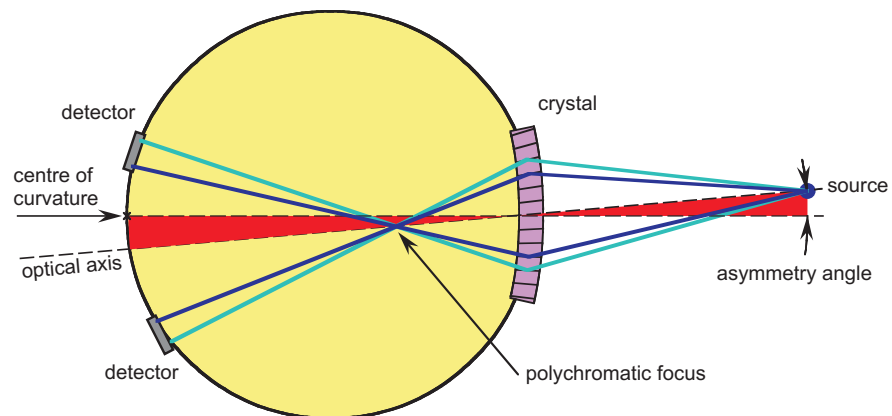


Figure 4.6: The principle of the FOCAL geometry. The source is placed on an axis intersecting the crystal at its apex where it points to the direction of the tilted crystal planes [68].

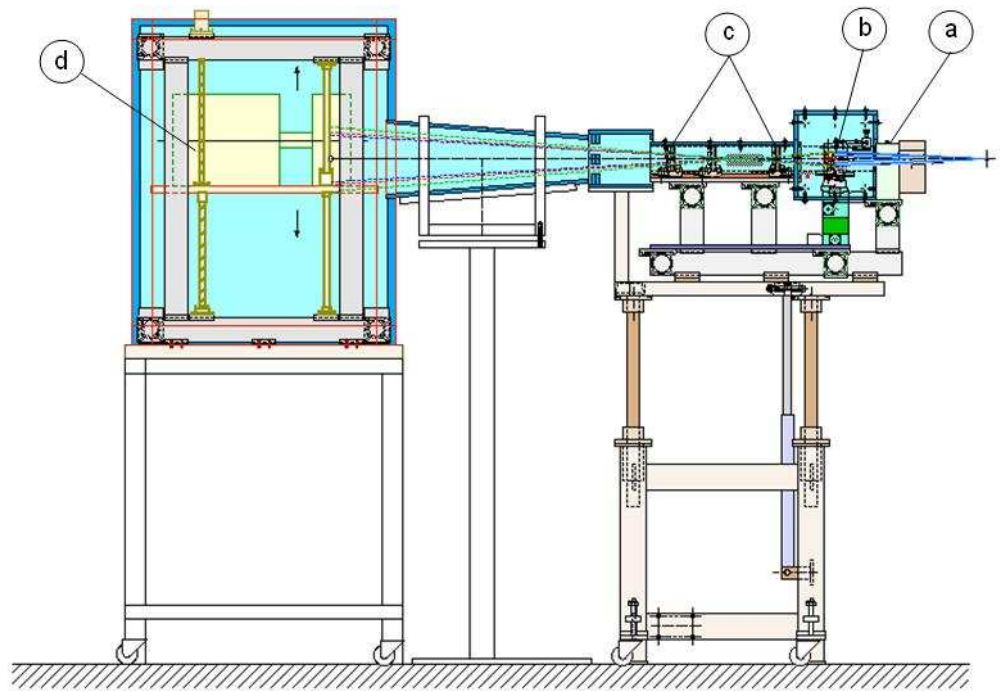


Figure 4.7: Schematic view of one of the two FOCAL spectrometers: (a) is the calibration source holder, (b) the crystal part, (c) the slit assembly and (d) the detector. Each of the two spectrometers is approximately 3.2 m long. The blue color denotes the lead shielding covering the whole spectrometer [71].

can be operated remotely. The radioactive source-to-crystal separation was  $s = 300$  mm. A massive block of tungsten alloy serves as a radiation shielding. When the source was not needed, it was withdrawn to its parking position, where the shielding thickness amounted to 50 mm in all directions. For the calibration of the spectrometer a gamma-ray source  $^{169}\text{Yb}$  with a half-life of 32 days was used. The  $^{169}\text{Yb}$  source emits a rich spectrum of gamma-ray and x-ray lines. The parameters of the FOCAL spectrometer have been optimized with respect to the 63.121 keV line. This gamma-ray line emitted by the source was used for calibration. The calibration spectra will be shown in the analysis section. The  $^{169}\text{Yb}$  was prepared with an isotropically enriched sample of Ytterbium oxide containing the isotope  $^{168}\text{Yb}$  source in the form of a thin tablet of 5 mm diameter sealed in a small capsule of pure aluminium. The sample was neutron activated in the nuclear reactor at the Institut fuer Kernchemie in Mainz. The sample used in our experiment had an initial activity of  $2 \times 10^9$  Bq [70]. Withdrawing the stationary source the optical axis is free to observe X-rays produced by ion interaction with a gas jet of the ESR located at a distance of 600 mm from the crystal.

### 4.2.2 The Background Shielding

Both the spectrometers were covered with 15 mm thick lead sheets with very low gamma ray radioactivity. This arrangement prevented background x-rays hitting directly the detectors. The blue color in Fig. 4.7 shows the lead covering through out the spectrometer. Additional lead sheets were placed just in front of the detectors positioned such that only Bragg-reflected X-rays could reach the detector.

### 4.2.3 The Crystal Component

The crystal part of the FOCAL spectrometer consists of a cylindrically bent and nearly perfect silicon crystal (220) with 2 m radius of curvature, which is glued in a crystal bending device shown in Fig. 4.8. Silicon was chosen for its long term stability and because its diffraction properties can be described well by theory. For the plane (220) used in the crystal, one can obtain maximum intensity in the Laue patterns produced in the diffraction [70].

The optimal thickness of the crystal was determined by the following conditions. A very thin crystal is sensitive to mechanical distortions and x-rays may pass directly through it without any diffraction effect, whereas a very thick crystal shows strong attenuation of the radiation. A 1.5 mm thick crystal has been used. The crystal area (which is  $40 \times 120 \text{ mm}^2$  in the present case) has been chosen keeping in mind several factors. Fig. 4.9 shows how the x-ray beam emitted from a source continues to diverge after the diffraction from the crystal. For a 40 mm wide crystal the beam appears on the detector plane with a horizontal length of

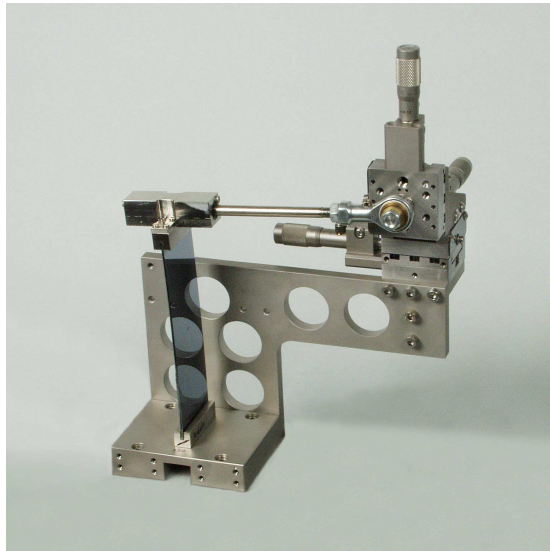


Figure 4.8: The crystal-bending device with the Si crystal.

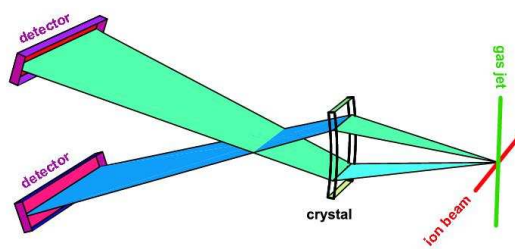


Figure 4.9: A three-dimensional view of reflected x-rays through the cylindrically bent Si crystal is shown.

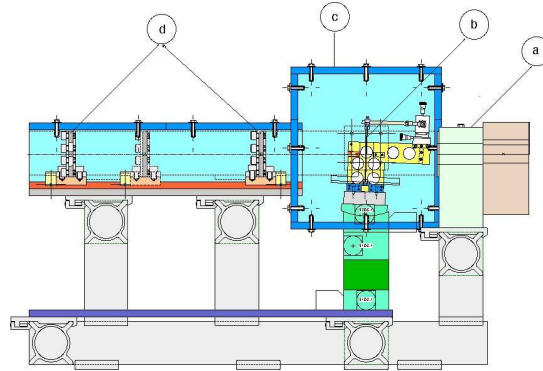


Figure 4.10: The slit assembly and the crystal arrangement of the spectrometer are shown. The part a) is the source positioner holder, b) the crystal, c) the lead shielding and d) the two slits.

200 mm [69], whereas the detector is only one-fourth of this size. Therefore, we don't need a wider crystal. On the other hand a smaller width reduces the number of transmitted photons and may be sensitive to bending stress. The length of the crystal (120 mm) was chosen keeping in mind the footprints appearing on the crystal (maximum at  $\pm 23.6$  mm for 600 mm distance between source-to-crystal and the wavelength range of our experiment [69]). The crystal radius was bent to a radius of curvature of approximately 2 m with the crystal bender shown in Fig. 4.8. The bending was made to produce a rocking curve width of  $50 \mu\text{rad}$  (which is the optimized width for resolution and efficiency of the spectrometer). The crystal bender follows a momentum bender philosophy [69]. At its short ends the crystal was glued into stainless steel mounting plates. By way of a rigid lever arm a suitable momentum was applied by micrometer screws. The lever arm is allowed to slide longitudinally as to avoid any unwanted horizontal force that would lead to the deviation from the desired cylindrical shape. We have measured the curvature of the crystals at the ESRF in Grenoble. For this purpose we used x-ray beams of 60 keV synchrotron radiation. The fluctuation of the local bending are on the order of  $\pm 2\%$ , the average radius of curvature measured is 2020 mm which is close to the required radius of 2000 mm. In addition tests in our laboratory have been performed using laser light and yielded a radius of 2016 mm agreeing with the former value well within the estimated measurement uncertainty of 5% [69].

#### 4.2.4 The Polychromatic Focus

Recalling Fig. 4.1 it can be seen that due to bending of the crystal the x-rays with different wavelengths, which are coming from the same source are focused at the same focal point on the optical axis after Bragg reflection. This focal point is called "polychromatic focus". Eq. 4.3 shows that the focal position is a function

of the radius of curvature of the crystal and the source-to-crystal separation. If we place slits on the optical axis, which allow only the passage of the focused x-rays, background x-rays that are not coming through Bragg reflections are blocked. We have positioned two such slits in front and behind the focal points of the spectrometer. For two different source positions 300 mm for stationary source and 600 mm for the gas-target, the positions of the focal points were 230 mm and 375 mm respectively. Therefore the positions of the slits were adjusted accordingly. The slit assembly is shown in Fig. 4.10.

### 4.2.5 The Detection Systems

At the beginning of this chapter the necessity of position sensitive detector in order to determine the positions of the spectral lines, which yields the wavelengths of the spectral lines was explained. For this purpose a first attempt with a normal germanium detector with a very narrow slit (the gap is around 100 micron) positioned in front of it can be exploited. A particular position of the slit allows to pass through a particular range of diffracted wavelengths. Therefore, if the detector is scanned (keeping the slit in front of it) along the direction of dispersion, it can cover a whole range of different lines. However, this is a feasible method for the test measurements with radioactive sources with high photon flux but not for the online measurement in our case, because only very few Lyman photons (typically 3-4 per hour) hit the detector. Therefore, we need a detector system, which has an intrinsic position sensitivity, so that the detector can be kept in fixed position, where, it can observe the expected spectral range. Before the experiment the check of proper alignment is very important and it was done in the scanning mode using the Yb calibration source. Since the source was very intense, scanning was possible. In order to enable the measurement in the scanning mode and also to move the position sensitive detectors, we installed a special detector stage at the end of the spectrometer, shown in part (d) of Fig. 4.7. The linear movement of this stage can be measured with an accuracy down to 5 micron using an incremental length encoder of 1 m length attached to the detector stage. In addition, few angle measuring devices were also placed on the detector stage, in order to monitor possible inclinations. A precision stepper motor was used for up and down movement of the detector stage. For the measurement, a couple of position sensitive microstrip germanium detectors (a one-dimensional and a two-dimensional) was developed in the FZ-Juelich [66, 72]. These two detectors are discussed separately in the following sections.

### 4.2.6 The Two-dimensional Microstrip Detector

A high performance two-dimensional position sensitive microstrip detector has been developed [72]. This has opened up several promising possibilities in the fields of precision x-ray spectroscopy and 2D x-ray imaging in the high energy

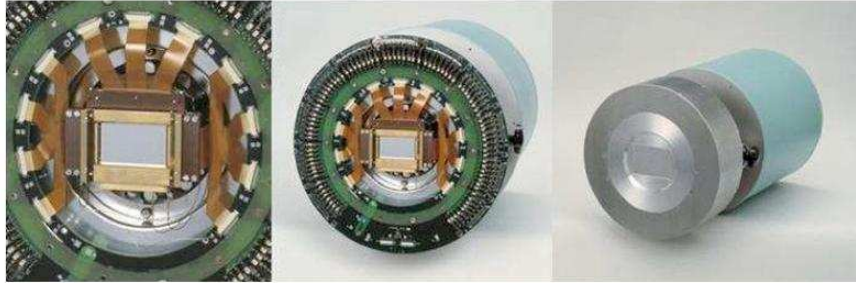


Figure 4.11: The two-dimensional microstrip detector. In the left side the detector without the cryostat cap and cover for the electronics is shown and on the right side the full view is presented [72].

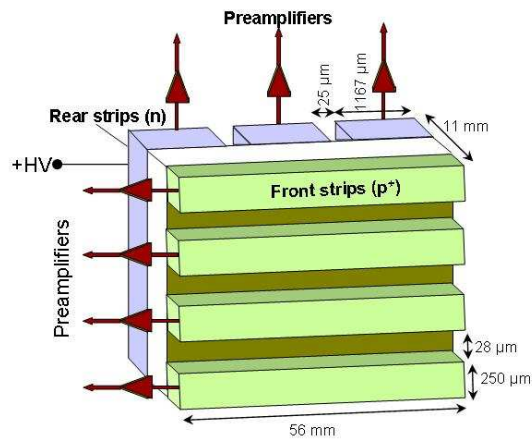


Figure 4.12: A schematic view of two-dimensional strips is shown (not to scale).

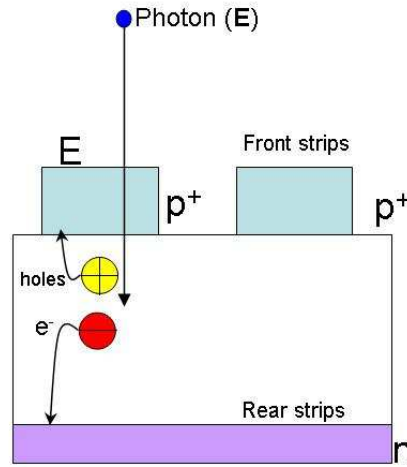


Figure 4.13: When a photon of energy  $E$  hits the detector, electron and hole pairs are produced. This picture shows a single-hit event where all holes generated by that event are collected by one  $p^+$ -strip and all electrons by one  $n$ -strip.

regime above 50 keV. At first a  $70 \times 41 \times 11 \text{ mm}^3$  Ge-diode was prepared from n-type high purity germanium. Boron was used to make the front  $p^+$ -contact with a  $0.33 \mu\text{m}$  thick Al layer. The rear contact was realized by a  $0.17 \mu\text{m}$  thick amorphous germanium (a-Ge-contact) layer with a  $0.2 \mu\text{m}$  thick Al layer. In the next step, on the  $p^+$ -contact a 128-strip structure with a pitch of  $250 \mu\text{m}$  and on the a-Ge-contact side 48 strips with a pitch of  $1167 \mu\text{m}$  were fabricated on an area of  $32 \times 56 \text{ mm}^2$ . The  $p^+$ -contact strips were separated by  $28 \mu\text{m}$  wide and  $15 \mu\text{m}$  deep grooves and for the a-Ge-contact by  $25 \mu\text{m}$  wide and  $10 \mu\text{m}$  deep grooves produced by plasma-etching technique. The energy resolution [FWHM] was measured with 60 keV photons from an  $^{241}\text{Am}$  source at a bias voltage of 1300 V with all the preamplifiers operating [72]. The values obtained for the 128  $p^+$ -strips on the front are  $(2.15 \pm 0.05) \text{ keV}$  for photons and  $(2.05 \pm 0.05) \text{ keV}$  for pulser signals, respectively, and  $(2.45 \pm 0.10) \text{ keV}$  and  $(2.30 \pm 0.10) \text{ keV}$  for the 48 rear strips. A time resolution [FWHM] of 50 ns at 60 keV is anticipated. Fig. 4.11 shows pictures of this detector and Fig. 4.12 gives a schematic view of the strip structure and most relevant geometrical dimensions. All strips are read out separately by preamplifiers.

### The Charge Sharing between Two Strips

The creation of electron-hole pairs, when a photon of energy  $E$  hits the detector is shown in Fig. 4.13. If the charge carrier creation occurs near a strip (let us say in the vicinity of one the  $p^+$  strips), then all holes produced by the photon will be collected by that strip ( $p^+$ ). Since the energy deposited to a strip is proportional to the number of collected charges, the  $p^+$  strip will receive the

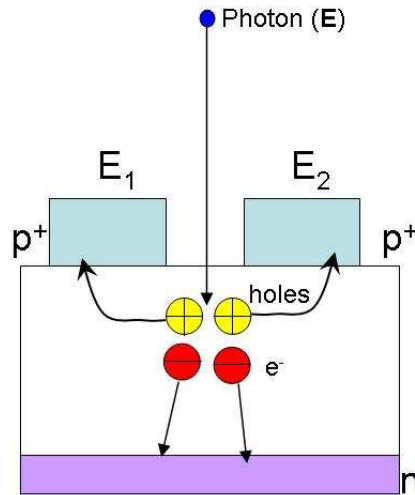


Figure 4.14: When a photon of energy  $E$  hits the gap in between two strips then the charges produced by this event may travel to more than one strip. Hence the energy of the incident photon is shared by more than one strip. The charge sharing between two  $p^+$  strips is shown here.

energy  $E$ . This process where all one-type charges are collected by only one strip is called a *single-hit* event. The above process is also true for the rear strips i.e.,  $n$ -type strips. So for an event if all electrons are collected by one  $n$ -strip and all holes by one  $p^+$ -strip, then each of these strips shows the energy  $E$  of the incident photon. Thus one may think that the total energy is  $2E$  instead of  $E$ . But note that this is just the way we calibrate the energy. That means actually each of them receives half of the total charge carriers (electrons+holes), i.e.,  $E/2$ , but this is represented as total energy  $E$ . The reason is that, we don't add up the energies of these two strips (rear and front) for an event, rather we see them as it is in order to produce a two-dimensional image of that event.

In the above discussion a *single-hit* process was explained. Now let's have a look at Fig. 4.14, where a photon hits in between two strips (let's say in between two  $p^+$  strips). In this case some of the created holes will follow the field lines towards one strip ( $p^+$ ) and others may follow to the other neighbor strip ( $p^+$ ) depending on which hole is close to which strip. Therefore, the total charge is shared between two neighbor strips. Let's call this process, where the total charges produced by an event is shared by two neighbor strips as *double-hit* event. However, the holes can also travel to the other  $p^+$  strips as well, in such case *multiple hits* can occur at the same time for one event. All these mechanisms are also true for the  $n$ -type rear strips. It's apparent from the above discussion that if the strip width is small and/or a groove width (the distance between two strips) is large, then photons have a fairly good chance to hit the gap and therefore more split events result [75]. The split charges can be summed

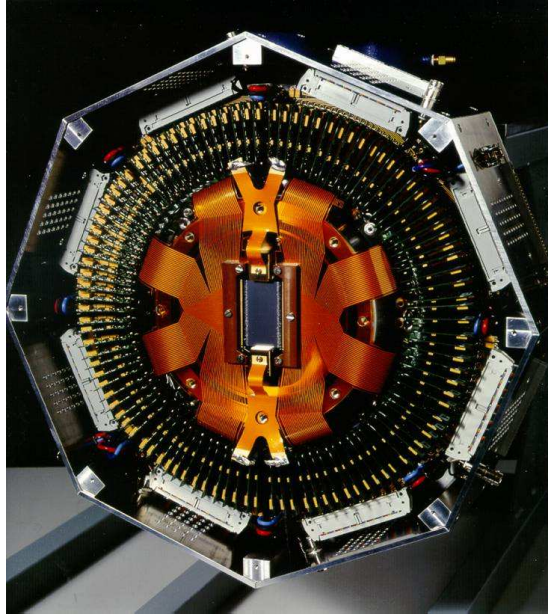


Figure 4.15: A front view of the one-dimensional detector without the cryostat cap and the cover for the detector [66].

up for each event and the original energy of that event can be reconstructed. The split energy reconstruction procedure will be discussed in the data analysis chapter. In this section a very basic description about charge sharing was given. In reality these processes are more complicated due to the detector construction, impurities, defects and multiple scattering of charges. The details can be found in the references from [72] to [82].

### 4.2.7 The One-dimensional Microstrip Detector

A structure of 200 strips has been realized on a block of pure germanium with dimension  $47 \times 23.4 \times 4.1 \text{ mm}^3$  [66]. The  $200 \mu\text{m}$  wide and  $23.4 \text{ mm}$  long strips are separated by  $35 \mu\text{m}$  wide grooves etched through the boron implanted front contact. A common  $0.6 \text{ mm}$  thick Li-diffused rear contact was used. Each of the strips has an energy resolution of about  $1.8 \text{ keV}$  [FWHM] for  $60 \text{ keV}$  photons. The coincidence between neighbor strips yielded a time resolution of  $70 \text{ ns}$  (see Ref. [66]). For our experiment, we connected 64 strips out of 200 for readout, which covered  $16 \text{ mm}$  across the dispersion plane. The detector physics is similar as described for 2D, the only difference is that the rear side has no strip structure. Fig. 4.15 shows the picture of the one-dimensional detector. To investigate the position sensitivity, the detector was mounted in the FOCAL test set-up and shifted in steps of  $50 \mu\text{m}$ . The position of the Yb- $\text{K}\alpha_2$  line centroid showed a linear variation with the position of the detector and could be determined with

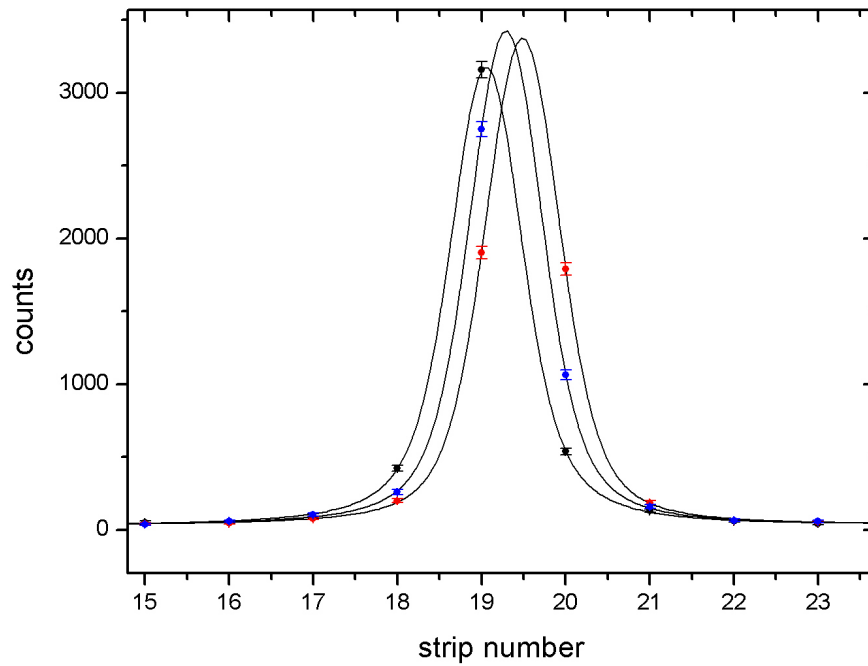


Figure 4.16: The one-dimensional detector (mounted in the FOCAL setup) has been shifted in steps of  $50 \mu\text{m}$  and the center of gravity of the Yb- $\text{K}\alpha_2$  line was observed. The solid lines represent a Voigt fitting to the experimental data points. [71].

an accuracy better than  $50 \mu\text{m}$  as shown in Fig. 4.16 [66, 71].

# Chapter 5

## The Experiment, Data Analysis and Interpretations

### 5.1 The Spectrometer Alignment

For the FOCAL experiment two spectrometers (FOCAL1 and FOCAL2) were aligned at the gas-jet target in the ESR. A schematic view of the whole experimental arrangement is shown in Fig. 5.1. The two spectrometers were aligned face-to-face i.e., along the same optical axis and each of them was placed perpendicular with respect to the beam axis. The spectrometers were positioned with the help of a pair of telescopes on the two sides of the gas-jet. The telescope alignment was done in the following way. At first the ion-beam axis was defined by using the reference axes of the quadrupole magnets in front and behind the target area. The "fiducial points" of these magnets served as actual reference points to determine the ion-beam axis coordinates. The gas-target middle point was determined from the "gas-ref" position on the floor. Thereby, the theoretical crossing point between the gas-jet and the ion-beam was determined. This enabled the alignment of the telescopes with respect to this crossing point and the direction of the ion-beam. The target area was open for the alignment purpose, that facilitated to align both the telescopes along the same optical axis with uncertainties of the angles both in the vertical and horizontal directions of about  $\pm 0.0023^\circ$  [83]. This yielded an alignment of each of the telescopes of  $90^\circ \pm 0.003^\circ$  with respect to the crossing point of the gas-jet and the ion-beam [83]. This special alignment of the spectrometers bears very important advantages for the experiment and will be explained in the following section.

#### 5.1.1 The Doppler Color Mixing Rule

Fig. 5.2 shows an x-ray source moving with velocity  $\beta$  ( $= v/c$ ) in the laboratory frame. The wavelength of an x-ray in the rest frame of the source is  $\lambda_{em}$ . A couple of detectors is kept at angles  $\theta$  and  $\pi - \theta$ , respectively, with respect to the

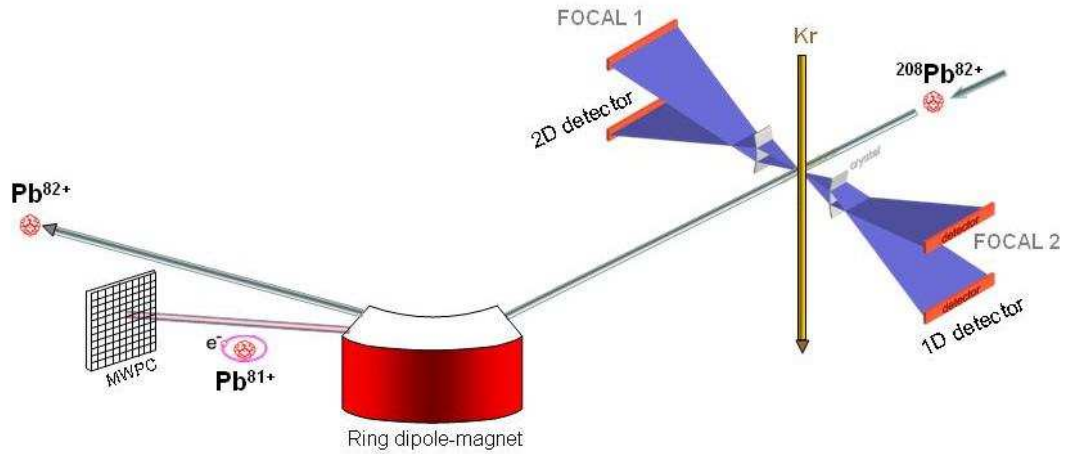


Figure 5.1: Two spectrometers FOCAL1 and FOCAL2 were aligned at the gas-jet target in the ESR. A beam of bare lead ions ( $^{208}\text{Pb}^{82+}$ ) was used as the projectile and krypton as the target gas. Down-charged  $\text{Pb}^{81+}$  ions produced by interactions in the gas target were deflected towards a particle detector (MWPC) by a ring dipole-magnet and the unchanged Pb ions continued to circulate in the storage ring. A coincidence measurement was performed between the down-charged particles and the detected x-rays.

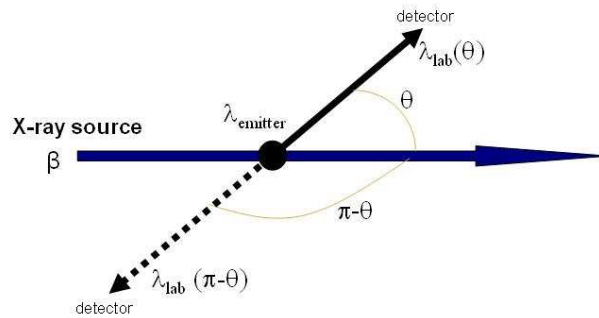


Figure 5.2: An x-ray source is moving with velocity  $\beta$ . Two detectors are kept at  $180^\circ$  angle with respect to each other. If  $\lambda_{emitter}$  is the emitted wavelength in the rest frame of the fast ion source, then the wavelengths in the laboratory frame seen by the two detectors are  $\lambda_{lab}(\theta)$  and  $\lambda_{lab}(\pi - \theta)$  respectively.

direction of the source. The wavelengths in lab frame seen by the two detectors are given by

$$\lambda_{lab}(\theta) = \lambda_{em} \cdot \gamma \cdot (1 - \beta \cos \theta). \quad (5.1)$$

and

$$\lambda_{lab}(\pi - \theta) = \lambda_{em} \cdot \gamma \cdot (1 + \beta \cos \theta). \quad (5.2)$$

where  $\gamma$  is the Lorentz factor. Adding these two equations, we obtain

$$\lambda_{em} = \frac{\lambda_{lab}(\theta) + \lambda_{lab}(\pi - \theta)}{2\gamma} \quad (5.3)$$

This is called the Doppler color mixing formula [16]. Clearly, this equation gives the emitter wavelength, which has no angle dependence term. Therefore, keeping two detectors at  $180^\circ$  with respect to each other yields no systematic uncertainty in observation angle caused by the arbitrary directions of the source (ions in our experiment). However, in our experiment the spectrometers have been aligned at  $180^\circ$  with an uncertainty of 0.04 mrad in both horizontal and vertical directions and the systematics caused by this uncertainty will be discussed in the error estimation section in detail. Differentiating equation 5.1 yields

$$\left(\frac{\Delta\lambda_{lab}}{\lambda_{lab}}\right)^2 = \left(\frac{\beta \sin \theta}{1 - \beta \cos \theta} \Delta\theta\right)^2 + \left(\gamma^2 \frac{\beta - \cos \theta}{1 - \beta \cos \theta} \Delta\beta\right)^2 + \left(\frac{\Delta\lambda_{em}}{\lambda_{em}}\right)^2 \quad (5.4)$$

where  $\Delta\lambda_{lab}$  and  $\Delta\lambda_{em}$  are the uncertainties of the wavelengths in the lab frame and the emitter frame, respectively.  $\Delta\theta$  and  $\Delta\beta$  are the uncertainties in observation angle and velocity of the x-ray source (which is ion-beam in our experiment), respectively. In terms of energy a similar expression can be derived

$$\left(\frac{\Delta E_{em}}{E_{em}}\right)^2 = \left(\frac{\beta \sin \theta}{1 - \beta \cos \theta} \Delta\theta\right)^2 + \left(\gamma^2 \frac{\beta - \cos \theta}{1 - \beta \cos \theta} \Delta\beta\right)^2 + \left(\frac{\Delta E_{lab}}{E_{lab}}\right)^2 \quad (5.5)$$

The emitter energy uncertainties  $\Delta E_{em}$  for two different beam energies (218.54 Mev/u and 20 Mev/u) are plotted in Fig. 5.3, which shows the dependence on  $\Delta\theta$  and  $\Delta\beta$  as a function of the observation angle. In our experiment we have used an ion-beam energy of 218.54 Mev/u (details in the next section). The  $\Delta\theta$  dependance was plotted using a value of  $0.003^\circ$ . The  $\Delta\beta$  dependance plots have been done using the two different values of  $2.12 \times 10^{-5}$  and  $2.70 \times 10^{-5}$ , which were estimated using cooler voltage uncertainties of  $\pm 3$  V and  $\pm 12$  V for 20 Mev/u and 218.54 Mev/u respectively (details about this calculation are given in the error estimation section). It is interesting to see in the lowermost plots that the emitter energy uncertainty due to  $\Delta\beta$  is much less at an observation angle of  $90^\circ$ , where we aligned the FOCAL spectrometers. The upper most plots in Fig. 5.3 shows the errors in emitter energy due to the uncertainties in the observation angle ( $\Delta\theta$ ). As we can see, close to the observation angle  $90^\circ$ ,  $\Delta E$  is large due to the finite value of  $\Delta\theta$ . Since we have aligned our spectrometers  $90^\circ$  with respect to the beam-axis this demands a very careful alignment of our spectrometers at this angle i.e., to minimize the value of  $\Delta\theta$ .

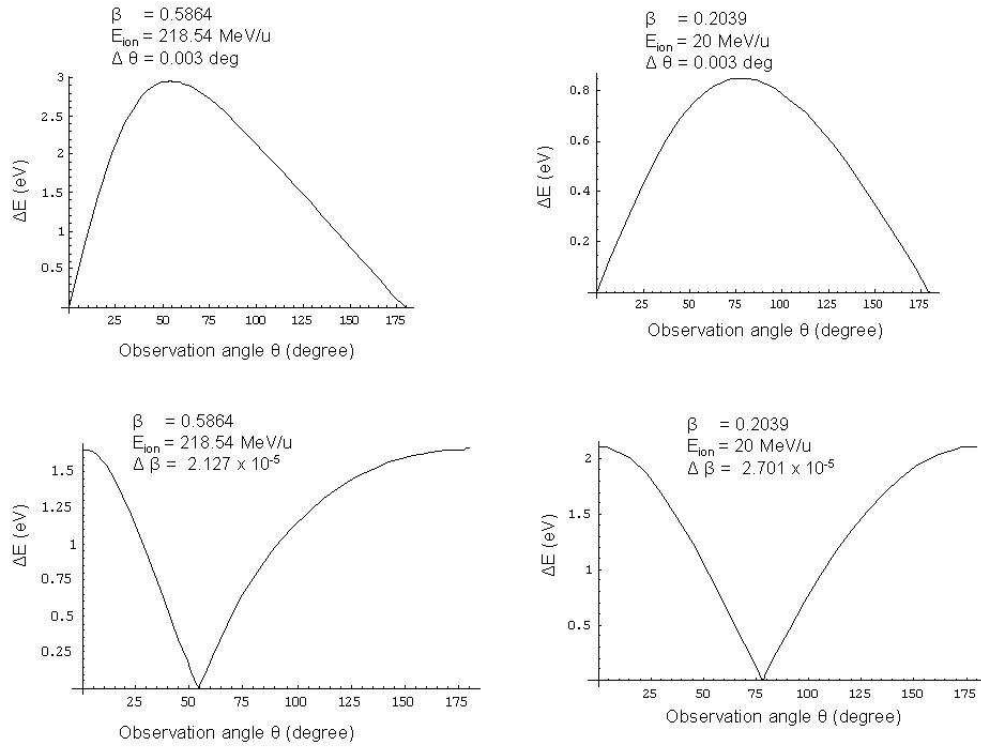


Figure 5.3: The uncertainty of the photon energy ( which is denoted by  $\Delta E$ ) in the emitter frame caused by the uncertainties of the observation angle  $\theta$  (the two uppermost figures) and ion-velocity  $\beta$  (the two lowermost figures) for the two different ion-beam energies of 218.54 MeV/u and 20 MeV/u respectively.  $\Delta\theta$  is the uncertainty of the observation angle in lab frame and  $\Delta\beta$  is the uncertainty of the velocity of the ion-beam.

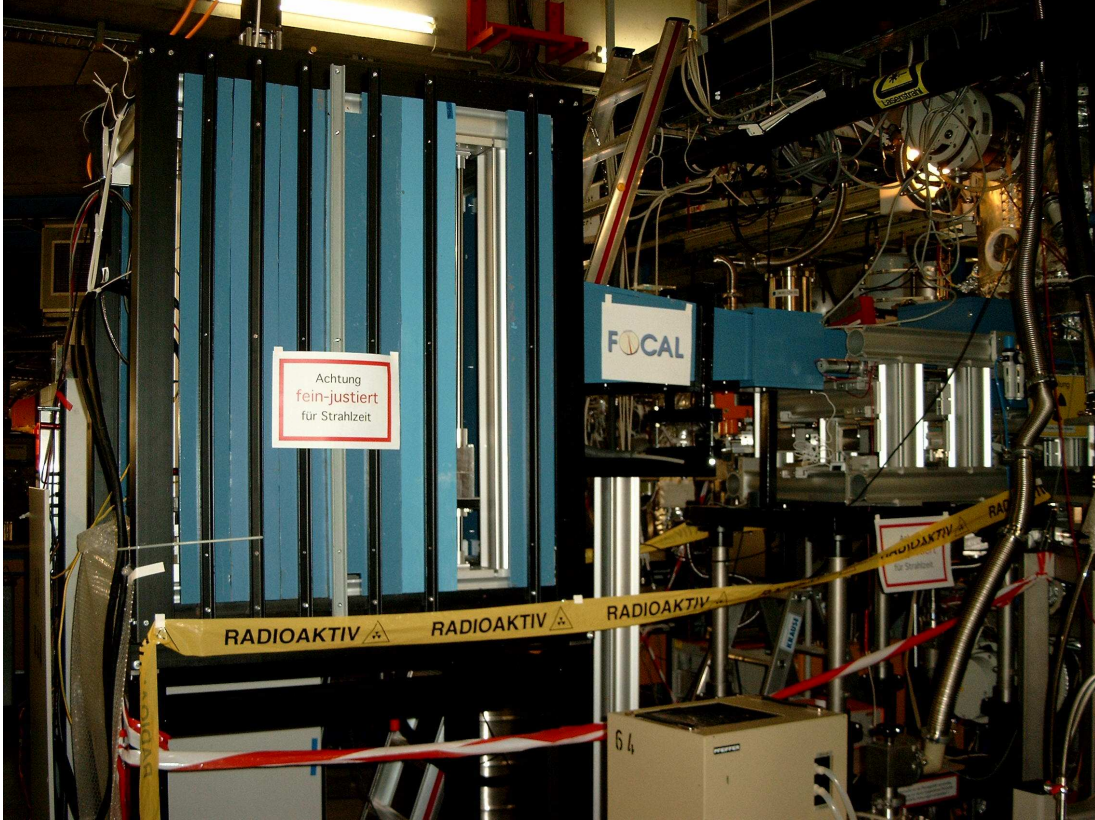


Figure 5.4: The FOCAL2 spectrometer in the gas-jet target area inside the ESR.

## 5.2 The Experimental Arrangement

A schematic view of the whole experimental arrangement is shown in Fig. 5.1. The picture of the FOCAL2 set-up is given in Fig. 5.4. A two-dimensional microstrip detector was placed in FOCAL1 and a one-dimensional microstrip detector in FOCAL2, respectively. Another small normal germanium detector (without position resolution) was placed at  $150^\circ$  with respect to the beamline for monitoring purposes of the interaction between the gas-jet and the ion-beam. The reason was that, since the spectrometers had very low count rate for the Lyman- $\alpha$  photons compared to the normal Ge detector (at least 10 times less), it was difficult to monitor the status of the experiment using the spectrometers. Therefore, the normal Ge detector was essential for that purpose.

For the experiment a bare  $^{208}\text{Pb}$  ion-beam was used as projectile and a krypton gas-jet was used as target (as shown in Fig. 5.1). The Ly  $\alpha_1$  transition in lead was used, which had a predicted value of 77.934 keV in the emitter frame of reference. The FOCAL spectrometer has been optimized for the energies close to 60 keV [68, 69]. This energy in the lab frame can be obtained by taking into account the Doppler shift of the emitter energy (i.e., 77.934 keV) by choosing

the suitable ion-beam energy of 218.54 Mev/u ( $\beta = 0.58647(2)$ ). The reason to choose this particular value was that we wanted the laboratory energy of Ly  $\alpha_1$  to be close to 63.121 keV, so that the Ly  $\alpha_1$  line hits the detector exactly at the same position as the calibration line of energy 63.121 keV from the  $^{169}\text{Yb}$  source. This has made the analysis easier, which will be discussed in the data analysis section.

The target was a Kr gas-jet with a density of approximately  $7 \times 10^{11}$  per  $\text{cm}^3$ . Kr was chosen instead of low- $Z$  gases (Ar or  $\text{N}_2$ ), simply because it has more electrons and the electron capture cross section of the bare ions increases linearly with the number of electrons in the target atom [57].

The experiment was performed in the following way. At first a beam of fully stripped lead ions from the SIS was directly injected into the ESR. The beam was then cooled by electron cooling in the electron cooler of the ESR. The cooling guaranties a good beam quality with an emittance of about  $0.1 \pi$  mm mrad, a momentum spread on the order of  $10^{-5}$  and a squeezed diameter of about 5 mm [54]. The limits to these numbers come from the space charge potential of the ions and this restricts the total number of stored ions to about  $10^8$  [54]. Although the cooling time ( $\sim 40$  ms [17]) is much less than electron capture time by the process of radiative recombination ( $\sim 20$  s [17]), capture is a probable process for the loss of bare ions during the cooling process. The bare lead ions, which captured electrons, follow a trajectory different from that of bare lead ions. Therefore, they were easily blocked by the scraper just next to the dipole magnet behind the cooler. After the cooling process the gas-jet was switched on, the gas-filled multi-wire proportional counter (MWPC) (as shown in Fig. 5.1) was moved inside the beam pipe in order to detect the down-charged  $\text{Pb}^{81+}$  ions, which appeared after capturing an electron in collisions with the atoms of the gas jet. The jet remained on for a measurement time of about 1 min and after that it was switched off, because the number of bare lead ions was decreased from an initial current of typically 3 mA to less than 1 mA. Therefore, a new cycle started with the injection of fresh  $\text{Pb}^{82+}$  ions. A complete cycle took around three and half a minute.

The x-rays emitted by the interaction between gas-jet atoms and ions were detected in coincidence with the down-charged  $\text{Pb}^{81+}$  ions. The time of flight of the down-charged ions from the interaction point to the particle detector (MWPC) was approximately 100 ns. This means that the x-rays, which hit the strip detector corresponded to a down-charged lead ion, which was detected in the particle detector 100 ns after that x-ray. A triggering scheme of the electronic set-up was implemented incorporating this fact.

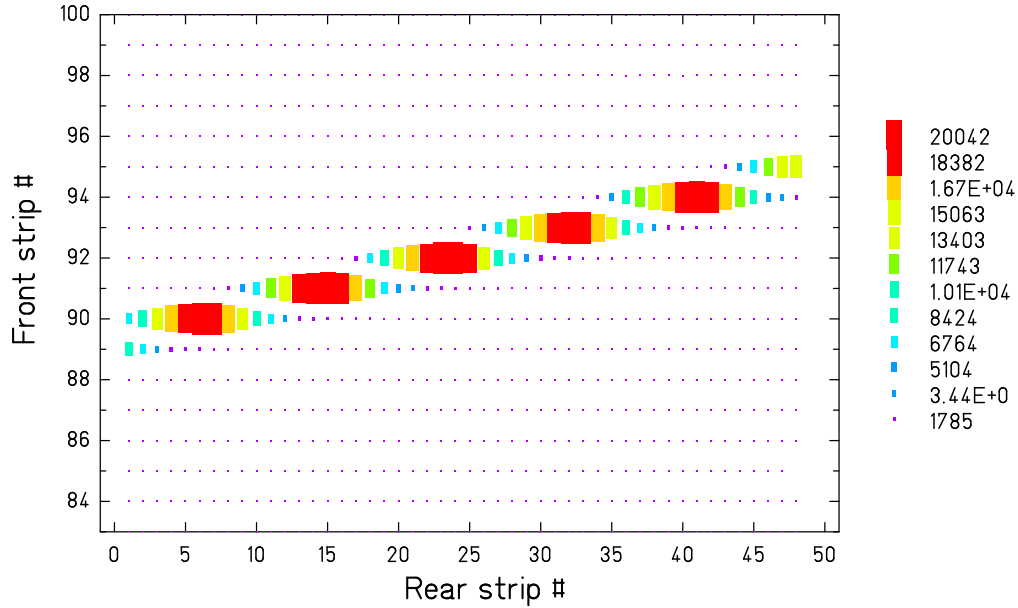


Figure 5.5: The two-dimensional image of the Yb gamma-ray line of 63.121 keV. The different colors represent the intensity distribution of the photons.

## 5.3 The Data Analysis and Interpretation of the Results of the FOCAL1(2D) spectrometer

### 5.3.1 The Analysis of the Calibration Spectrum

The image of the  $^{169}\text{Yb}$  63.121 keV calibration line observed in the two-dimensional detector placed in the FOCAL1 spectrometer is shown in Fig. 5.5. The spectrum was obtained integrating all the reasonable calibration files assembled throughout the beam-time. We had an effective beam-time of about 10 days and we performed calibration measurements of the spectrometers almost in regular intervals during the beam-time. The purpose of doing the calibration regularly was to see if any possible drifts or shifts of the calibration line in the detector occurred. An energy drift can be possible due to an accidental change in some electronics parameters (e.g., the amplification of the spectroscopy amplifier) and a shift of the lines can happen due to any fluctuation of the detector position along the direction of dispersion.

As can be seen, the calibration line is tilted. In principle the calibration line hits the detector horizontally, but we have tilted the detector by an angle of  $1.32^\circ$ , therefore the line appears to be slanted and the reason will be explained in the next section. The calibration line reflected from the crystal has a continuous distribution along the horizontal direction. However, one can see several discrete

patches instead of a continuous line. The reason is the digitization of the intensity distribution due to the pixel structure of the detector. Each of these patches shows again a horizontal intensity distribution (i.e., along the rear strip axis). That is, the center of a patch has maximum number of counts (where the major part of the spectral line hits) and decreases at the two sides along the horizontal direction. The main reason of such a decrement of the intensity along the horizontal direction is due to the charge sharing between two horizontal strips (i.e., between two front strips). That means, when a part of the spectrum is hitting in between two front strips, the energy is shared by these two strips, resulting in the decrement of the counts at 63.121 keV energy. The detailed structure of the calibration line can be understood in a three-dimensional view shown in Fig. 5.6. In this picture the front strip axis is energy calibrated in order to show the energy distribution (the green part of the spectrum) along the axis of dispersion. Along the rear strip axis the digitized intensity distribution is apparent. Though a very narrow energy window condition on the pulse-height spectrum was chosen to produce this intensity distribution, still a small peak around 61 keV is partially visible in Fig. 5.6, which is the Yb-K $\beta_2$  line.

In the next step of the analysis, the centroid of the calibration line has to be determined, i.e., the center of the line along the axis of dispersion (the front-strip axis). In order to do that the contents of every pixel (total 48 pixels) were projected onto the front-strip axis and fitted by a Gauss function to estimate the mean position of each projected peak in terms of the front strip number. During fitting of the peaks, mostly the mean position was the free fitting parameter, because the peaks are typically 1-3 data points, which requires less than 3 free fitting parameters in order to reach the convergence in the least square fit calculation (see Fig. 5.7). Note that the front strip numbers (e.g., Fig. 5.5 or 5.8) denote the parameter numbers and the absolute values of these numbers are not important, because we have performed relative measurement of the centroids between the Ly  $\alpha_1$  and the calibration line. Three examples of projected and fitted intensity distributions are shown in Fig. 5.7.

The mean positions on the front-strip axis for all 48 pixels are plotted in Fig. 5.8. The oscillating structure of this plot is the consequence of three different facts namely, the intensity sharing between two front strips, the resolution of the electronics limited to one strip width and the digitization of the intensity distribution. The centroids corresponding to the pixels for vertical strip numbers 4, 5 or 6 (see Fig. 5.7 and 5.8) are likely to stay along the center of a front strip i.e., almost horizontally in Fig. 5.8. This is because for these pixels the x-ray shines almost over one front strip and in that case the photon hit is uncertain by one strip width because of the electronics resolution. As a result the intensity distribution fills the whole front strip regardless where the x-ray photon hits. Therefore, the centroids of these distributions tend to lie almost on the middle of that front strip. Now, slightly off from these vertical strips, where the x-ray shines over two front strips, i.e., the intensity of the line is shared significantly between

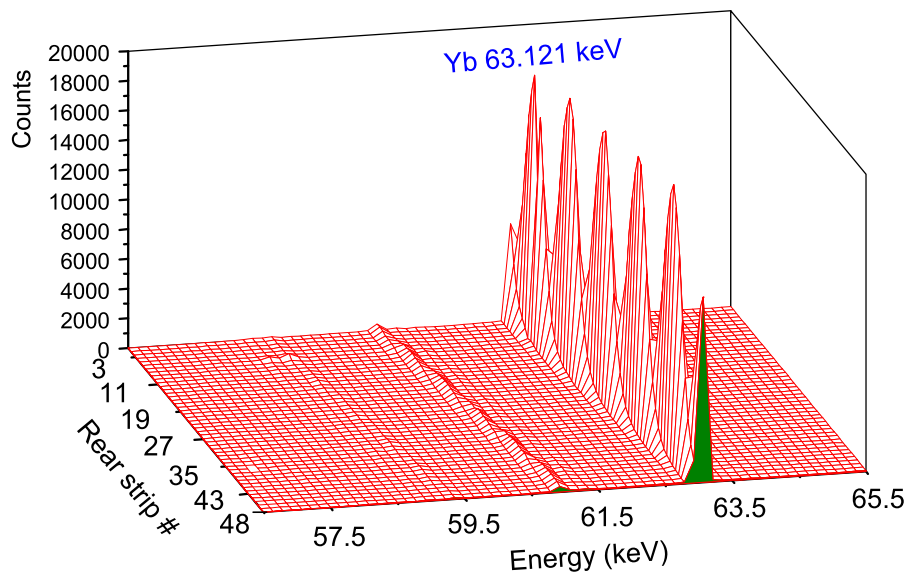


Figure 5.6: A three-dimensional plot of the 2-D image shown in Fig. 5.5. The front strip axis is energy calibrated. Along the rear strip axis the photon intensity distribution is noticeable.

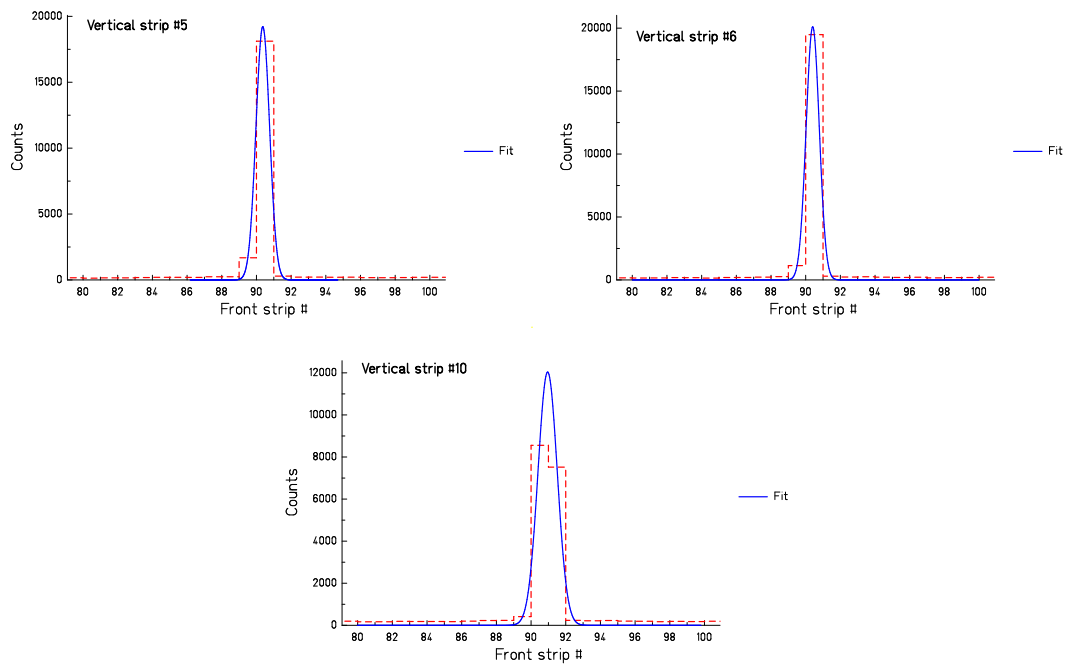


Figure 5.7: The pixels corresponding to the vertical strips 5, 6 and 10 are projected onto the front-strip axis. In order to estimate the mean positions of the peaks, a Gauss function has been fitted.

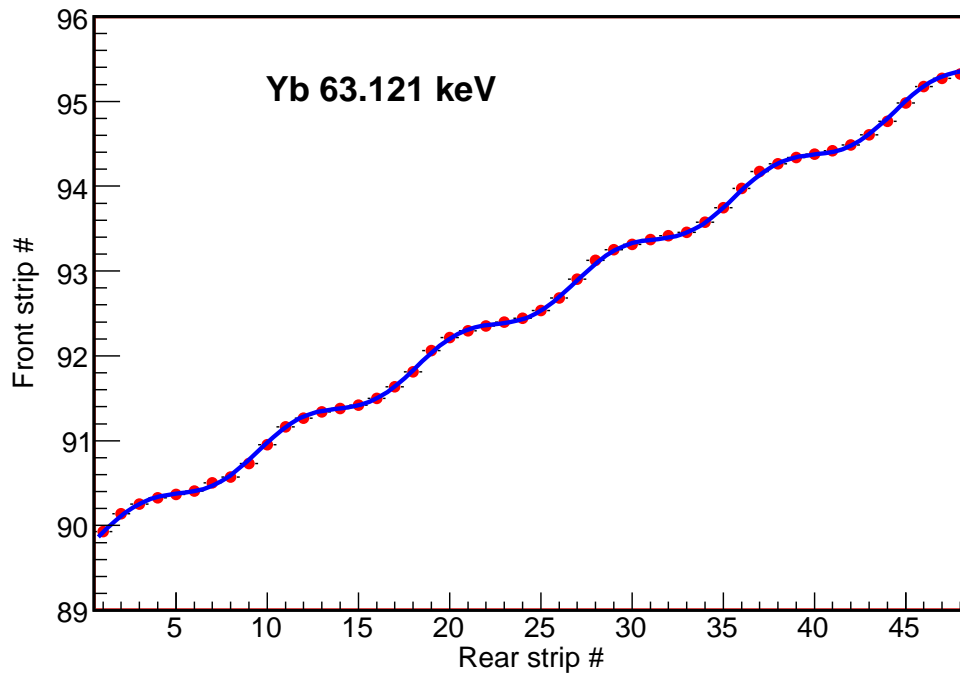


Figure 5.8: The content of each pixel of Fig. 5.5 has been projected onto the front-strip axis (e.g., Fig. 5.7) and determined the mean positions of the intensity distributions. Solid circles in this picture represent the mean positions of the intensity distributions of all 48 pixels and the solid line is a fit to the data points. The oscillating structure is due to the intensity sharing between two front strips, the resolution of the electronics limited to one strip width and the digitization of the intensity distribution.

two strips, the position of the peak-centroid on the front-strip axis depends on the shared intensity ratio of these two neighbor strips. For example, the projected content of the pixel corresponding to the vertical strip number 10 (see Fig. 5.7), the x-ray shines almost equally over the two front strips 91 and 92. Therefore, the centroid of the intensity distribution is determined depending on the ratio of the two intensities of the strips 91 and 92 (see the fit in Fig. 5.7), which stays close to the middle of these two strips. Hence, in contrast to the centroids of pixels corresponding to the vertical strips 5 or 6, which tend to stay horizontally, i.e., at the middle of one strip, the centroids of pixels corresponding to the vertical strips 9 or 10 stay in between two front strips. These two different effects produce the periodic structure of the mean peak positions in Fig. 5.8. The above mentioned effects are clearly noticeable, because of the digitization of a large number of counts of the calibration line. In order to determine the centroid of this line, the data points of Fig. 5.8 have been fitted using the following function

$$Y = aX + b \cdot \sin(cX + d) + e \quad (5.6)$$

where  $a$ ,  $b$ ,  $c$ ,  $d$  and  $e$  are the fitting parameters. The determination of the line-centroid from the fitting parameters will be discussed in the section of the determination of the wavelength centroid.

### 5.3.2 The Analysis of the Online Measurement

It was mentioned before that the spectrometers eventually see only 3-4 Lyman photons per hour, which requires the suppression of background photons as much as possible. In order to reduce the background photons and produce a clean Lyman spectrum, three different possibilities in the data analysis have been exploited, namely the condition on time, energy and position. This is explained with pictures of the coincidence time spectrum and the pulse-height spectra shown in Fig. 5.9 and 5.10, respectively.

The peak in the coincidence spectrum denotes a time difference between an x-ray hit in the 2D detector and the corresponding down-charged particle hit in the particle detector. We have used TDCs in the experiment with a bin size of 1.6 ns, which was used to calibrate the time spectrum. The full width at half maximum of the coincidence spectrum is about 90 ns. The anticipated time resolution of the 2D x-ray detector was better than 50 ns and that of the particle detector less than 90 ns and they are added quadratically in this case [85, 86]. The time spectrum was obtained by putting iteratively proper conditions on the positions of Lyman lines on the detector along the axis of dispersion. The reason is that the Lyman lines are lying on particular strips along the axis of dispersion, therefore, the coincidence time for Lyman photons is defined by those particular strips.

The pulse-height spectrum in Fig. 5.10 has been obtained with and without applying conditions on the coincidence time spectrum. When no time condition

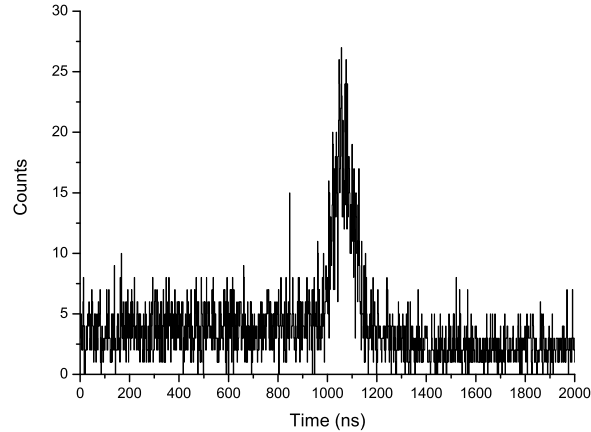


Figure 5.9: The coincidence time spectrum between the 2D x-ray detector and the particle detector.

is applied, lots of background photons show up. The spectrometer was covered with a lead shielding. The strong background radiation emitted during beam operation ionized the K-shell electrons of these lead atoms, resulting in fluorescence radiation at energies around 74 keV (Pb-K $\alpha$ ) and 85 keV (Pb-K $\beta$ , -K $\gamma$  etc), which can be seen in the pulse-height spectrum. However, if we apply a time condition these background photons disappear and a clean Lyman pulse-height spectrum is produced. Now, by applying proper energy windows (57-68 keV) to the Ly  $\alpha_1$  and Ly  $\alpha_2$  pulse-height spectra, a two-dimensional intensity distribution has been obtained as shown in Fig. 5.11. This 2D image is the result of choosing suitable conditions on time and energy and is random subtracted. A sharp energy window on the pulse-height spectrum of Ly  $\alpha_1$  and Ly  $\alpha_2$  is important. The reason is that the neighbor strips share split events and other low or high energy background photons. A bigger window than the pulse-height energy distribution would allow these high or low energy events and as a result the intensity distribution on the strips of the 2D image may change in an unexpected way, which in turn may introduce a shift of the centroid position of the intensity distribution on the front-strip axis. This will be more clear when the analysis of the projected intensity distributions of the Lyman lines will be discussed. Note that Fig. 5.11 was obtained only with single-hit events. The split events (i.e., the double-hit events) will be recovered and added to the intensity distribution.

Now, the reconstruction of the the split Lyman events will be discussed. Let me start with the example of the Yb 63.121 keV split events, because it has a huge number of counts, which produces recognizable pictures. Exactly the same method will be applied in case of the Lyman events reconstructions. Fig. 5.12 shows the pulse-height spectrum of split events of the Yb 63.121 keV photons

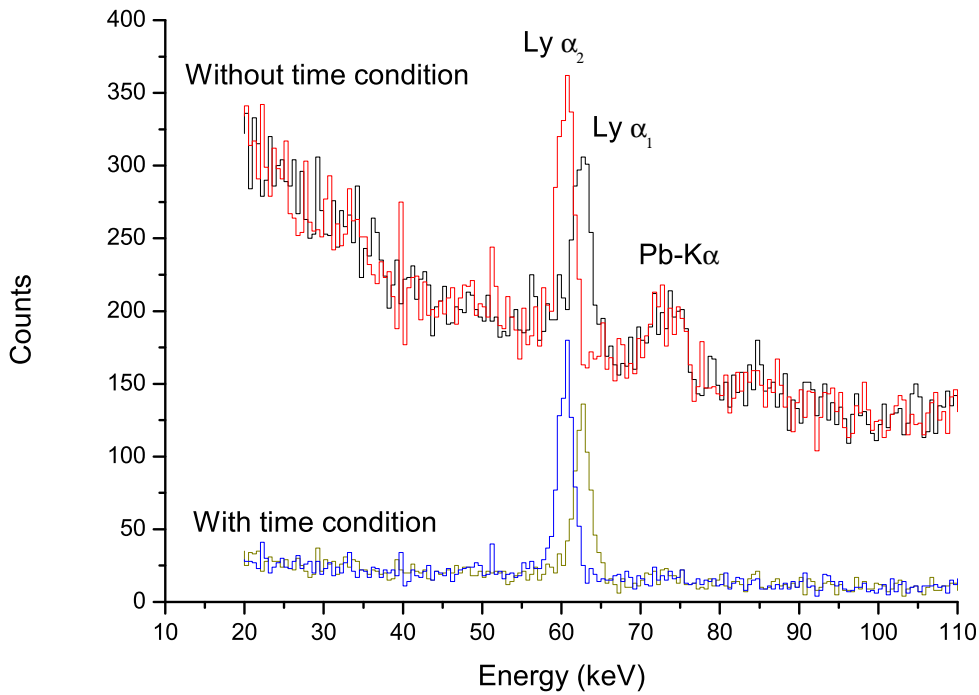


Figure 5.10: The pulse-height spectra of different strips of the 2D detector obtained in the online measurement are merged on the same picture. The uppermost spectrum was obtained without any time condition, therefore the Pb fluorescent photons ( $\text{Pb-K}\alpha$ ) from the lead shielding are visible besides the Lyman lines from  $\text{Pb}^{81+}$ . Applying proper time condition produces clean Lyman lines as shown in the lowermost spectrum.

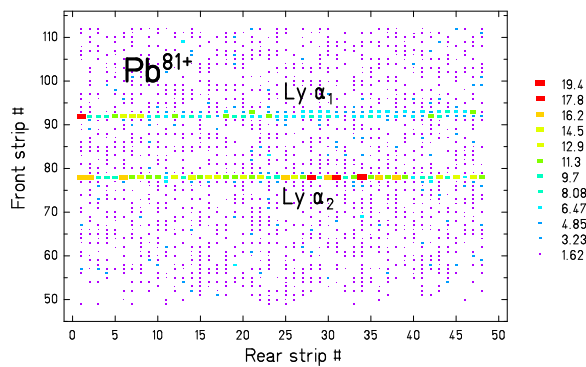


Figure 5.11: A two-dimensional intensity distribution of the  $\text{Ly } \alpha_1$  and  $\text{Ly } \alpha_2$  lines obtained by choosing proper windows on time and energy. Only single-hit events are considered and the spectrum is random subtracted.

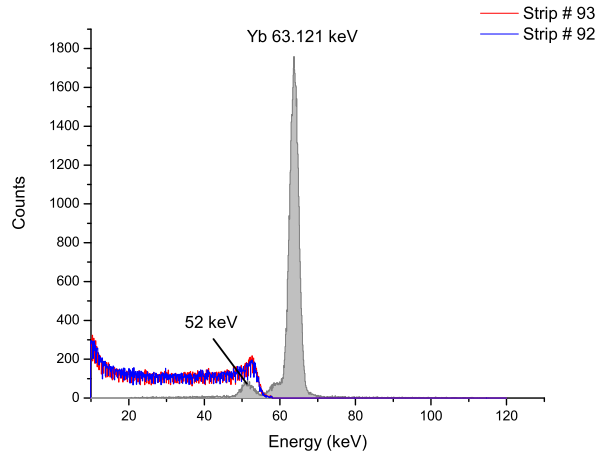


Figure 5.12: The split events of 63.121 keV calibration photons between the two front strips 92 and 93 are shown in the unfilled portion, where the energies of split events range from 10 keV to 55 keV. The reconstructed events are shown by filled areas of the pulse-height spectrum.

between two front strips 92 and 93 respectively.

A 63.121 keV photon can be split up in any combination of two energies below 63.121 keV depending on which place the photon hits in between the two strips. If the photon hits close to strip number 92, then this strip gets the biggest part of the split energy. Only split events between 10 keV and 55 keV have been considered, because below 10 keV there is a huge noise in the pulse-height spectrum. Adding up the split energies for every event, we obtain the reconstructed events of 63.121 keV energy as shown by the filled portion of the pulse-height spectrum. The FWHM of the sum peak is 2.81 keV. The summed up spectrum shows some events at energies lower than 63.121 keV. The peak at 52 keV is an escape-peak and a little shoulder comes from Compton scattered photons.

If the energies of the split events of one strip are plotted on one axis and the same for the neighbor strip on the other axis, a continuous line of 63.121 keV as shown in Fig. 5.13 arises, which shows that there was no charge loss for an event in the groove.

The reconstructed 63.121 keV events have been distributed in the strips in the following way. If the photon hits close to a strip, then most of the charges (in other word the bigger part of the split energy) goes to that strip. So the event (photon) is most likely to incident on that strip. Therefore, by looking to the charge ratio between two neighbor strips for every event and setting a condition on the sum peak of the reconstructed pulse-height spectrum, the events can be accumulated on the strips. For the Lyman events the above procedure was

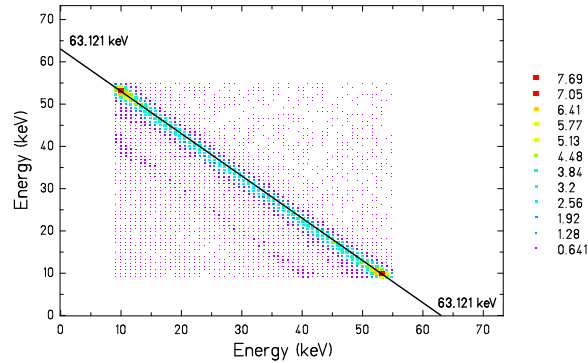


Figure 5.13: The split energies of strip number 91 are plotted along the x-axis and same for strip number 92 along the y-axis, where both the axes are energy calibrated. A consistent 63.121 keV line shows that there was no charge loss in the groove between strip number 91 and 92.

followed with applying a suitable time condition and a reconstructed intensity distribution on the strips has been obtained as shown in Fig. 5.14.

The reconstruction was done only for the front strips. Since the rear strips are almost 5 times wider compared to the front strips and the rear gap width is almost same as the front gap width, the charge splitting in the rear strips was extremely small, hence they have not been considered.

The intensity of the double-hit events (i.e., the reconstructed events) of Fig. 5.14 is added up with the single-hit events (Fig. 5.11) and the 2D image of the intensity distribution is obtained as shown in Fig. 5.15.

A comparison of the intensities between single-hit and double-hit events is shown in Fig. 5.16. We have 18.7% Ly  $\alpha_1$  and 13.7% Ly  $\alpha_2$  reconstructed events. The splitting for Ly  $\alpha_1$  was larger, because a significant part of this line hit the gap between strip number 92 and 93, whereas Ly  $\alpha_2$  laid almost on one strip (strip number 78). A three-dimensional view of the intensities of the Lyman lines is shown in Fig. 5.17. The front-strip axis is energy calibrated, which shows the energy distribution of the Lyman lines along the axis of dispersion.

In order to determine the centroid of the Ly  $\alpha_1$  line on the front-strip axis, the content of each pixel (i.e., each slice of Lyman intensity distribution of Fig. 5.17) was projected onto the front-strip axis and the mean positions of the peaks in terms of front strip number was determined by fitting a Gaussian function. A fitted projection is shown in Fig. 5.18 as an example.

The centroids of the Ly  $\alpha_1$  and Ly  $\alpha_2$  lines for all 48 pixels are plotted in Fig. 5.19 and linear fits are made. The fitting parameters will be incorporated in the determination of the line centroid.

Now looking at the figures 5.15 and 5.5 one can see that the Lyman lines are rotated with respect to the calibration line. In the following subsection an

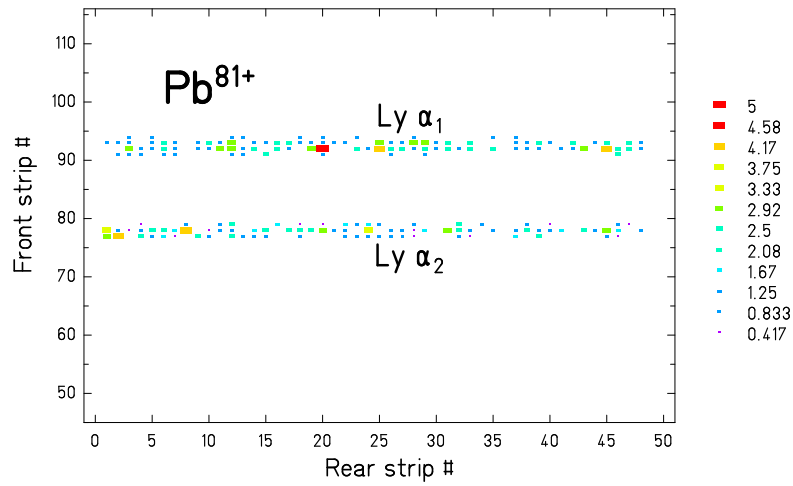


Figure 5.14: The intensity distribution of reconstructed Lyman photons is shown. The random events are subtracted.

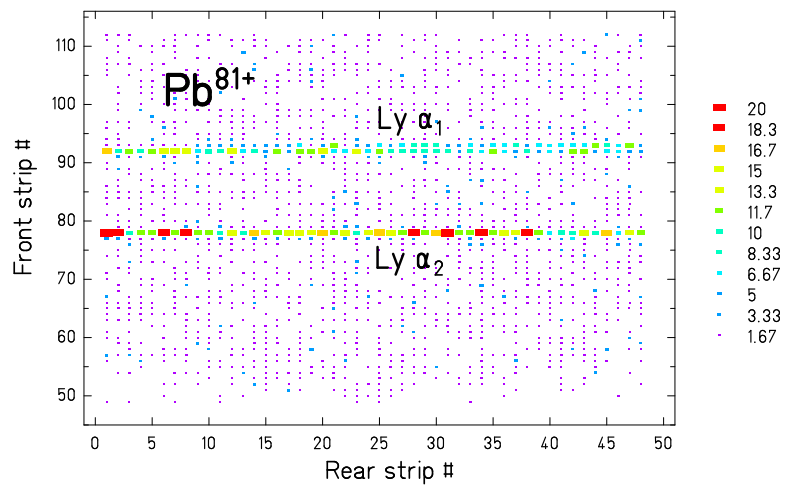


Figure 5.15: The single-hit and reconstructed split events were added up in this spectrum.

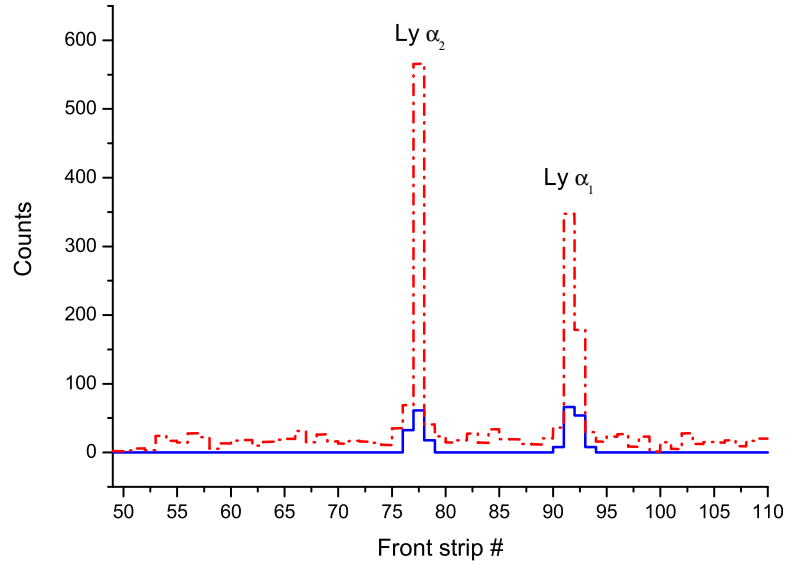


Figure 5.16: The dotted line represents the number of the single-hit events and the solid line of the double-hit events.

explanation is given for this rotation, when we perform measurement with a very fast x-ray source (59% of the speed of light in our case).

### The Doppler Rotation

In order to understand the reason for the rotation, a simplified crystal optics geometry has been drawn in Fig. 5.20. Only the upper reflected x-rays are considered in this case. A fast x-ray source is moving parallel to the meridional plane of a cylindrically bent crystal. The optical axis is defined by the line ABF, which is passing through the center of the crystal and the detector plane. Three x-rays are considered, which are emitted from the point A, incident on the crystal and denoted by AE, AC and AD. The x-ray AC, which is crossing the vertical plane at the middle of the crystal makes a  $90^\circ$  angle to the direction of the x-ray source and finally hits the detector plane at point O after the diffraction. AD has an angle  $90^\circ + \psi_1$  and AE  $90^\circ - \psi_2$  with respect to the direction of the source. Looking at the Doppler formula for the wavelength shift (Eq. 5.1), we find that the wavelength  $\lambda_1$  of x-ray AD for  $90^\circ + \psi_1$  is larger than the wavelength  $\lambda_2$  of x-ray AE for  $90^\circ - \psi_2$ . The Laue-Bragg equation  $2d\sin\theta = \lambda$  yields that for the larger wavelength  $\lambda_1$ , the deflection angle  $\theta_1$  is bigger and similarly, for  $\lambda_2$  the angle  $\theta_2$  is smaller. Therefore, the x-ray AD hits the detector plane somewhere down the point O at H and the x-ray AE somewhere up the point O at G on the detector plane. If we make a linear fit through the points G, O and H, a

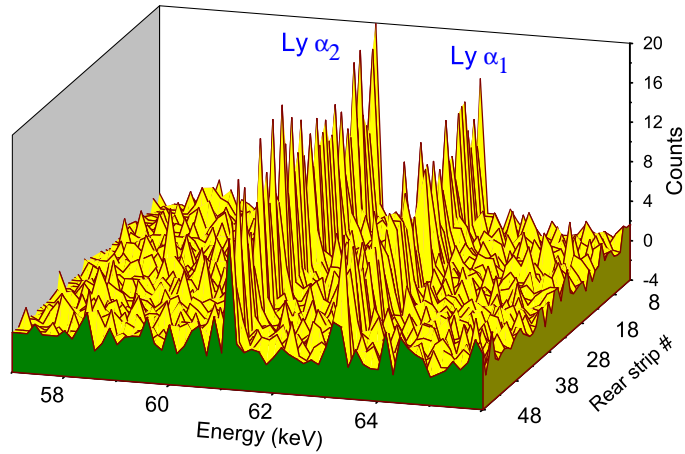


Figure 5.17: A three-dimensional view of the spectrum of Fig. 5.15 is shown. The front-strip axis is energy calibrated. The many peaks in a row along the rear-strip axis are the consequence of the digitization of the continuous intensity distribution. The spectrum is random subtracted, therefore, some negative counts can be seen.

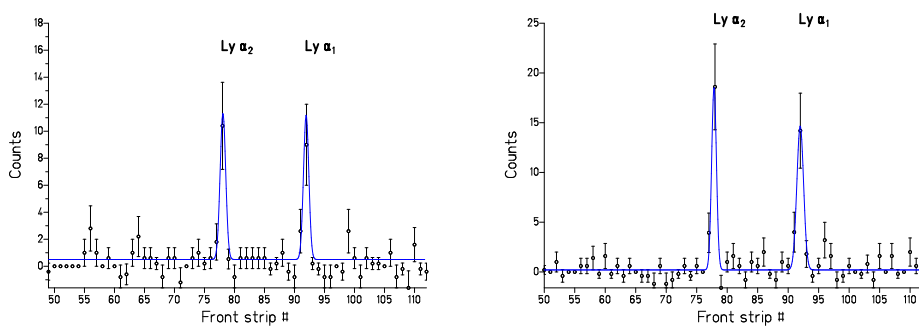


Figure 5.18: Two pixels corresponding to rear strip number 4 (left) and 6 are projected onto the front-strip axis and a Gaussian function is fitted (solid lines) in order to determine the centroids of the Lyman lines.

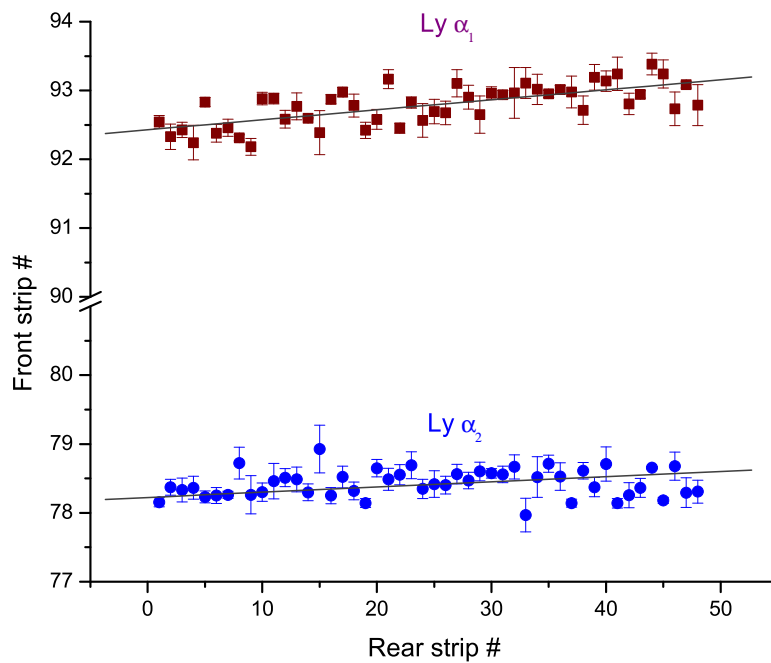


Figure 5.19: The centroids of the Ly  $\alpha_1$  (solid square) and Ly  $\alpha_2$  (solid circle) lines for all 48 pixels are plotted. The solid lines are the linear fits to the data points.

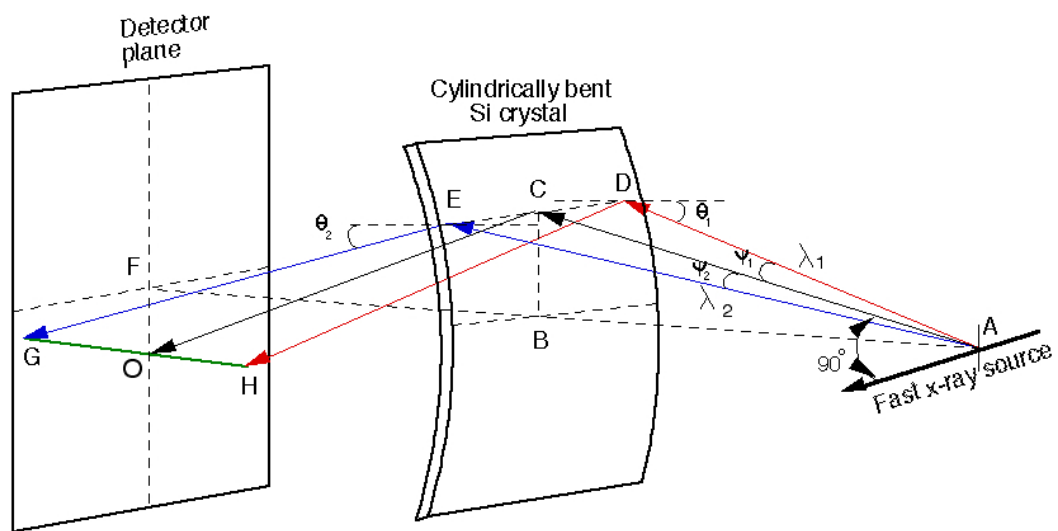


Figure 5.20: A fast x-ray source is moving parallel to the meridional plane of a cylindrically bent crystal. The x-rays considered here are emitted from a point lying on the optical axis ABF.

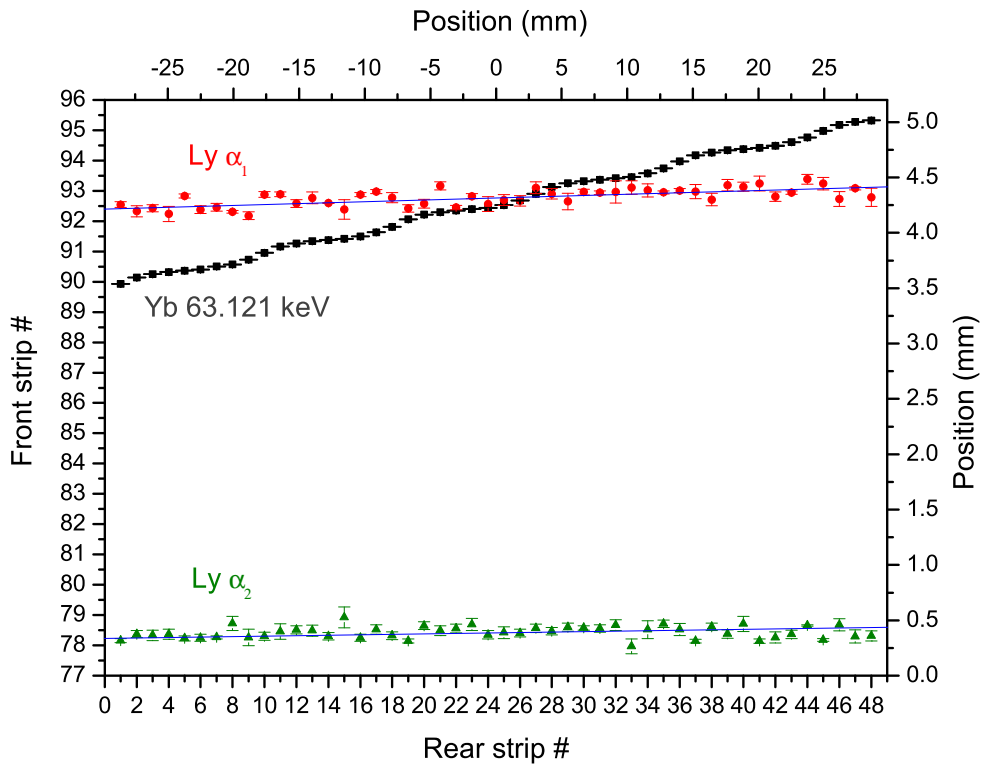


Figure 5.21: The centroids of the projected peaks for all pixels of the  $\text{Ly } \alpha_1$ ,  $\text{Ly } \alpha_2$  and  $\text{Yb } 63.121 \text{ keV}$  calibration lines are plotted. The Doppler rotation of the Lyman lines with respect to the calibration line is apparent.

spectral line is obtained which is inclined with respect to the horizontal axis. If a stationary source is considered in point A, then the wavelengths of AD and AE will be the same, hence they will hit the detector plane on the same horizontal line. Note that for the lower reflections from the crystal the sign of the line slope will be just opposite to that for upper reflections.

Merging the Figs. 5.8 and 5.19 into Fig. 5.21 makes the Doppler rotation apparent. The  $\text{Ly } \alpha_1$  line has a different slope than the  $\text{Ly } \alpha_2$  line. This is due to the fact that they have different energies (a difference of about 2.65 keV) and therefore different degrees of Doppler rotations.

In the above geometry a simple case was considered. However, for the FOCAL spectrometers a detailed crystal optics formulation was done in Ref. [68]. The vertical position of a reflected x-ray on the detector plane can be approximately

written as

$$X = R \cdot \left[ \frac{\sin(\theta + \chi + \tau)}{\cos(\theta + \chi + \tau)} - \frac{\sin(\theta + 2\chi)}{\cos(\theta + \chi + \tau)} - \cos\chi \cdot \tan(\theta + \chi + \tau) \right] \quad (5.7)$$

and the position along horizontal axis can be approximated as,

$$Z = [R \cdot \sin\chi - R \cdot \sin(\chi - \tau) - X] \times \frac{\tan\psi}{\sin(\theta + \chi + \tau)} + h \quad (5.8)$$

where  $R$  is the radius of curvature (2020 mm for FOCAL1),  $\chi$  is the asymmetry angle ( $2^\circ$ ),  $\tau$  is the ratio of the crystal footprint to the source-to-crystal distance = 2.25,  $h = CD$  or  $CE$  in Fig. 5.20 ( $= \pm 20$  mm).  $\psi = \psi_1 = \psi_2 = \pm 1.9076^\circ$  and  $\theta$  is the Bragg angle. The predicted energies of the Ly  $\alpha_1$  and Ly  $\alpha_2$  lines from  $Pb^{81+}$  in the emitter frame are 77934.25 eV and 75280.47 eV respectively [43]. The velocity of the source is  $\beta = 0.5864$ . From these values and using the Doppler formula 5.1, the wavelengths  $\lambda_1$  and  $\lambda_2$  can be derived for the angles  $90^\circ + \psi$  and  $90^\circ - \psi$ , respectively, and the corresponding Bragg angles  $\theta_1$  and  $\theta_2$  (see the Fig. 5.20 for  $\theta_1$  and  $\theta_2$ ). Thereby, for the two different Bragg angles the vertical positions  $X_1$  and  $X_2$  and the horizontal positions  $Z_1$  and  $Z_2$  are obtained using equations 5.7 and 5.8. Hence the slope of the line (GOH in Fig. 5.20) is given by  $\frac{X_2 - X_1}{Z_2 - Z_1}$ . The estimated Doppler rotation of the Ly  $\alpha_1$  line is 0.0232 radian. The measured slope of Ly  $\alpha_1$  with respect to the calibration line is  $0.0234 \pm 0.0002$  rad, which is in good agreement with the estimation. The measured difference of the slopes of the Ly  $\alpha_1$  and Ly  $\alpha_2$  lines is  $0.0017 \pm 0.0003$  rad. The estimated slope difference is 0.0012. A small difference between the measured and estimated values is due to the fact, that the calculation was done for a Ly  $\alpha_2$  energy of 75280.47 eV, whereas the observed line is a blend of two different transitions, the  $2p_{1/2}$  to  $1s_{1/2}$  E1 and  $2s_{1/2}$  to  $1s_{1/2}$  M1 transitions, respectively.

The 2D detector was rotated at the beginning of the measurement keeping in mind the Doppler rotation of the Lyman lines. If the line stays on several strips due to Doppler rotation then the data analysis becomes too lengthy for summing up split events. After tilting the detector the Lyman lines stayed on 1 or 2 strips, which made the analysis easier.

## 5.4 The Data Analysis and Interpretation of FOCAL2(1D) Spectrometer

The strips on the front side of the 1D detector are horizontal so that the strip number denotes the position along the axis of dispersion. Like in FOCAL1, in this case also the upper reflections from the crystal were used for sake of stable operation throughout the beam-time. The calibration spectrum shown in Fig. 5.22, was obtained integrating all the reasonable files accumulated during the

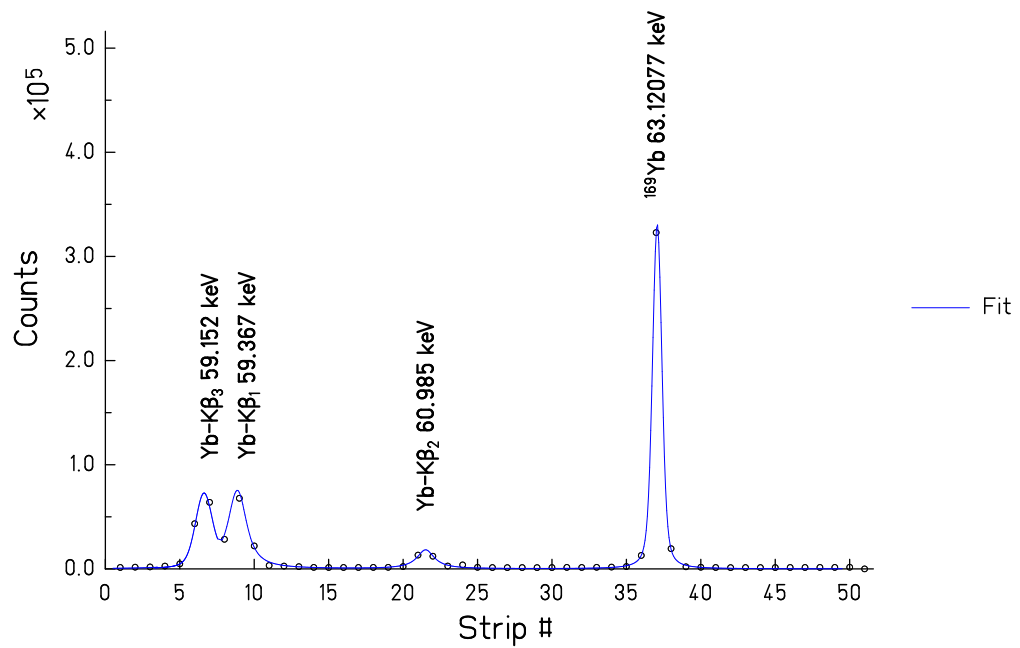


Figure 5.22: The calibration spectrum obtained from FOCAL2 by integrating all reasonable data files accumulated during the beam-time. Voigt profiles were fitted and are denoted by the solid curves. The 63.121 keV line was used to calibrate the spectrometer. The very weak line of  $\text{Yb-K}\beta_2$  is also noticeable because of having good resolution and almost no background photon.

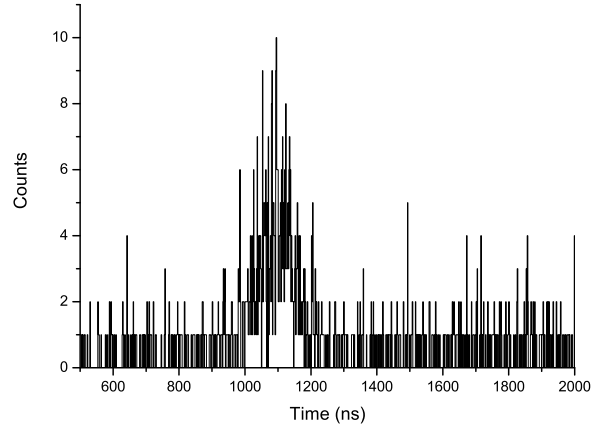


Figure 5.23: The coincidence time spectrum between the 1D detector and the particle detector.

beam-time. Even the weakest line  $\text{Yb-K}\beta_2$  at 60.985 keV is visible, which is very difficult to observe with a normal solid state detector because of low resolution and background photons. The calibration line (i.e., the 63.121 keV line) stays almost on one strip (#37).

The coincidence time spectrum between the 1D detector and the particle detector is shown in Fig. 5.23. The FWHM of the time spectrum is about 120 ns, which is the convolution of the time resolutions of the 1D detector of about 70 ns [66] and the particle detector of less than 90 ns [86].

The pulse-height spectrum of the online measurement shown in Fig. 5.24 exhibits the same kind of features as that of the FOCAL1 spectrometer. A pulse-height spectrum was generated (see Fig. 5.25), where the positions of the Lyman line pulse-height spectra are plotted along the X-axis, which indicates the resolution of FOCAL2 and along the Y-axis the energy of pulse-height spectrum is plotted, which shows the resolution of the 1D detector.

In principle the 1D detector also shows charge sharing between two neighbor strips. However, no evidence of multi-hit events was found. Fig. 5.26 shows the pulse-height spectrum of split events from the Yb 63.121 keV photons between strip number 36 and 37. The energy was reconstructed by summing up split charges event by event, which is shown in the filled area of this pulse-height spectrum. From Fig. 5.26 it can be seen that many high energetic split events in strip # 37 and many low energetic events occur in strip # 36. The reason will be apparent if one looks back to Fig. 5.22, where the majority of the 63.121 keV photons are hitting strip # 37 or close to it. Therefore, most of the split charges appear on strip # 37 and less amount of split charges on # 36 and the strips show the energies which are proportional to the number of collected charges. The

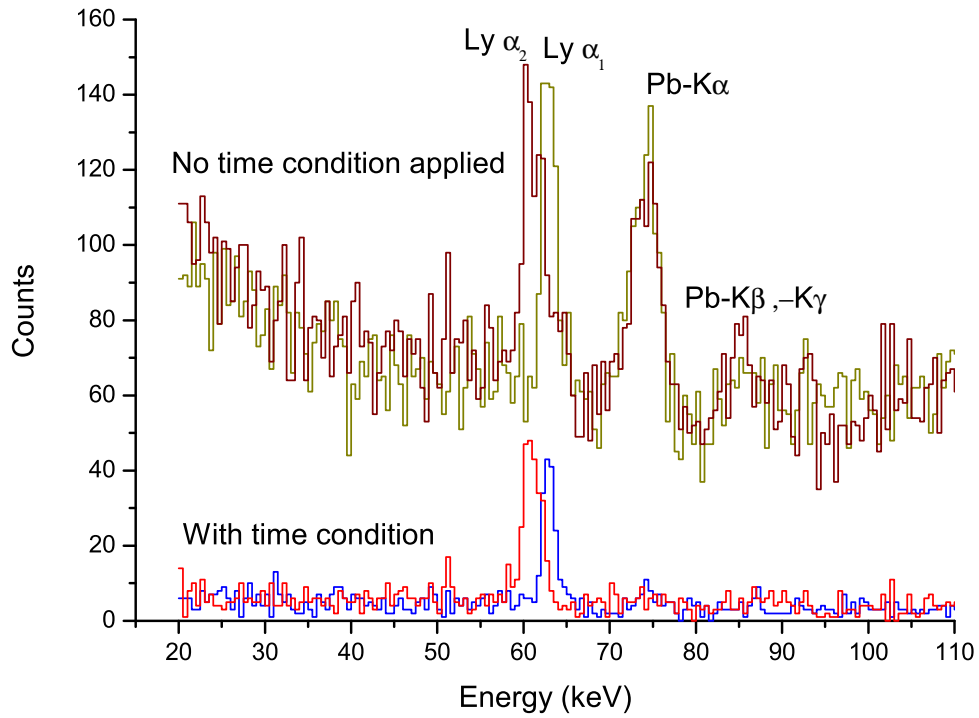


Figure 5.24: The pulse-height spectra of different strips of the 1D detector obtained in the online measurement are merged in one picture.

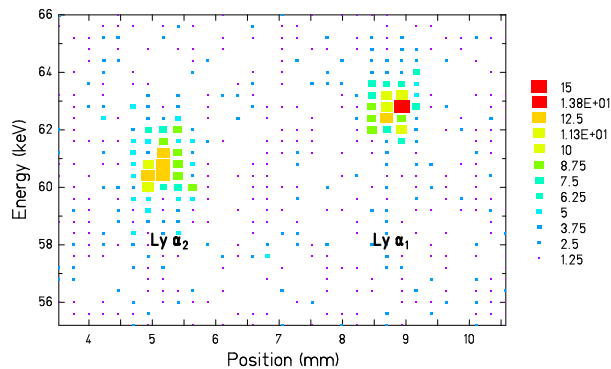


Figure 5.25: The pulse-height spectrum of  $\text{Ly } \alpha_1$  and  $\text{Ly } \alpha_2$  lines from  $\text{Pb}^{81+}$  with proper time condition. The positions of the lines along the X-axis indicate the resolution of the spectrometer, whereas the energy along the Y-axis shows the resolution of the 1D detector.

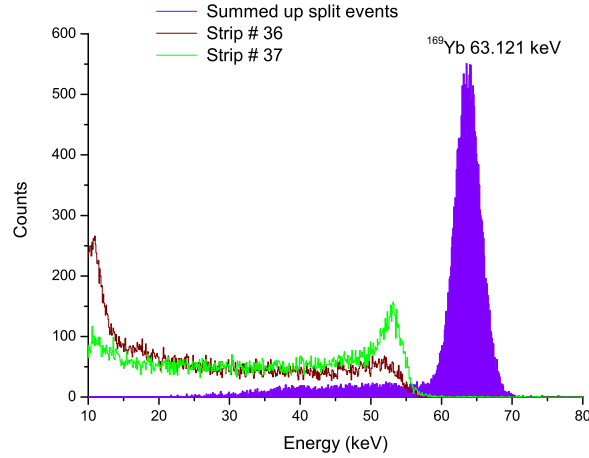


Figure 5.26: The split events of 63.121 keV calibration photons between strip # 36 and 37 are shown in the unfilled part of the pulse-height spectrum and the energies of such events range from 10 keV to 55 keV. The event by event summed spectrum is shown by the filled area.

summed-up spectrum shows a smaller contribution of escape photon as compared to the 2D detector. This is because the effective volume of one pixel for the 1D detector is larger compared to that of the 2D detector. The Fig. 5.27 shows a plot of the split energies between strip number 36 and 37. A consistent 63.121 keV line is the sign of no charge loss for any event in the gap.

The split events of the Lyman lines have been reconstructed in the same way as discussed in case of the 2D detector. The comparison of the intensity distributions between single-hit and double-hit events in the strips is shown in Fig. 5.28. The number of double-hit events is 18.5% and 16.5% for Ly  $\alpha_1$  and Ly  $\alpha_2$  lines, respectively. The intensity distribution of the total number of reasonable hits of Ly  $\alpha_1$  and Ly  $\alpha_2$  photons is shown in Fig. 5.29. A least square fitting was performed using a Gauss function.

## 5.5 The Energy Centroid Determination of the Ly $\alpha_1$ line

In order to obtain the energy centroid of the Ly  $\alpha_1$  line, one needs to determine at first the wavelength centroid using the dispersion relation of the spectrometer. Due to the Bragg condition the higher energetic x-rays will be reflected at smaller angles from the crystal, thus they appear closer to the optical axis. For example, Ly  $\alpha_1$  photons hit the detector closer to the optical axis than Ly  $\alpha_2$  photons. The Ly  $\alpha_1$  line hits a strip on the detector at a distance  $X_L$  from the optical

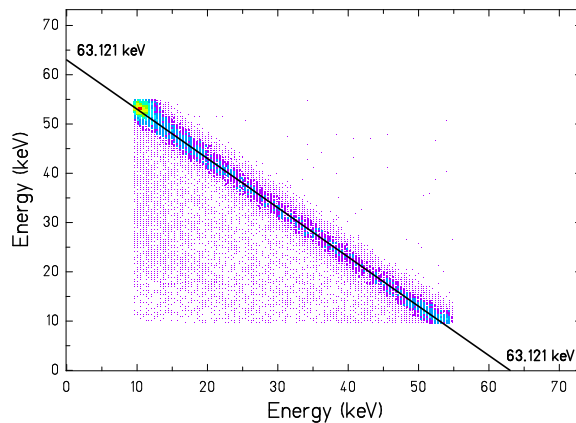


Figure 5.27: The split energies of strip number 36 are plotted along the x-axis and the same for strip number 37 along the y-axis. A consistent 63.121 keV line shows that there was no charge loss in the groove between strip number 36 and 37.

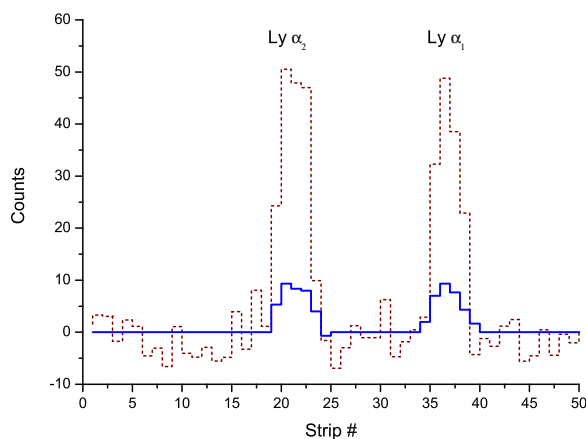


Figure 5.28: The intensity distributions in the strips of the one-dimensional detector for single-hit events (dotted line) and double-hit events (solid line).

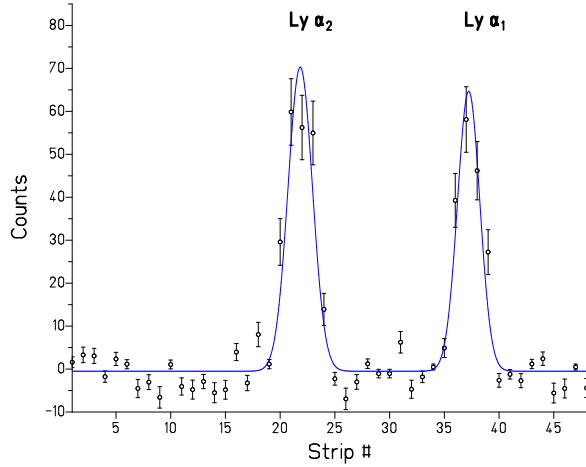


Figure 5.29: The total number of reasonable counts of the Lyman lines is plotted. A least square fitting was done using a Gauss profile (shown by the solid curve).

axis and this is given by  $X_L = C + S_l \cdot W$ , where  $S_l$  is the strip number of the Ly  $\alpha_1$  centroid,  $W$  is the effective strip width, which is the sum of the active width and the gap width and  $C$  is the distance of that strip from optical axis. Similarly, the position of the calibration line on the detector plane can be written as,  $X_y = C + S_y \cdot W$ , where  $S_y$  is centroid of calibration line in terms of the strip number. Therefore, the position of the Ly  $\alpha_1$  line relative to the calibration line is given by  $(X_y - X_L) = (S_y - S_l) \cdot W$ . If we substitute the X's by the corresponding wavelengths using the dispersion relation 4.4, we obtain,

$$\lambda_L = \frac{2d}{R} \cdot (S_l - S_y) \cdot W + \lambda_y \quad (5.9)$$

where  $\lambda_L$  is the wavelength centroid of the Ly  $\alpha_1$  line and  $\lambda_y$  is the wavelength centroid of the calibration line.

### 5.5.1 The FOCAL1(2D) Spectrometer

The 2D detector was aligned in such a way that the axis of rotation of the Lyman lines passes through the middle of the detector, i.e., through the middle of the vertical strip number 24. The axis of rotation is defined by an imaginary axis, which makes a  $90^0$  angle with respect to the beam-axis and the Lyman lines of the fast ion-beam make a Doppler rotation centering that axis (e.g., an axis, which passes through the point O and parallel to the optical axis ABF in Fig. 5.20). The ion-beam velocity was chosen  $\beta = 0.58647(2)$  estimating the Doppler shift of the Ly  $\alpha_1$  emitter energy of 63.121 keV at  $90^0$  angle with respect to the beam axis (the reason for choosing this particular energy has been explained at

the beginning of this chapter). Therefore, the position of the Ly  $\alpha_1$  line on this axis of rotation should provide the energy or wavelength centroid of the line from the dispersion relation. Note that the optical axis of the spectrometer and the axis of rotation of the Lyman lines stayed on the same vertical plane (e.g., points F and O in Fig. 5.20), that means the middle of the detector was placed on the optical axis.

In the data analysis section of FOCAL1, the linear fit of the centroids of the Ly  $\alpha_1$  and of the calibration line has been mentioned (refereing to the Fig. 5.8, 5.19 and the equation 5.6 ). For  $x = 24.5$  (the middle of the detector) and from the fitting parameters, the centroid positions of the Ly  $\alpha_1$  line and the calibration line in terms of strip number was obtained, i.e.,  $S_L = 92.766 \pm 0.026$  and  $S_y = 92.6401 \pm 0.0014$ . Plugging these values into Eq. 5.9 and taking  $R = 2.02$  m,  $2d = 384.031 \times 10^{-12}$  m,  $W = 278$   $\mu\text{m}$  and  $\lambda_y = (19.642376 \pm 0.000028) \times 10^{-12}$  m, we obtain the centroid wavelength of the Ly  $\alpha_1$  line in the lab frame  $\lambda_{2D}^{lab} = 19.635695 \times 10^{-12}$  m. Note that the conversion from energy to wavelength or vice versa was done using the value of  $h = 6.6260693(11) \times 10^{-34}$  J s,  $c = 2.99792458 \times 10^8$  m/s and 1 eV corresponds to  $1.60217653(14) \times 10^{-19}$  J [87].

### 5.5.2 The FOCAL2(1D) Spectrometer

The centroid determination of the Ly  $\alpha_1$  line for this spectrometer is rather straight forward, because the centroid positions of the Ly  $\alpha_1$  line and the calibration line in terms of strip number can be directly obtained from the fit of the corresponding one-dimensional intensity distributions (refereing to the Fig. 5.22 and Fig. 5.29). Therefore, we have  $S_L = 37.647 \pm 0.080$  and  $S_y = 37.5704 \pm 0.0023$ . The effective strip width of 1D detector is  $W = 235$   $\mu\text{m}$ ,  $2d = 384.031 \times 10^{-12}$  m,  $R = 2.05$  m and  $\lambda_y = (19.642376 \pm 0.000028) \times 10^{-12}$  m. Plugging these values into Eq. 5.9, we obtain the wavelength centroid of the Ly  $\alpha_1$  line,  $\lambda_{1D}^{lab} = 19.63899 \times 10^{-12}$  m.

### 5.5.3 The Mean Energy Centroid

The mean centroid wavelength can be obtained from the Doppler color mixing formula

$$\lambda^{em} = \frac{\lambda_{1D}^{lab} + \lambda_{2D}^{lab}}{2\gamma} \quad (5.10)$$

Substituting the values of  $\lambda_{2D}^{lab}$  and  $\lambda_{1D}^{lab}$  and taking  $\gamma = 1.2346$ , we obtain the wavelength centroid of the Ly  $\alpha_1$  line in the emitter frame of reference of the ions, i.e.,  $\lambda^{em} = 15.905630 \times 10^{-12}$  m. Therefore the energy centroid of Ly  $\alpha_1$  in the emitter frame of  $Pb^{81+}$  is 77949.87 eV.

## 5.6 The Estimation of Errors

Beside the statistical errors of the wavelength centroids several systematic errors with substantial contributions to the final uncertainties have to be considered. The systematics, which are included in this thesis are the errors due to the radius of curvature of the crystal, the error of the calibration source energy, the telescope alignment error and the determination of the velocity of the ion beam and the error of the placement of the detectors along the optical axis (i.e., the axis of rotation).

Differentiating Eq. 5.9 using the formula  $\sigma_L^2 = (\frac{\partial \lambda_L}{\partial S_L})\sigma_{sl}^2 + (\frac{\partial \lambda_L}{\partial S_y})\sigma_{sy}^2 + (\frac{\partial \lambda_L}{\partial R})\sigma_R^2 + (\frac{\partial \lambda_L}{\partial \lambda_y})\sigma_y^2$  yields

$$\sigma_L^2 = \left[ \frac{2d \cdot W \cdot (S_y - S_L) \cdot \sigma_R}{R^2} \right]^2 + \left( \frac{2d \cdot W}{R} \right)^2 \cdot (\sigma_{sl}^2 + \sigma_{sy}^2) + \sigma_y^2 \quad (5.11)$$

where  $\sigma_{sl}$  is the statistical error of the Ly  $\alpha_1$  line centroid,  $\sigma_{sy}$  the statistical error of the calibration line centroid in terms of strip numbers and  $\sigma_y$  the error of calibration line energy,  $\sigma_R$  the error of the radius of curvature of the crystal.

In equation 5.4, the first term  $(\frac{\beta \sin \theta}{1 - \beta \cos \theta} \Delta \theta)$  gives the relative error of the laboratory wavelength due to the error in the telescope alignment  $\Delta \theta$  and the second term  $(\gamma^2 \frac{\beta - \cos \theta}{1 - \beta \cos \theta} \Delta \beta)$  in that equation gives the relative error of the lab wavelength due to the error of the velocity of the ion-beam  $\Delta \beta$ . A separate estimation of the uncertainties for FOCAL1 and FOCAL2 is given in the following subsections.

### 5.6.1 The FOCAL1(2D) Spectrometer

1. The values of  $\sigma_{sl}$  and  $\sigma_{sy}$  are 0.026 and 0.0014 respectively (see the values of  $S_L$  and  $S_y$  mentioned in the context of the energy-centroid determination of FOCAL1). The effective strip width  $W = 278$  micron and  $R = 2.02$  m. Hence from the second term of Eq. 5.11 we obtain the statistical error of the wavelength of  $1.41 \times 10^{-15}$  m.
2. The error of the radius of curvature of the crystal is 2% of 2.02 m, i.e.,  $\sigma_R = 0.0404$  m [70]. From the first term of Eq. 5.11, we get an uncertainty of the wavelength of  $0.15 \times 10^{-15}$  m.
3. The 63.121 keV line from  $^{169}\text{Yb}$  source has an error of 0.09 eV [88], which yields an uncertainty of the wavelength of  $0.028 \times 10^{-15}$  m.
4. The telescope alignment had an error of 0.04 mrad in both horizontal and vertical directions. Using the first term of Eq. 5.4 yields a relative error of the lab wavelength of  $0.02345 \times 10^{-3}$  for the horizontal and vertical directions separately. Therefore, multiplying this value with the lab wavelength of  $\lambda = 19.6356$  pm for FOCAL1 the total absolute error of the wavelength due to the telescope alignment of  $0.65 \times 10^{-15}$  m is obtained.

5. The velocity of the ion-beam was inferred from the electron cooler voltage. The high-voltage generator of the electron cooler has been calibrated by the Physikalisch-Technische Bundesanstalt (PTB) and the voltage can be determined with an accuracy better than  $\pm 12\text{V}$  at the voltage setting of 119889 V used in the experiment [89]. The error of the velocity of the ion-beam due to the uncertainty in the cooler voltage can be formulated as  $\Delta\beta = \frac{e\Delta U_e}{\beta\gamma^3 mc^2}$  [50], which yields an error of  $\Delta\beta = 2.12 \times 10^{-5}$ . Therefore, from the second term of Eq. 5.4, one determines the relative error of the laboratory wavelength of  $1.9019 \times 10^{-5}$ . Multiplying this value with the lab wavelength 19.6356 pm an absolute error of  $0.37 \times 10^{-15}$  m due to the uncertainty in the ion beam velocity is obtained.
6. The detector center was aligned along the optical axis with an error of  $\sigma_x = \pm 0.5$  mm along horizontal direction [70]. The Doppler rotation of the Ly  $\alpha_1$  line was measured to be 0.0234(2) rad. Differentiating the equation 5.6 transforms this error along the direction of dispersion as  $\sigma \simeq [X^2\sigma_a^2 + a^2\sigma_x^2]^{1/2}$ , where  $X = (24.5 \times 1192) \mu\text{m}$ ,  $\sigma_a = 0.0002$  rad and  $a = 0.02346$  rad. This yields  $\sigma = 13.04 \mu\text{m}$ . From the energy dispersion of the spectrometer, we have that 1  $\mu\text{m}$  along the axis of dispersion is equivalent to 0.60 eV, which yields an equivalent error of 7.88 eV. Hence the corresponding error of the wavelength in the lab frame is  $2.45 \times 10^{-15}$  m.

Adding all the errors quadratically we get a total error of the wavelength in the laboratory frame of  ${}^{2D}\sigma_{lab} = 2.91 \times 10^{-15}$  m which is equivalent to an error of the energy of  $\frac{h\cdot c \cdot 2D\sigma_{lab}}{2D\lambda_{lab}^2} = 9.36$  eV.

It has been observed that the detector stages (both FOCAL1 and FOCAL2) was displaced vertically as large as 50  $\mu\text{m}$  due to change in weight of the detectors before and after the liquid nitrogen filling. The uncertainty caused by this problem is yet to be evaluated.

### 5.6.2 The FOCAL2(1D) Spectrometer

For a detailed explanation please see the estimation of errors for FOCAL1.

1. The values of  $\sigma_{sl}$  and  $\sigma_{sy}$  are 0.080 and 0.0023 respectively (see the values of  $S_L$  and  $S_y$  mentioned in context of energy centroid determination of FOCAL2). The effective strip width  $W = 235$  micron and  $R = 2.05$  m. Hence from the second term of Eq. 5.11, we obtain a statistical error of the wavelength of  $3.5664 \times 10^{-15}$  m.
2. The error of the radius of curvature of the crystal is 2% of 2.05 m, i.e.,  $\sigma_R = 0.041$  m [70]. From the first term of Eq. 5.11, we get the uncertainty of the wavelength of  $0.06756 \times 10^{-15}$  m.

3. The 63.121 keV line from  $^{169}\text{Yb}$  source has an error of 0.09 eV, which yields an uncertainty of the wavelength of  $0.028 \times 10^{-15}$  m.
4. The telescope alignment had an error of 0.04 mrad for both horizontal and vertical directions, which yields a relative error of laboratory wavelength of  $0.02345 \times 10^{-3}$ . Therefore, for  $\lambda = 19.6389$  pm for the FOCAL2 the total absolute error of the wavelength is  $0.65 \times 10^{-15}$  m.
5. The absolute error on the wavelength in lab frame due the uncertainty in the determination of the velocity of the ion beam was determined in the same way as for FOCAL1, which yields a value of  $0.37 \times 10^{-15}$  m.
6. The 1D detector center was aligned along the optical axis with an error of  $\pm 0.5$  mm and since the Doppler rotation of the Ly  $\alpha_1$  line depends on its emitter energy and the velocity of ion-beam therefore the rotation is  $a = 0.0234$  rad and error on it  $\sigma_a = 0.0002$  rad and for the 1D detector X is 11.7 mm. Using the formulas shown in case of FOCAL1 one obtains the error of the position along the axis of dispersion  $11.93 \mu\text{m}$ . This translates into an error of 7.15 eV and the corresponding wavelength is  $2.22 \times 10^{-15}$  m.

The total error of the wavelength in lab frame is estimated to be  ${}^{1D}\sigma_{lab} = 4.24 \times 10^{-15}$  m and the corresponding energy is  $\frac{h \cdot c \cdot {}^{1D}\sigma_{lab}}{{}^{1D}\lambda_{lab}^2} = 13.65$  eV.

### 5.6.3 The Total Error of the Ly $\alpha_1$ Energy

The total error of the wavelength of the Ly  $\alpha_1$  line in the emitter frame can be obtained by differentiating Eq. 5.10, which yields,

$$\sigma_{\lambda}^{em} = \frac{1}{2\gamma} \cdot [{}^{1D}\sigma_{lab}^2 + {}^{2D}\sigma_{lab}^2 + \left(\frac{{}^{1D}\sigma_{lab}^2 + {}^{2D}\sigma_{lab}^2}{2\gamma}\right)^2 \cdot \sigma_{\gamma}^2]^{1/2} \quad (5.12)$$

where  ${}^{1D}\sigma_{lab}$  is the total error of the wavelength of the Ly  $\alpha_1$  line in the lab frame for FOCAL2,  ${}^{2D}\sigma_{lab}$  the same for FOCAL1 and  $\sigma_{\gamma} = 2.34 \times 10^{-5}$  is the error of the Lorentz factor, which was obtained from the cooler voltage uncertainty. Therefore, substituting all the values yields a total error of the wavelength of the Ly  $\alpha_1$  line in emitter frame of  $\sigma_{\lambda}^{em} = 2.088 \times 10^{-15}$  m. The corresponding energy value is given by  $\sigma_E^{em} = \frac{h \cdot c \cdot \sigma_{\lambda}^{em}}{\lambda_{em}^2} = 10.23$  eV. Therefore, the emitter energy of the Ly  $\alpha_1$  line is  $(77949.87 \pm 10.23)$  eV. The binding energies of  $1s_{1/2}$  and  $2p_{3/2}$  of lead from Dirac theory for a point-like nucleus are  $-101581.34(1)$  and  $-23407.276(3)$  eV respectively [90]. The  $2p_{3/2}$  state has a Lamb shift of  $5.15(1)$  eV [43, 90], which yields the binding energy of this state of  $-23402.12(1)$  eV. The  $1s_{1/2}$  has a Lamb shift of  $244.79(53)$  eV [91], which gives the binding energy of  $-101336.55(52)$  eV. Therefore, the predicted Ly  $\alpha_1$  transition is  $77934.43(52)$  eV.

The errors in the measurement are listed in table 5.1.

Different sources of error	FOCAL2(1D): units are in eV	FOCAL1(2D): units are in eV
1. Statistical error	11.46	4.55
2. Radius of curvature of the crystal	0.21	0.49
3. Yb 63.121 keV line energy	0.09	0.09
4. Telescope alignment	2.09	2.09
5. Velocity of the ion-beam	1.20	1.20
6. Axis of rotation	7.15	7.88
7. Total error	13.65	9.36

Table 5.1: The statistical and the different systematic errors for FOCAL1 and FOCAL2 are presented.

## 5.7 The Energy Dispersion of the Spectrometers

The energy dispersion of the spectrometers was discussed with an example in the previous chapter. A detailed calculation can be found in Ref. [68]. For small angles the inverse of the linear wavelength-dispersion can be approximated as,

$$\left(\frac{\Delta\lambda_{ion}}{\Delta X}\right) = \gamma^{-1} \cdot 2d \cdot \cos\theta \cdot \cos^2\left(\frac{R+2s}{R+s} \cdot \theta\right) \cdot R^{-1} \quad (5.13)$$

where  $s$  is the source-to-crystal distance ( $= 600$  mm). The other symbols have been used before in several occasions. The equation says that, if two x-rays having a wavelength difference of  $\Delta\lambda_{ion}$  emitted by an ion moving with velocity  $\beta$  then they will show up on the detector plane with a distance of  $\Delta X$ . The angle of diffraction  $\theta$  is given by  $\theta = \sin^{-1}\left(\frac{\lambda_{lab}}{2d}\right)$ . For FOCAL1 the lab wavelength is  $\lambda_{lab} = 19.63569$  pm, which yields,  $\theta = 2.9306^\circ$ . Therefore,  $\frac{\Delta\lambda_{ion}}{\Delta X} = 1.2334 \times 10^{-10}$  m/m. So the energy dispersion can be written as  $\frac{\Delta X}{\Delta E_{ion}} = 1.65$  mm/keV. This means  $1 \mu\text{m}$  distance on the detector plane along the direction of dispersion has an energy difference of  $0.6044$  eV.

Similarly, for FOCAL2  $\theta = 2.9313^\circ$ , which yields  $\frac{\Delta\lambda_{ion}}{\Delta X} = 1.2245 \times 10^{-10}$  m/m. Hence, the energy dispersion reads  $\frac{\Delta X}{\Delta E_{ion}} = 1.66$  mm/keV. This means  $1 \mu\text{m}$  distance on the detector plane along the direction of dispersion has an energy difference of  $0.6024$  eV.

A theoretical estimation of the energy-dispersion of about  $1.63$  mm/keV [68, 69] has been obtained, which is in good agreement with the experimental result.

# Chapter 6

## Conclusion and Outlook

In this work we have exploited the FOCAL spectrometers for the first time in a production run to determine the wavelength of the Lyman- $\alpha$  transitions in H-like Pb. Despite the experiment went on according to the plans and anticipations, unfortunately a few systematic problems showed up, which have to be solved before the next run. The largest systematic error is due to the detector stage fluctuation. It has been observed that the detector stage was displaced vertically as large as  $50 \mu\text{m}$  due to change in weight of the detectors before and after liquid-nitrogen filling. The essential systematic error caused by this problem is yet to be evaluated. An uncertainty of  $1 \mu\text{m}$  of the detector position along the axis of dispersion (i.e., in the vertical direction) introduces an error of 0.6 eV. Therefore, the vertical displacements of the detectors are most probably the reason for the discrepancy between the experimental and the theoretical values of the transition energy. A more delicate design of the detector stage needs to be incorporated to increase the stability. The second largest systematic error is the placement of the detectors along the optical axis of rotation of the Lyman line. For the next run a very careful adjustment of the detector center along the optical axis is necessary. Among the other systematics, the telescope alignment error has a significant contribution. It was shown in Fig. 5.3, that at an observation angle of  $90^\circ$ , the error in the energy is large due to the uncertainty in the observation angle. So the small uncertainty in the telescope alignment (0.04 mrad) introduced a significant systematic error. We need more precise alignment of the telescopes in order to reduce this uncertainty to a negligible level. From the Table 5.1, one can see that the statistical error of FOCAL2(1D) is quite large (11.46 eV). The reason is that, the intensity of the Ly  $\alpha_1$  line is distributed over several strips due to the Doppler rotation, which yields a large FWHM of the distribution (see Fig. 5.29). And since the statistical error on the mean position is proportional to the FWHM, FOCAL2(1D) shows a large statistical error. For the 1D detector we cannot solve the broadening problem by turning the detector and placing the Ly  $\alpha_1$  on one strip. This is because, if the 1D detector is tilted, the horizontal calibration line produces broadening in the one dimensional distribution, which

in turn again yields a large statistical error. The only way to get rid of this problem is to reduce the energy of the ion-beam as low as 20 Mev/u, which will yield much less Doppler rotation of the Ly  $\alpha_1$  line and therefore, the intensity splitting as well as the broadening will be reduced. The low beam energy has other advantages. Fig. 5.3 shows that the uncertainties of emitter energy due to the observation angle ( $\Delta\theta$ ) and the velocity ( $\Delta\beta$ ) at a low beam energy ( $\leq 20$  Mev/u) is much less compared to the energy we used in this experiment (i.e., 218.54 Mev/u). Also the intensity of the Lyman lines will be increased at this energy due to the reduction of direct capture into the K-shell of the bare ion, despite 10 times less number of ions stored due to the deceleration of the ion beam [89].

Last but not least, in order to achieve an uncertainty of  $\pm 1$  eV or below in such an experiment an improvement of the electronics concerning the detector position (strip) response function is needed with the option to subdivide more accurately the strip width. With the current electronics the intensity spectrum of the photons appears to one strip, i.e., the position of the photon hit is uncertain by one strip width. Therefore, even if we have a large number of events hitting only on one part of a strip, still the width of the intensity distribution is limited to one strip. For example, the spatial width of the spot of a 63 keV calibration line is estimated to be 100  $\mu\text{m}$ , which is less than the half of a strip width [69]. A development of the digital signal processing is going on to take an edge to this problem. At this point one may wonder that despite such electronic resolution, how one could determine the position sensitivity down to 50  $\mu\text{m}$ . This will be apparent if one looks back to the Fig. 4.16, where every peak consists of at least two data points in the intensity distribution. Therefore, the peak centroid was determined by the intensity ratio of these data points. If one looks carefully to the data points for each peak from left to right, one notices that with shifting the position of the detector along the axis of dispersion, the intensity distribution of the spectral line over the neighbor strips was changing and as a result the left data points of a peak are going down and the right data points moving up. Hence the position sensitivity down to 50  $\mu\text{m}$  could be determined by virtue of intensity splitting.

# Bibliography

- [1] S. Bourzeix, B. de Beauvoir, F. Nez, M. D. Plimmer, F. de Tomasi, L. Julien, F. Biraben, and D. N. Stacey Phys. Rev. Lett. **76** (1996) 384.
- [2] Th. Udem, J. Reichert, R. Holzwarth, and T. W. Hänsch Phys. Rev. Lett. **82** (1999) 3568.
- [3] B. Franzke, Nucl. Inst. Meth. B **24/25** (1987) 18.
- [4] B. Franzke, Phys. Scr. T **22** (1988) 41.
- [5] R.E. Marrs, Adv. At. Mol. Phys., **27** (1991) 57.
- [6] A. Gumberidze, Th. Stöhlker, D. Banas, K. Beckert, P. Beller, H. F. Beyer, F. Bosch, S. Hagmann, C. Kozhuharov, D. Liesen, F. Nolden, X. Ma, P. H. Mokler, M. Steck, D. Sierpowski, and S. Tashenov, Phys. Rev. Lett. **94** (2005) 223001.
- [7] M. Jammer, The Conceptual Development of Quantum Mechanics, New York: McGraw-Hill, 1966
- [8] S. S. Schweber, QED and the Men Who Made it: Dyson, Feynman, Schwinger, and Tomonaga, Princeton University Press, Princeton (1994).
- [9] R. Eisberg and R. Resnick, Quantum Physics of Atoms, Molecules, Solids, Nuclei, and Particle, John Wiley and Sons (1974).
- [10] C.D. Anderson, Phys. Rev. **43** (1933) 381A.
- [11] O. Betz, Ann. d. Physik **15** (1932) 321.
- [12] T. Hasse, Ann. d. Physik **23** (1935) 675.
- [13] W. E. Lamb and R. C. Retherford. Fine structure of the hydrogen atom by a microwave method. Phys. Rev. **72** (1947), 241-243.
- [14] H. A. Bethe. The electromagnetic shift of energy levels. Phys. Rev. Lett. **91** (1947), 339-341.

- [15] A. Surzhykov, S. Fritzsche, A. Gumberidze, and Th. Stöhlker, *Phys. Rev. Lett.* **88** (2002) 153001.
- [16] H.F. Beyer and V.P. Shevelko, *Introduction to the Physics of Highly Charged Ions*, IOP (2003).
- [17] R.Marrus, *Physics of Highly-Ionized Atoms*, NATO ASI Series B: Physics Vol. 201, Plenum Press, 1989.
- [18] P.J. Mohr, *Ann. Phys.* **88**, 26, (1974); **88**, (1974) 52.
- [19] P.J. Mohr, *Phys. Rev. A* **46**, (1992) 4421.
- [20] P. Indelicato, and P.J. Mohr, *Phys. Rev. A* **58**, (1998) 165.
- [21] P.J. Mohr, and G. Soff, *Phys. Rev. Lett.* **70**, (1993) 158.
- [22] V.A. Yerokhin, and V.M. Shabaev, *Phys. Rev. A* **60**, (1999) 800.
- [23] V.A. Yerokhin, V.M. Shabaev, *Phys. Lett. A* **210**, (1996) 437.
- [24] T. Beier, Private communication.
- [25] G. Soff, and P.J. Mohr, *Phys. Rev. A* **38**, (1988) 5066.
- [26] H. Persson, I. Lindgren, S. Salomonson, and P. Sunnergren, *Phys. Rev. A* **48**, (1993) 2772.
- [27] N.L. Manakov, A.A. Nekipelov, and A.G. Fainshtein, *Zh. Eksp. Teor. Fiz.* **95**, (1989) 1167 [*Sov. Phys. JETP* **68**, (1989) 673].
- [28] A.N. Artemyev, V.M. Shabaev, V.A. Yerokhin *J. Phys. B* **28** (1995) 1884.
- [29] V.A. Yerokhin, A. N. Artemyev, P. Indelicato and V. M. Shabaev , *Nucl. Inst. Meth. B* **205** (2003) 47.
- [30] G. Soff, T. Beier, and C. Hoffmann, *Acta Phys. Pol. B* **27** (1996) 369.
- [31] A. Mitrushenkov, L. Labzowsky, I. Lindgren, H. Persson, and S. Salomonson, *Phys. Lett. A* **200** (1995) 51
- [32] S. M. Schneider, W. Greiner, G. Soff, *J. Phys. B* **26** (1993) L529.
- [33] H. Persson, L. Labzowsky, I. Lindgren, T. Beier, G. Plunien, and G. Soff, *Phys. Rev. A* **54** (1996) 2805.
- [34] S. Mallampalli and J. Sapirstein, *Phys. Rev. A* **54**, (1996), 2714.
- [35] M. I. Eides, H. Grotch, and V. A. Shelyuto. Theory of light hydrogenlike atoms. *Phys. Rep.* **342** (2001), 63.

- [36] T. Beier, P. J. Mohr, H. Persson, G. Plunien, M. Greiner and G. Soff, *Physics Letters A* **236** (1997) 329.
- [37] V.M. Shabaev, *Theor. Math. Phys.* **63** (1985) 588.
- [38] V.M. Shabaev, *Phys. Rev. A* **57** (1998) 67.
- [39] V.M. Shabaev, A. N. Artemyev, T. Beier, G. Plunien, V. A. Yerokhin, and G. Soff, *Phys. Rev. A* **57** (1998) 4235.
- [40] G. Plunien, and G. Soff, *Phys. Rev. A* **51**, 1119 (1995); **53** (1996) 4614.
- [41] A.V. Nefiodov, L.N. Labzowsky, G. Plunien, and G. Soff, *Phys. Lett. A* **222** (1996) 227.
- [42] P.J. Mohr, *At. Data and Nucl. Data Tables* **29** (1983) 453.
- [43] W.R. Johnson and G. Soff, *At. Data and Nucl. Data Tables* **33** (1985) 405.
- [44] M. Niering, R. Holzwarth, J. Reichert, P. Pokasov, Th. Udem, M. Weitz, T. W. Hänsch, P. Lemonde, G. Santarelli, M. Abgrall, P. Laurent, C. Salomon, and A. Clairon, *Phys. Rev. Lett.* **84** (2000) 5496.
- [45] H.F. Beyer, H.-J. Kluge, and V.P. shevelko, *X-ray Radiation of Highly Charged Ions*, Springer Ser. Atoms Plasmas, Vol. 19, Springer, Berlin, Heidelberg, 1997.
- [46] H. Persson, S. Salomonson, P. Sunnergren, I. Lindgren, M.G.H. Gustavsson, *Hyperfine Interaction* **108** (1997) 3.
- [47] H. Persson, I. Lindgren, L. Labzowsky, G. Plunien, T. Beier, G. Soff, *Phys. Rev. A*, in print.
- [48] Th. Stöhlker, *et al.* GSI scientific report 1997 (1998) 99.
- [49] Th. Stöhlker P.H. Mokler, K. Beckert, F. Bosch, H. Eickhoff, B. Franzke M. Jung, T. Kandler, O. Klepper, C. Kozhuharov, R. Moshhammer, F. Nodeln, H. Reich, P. Rymuza, P. Spaedtke, and M. Steck, *Phys. Rev. Lett.* **71** (1993) 2184.
- [50] H.F. Beyer, G. Menzel, D. Liesen, A. Gallus, F. Bosch, R.D. Deslattes, P. Indelicato, Th. Stoehlker, O. Klepper, R. Moshhammer, F. Nodeln, H. Eickhoff, B. Franzke, and M. Steck, *Z. Phys D* **35** (1995) 169.
- [51] Th. Stöhlker, P.H. Mokler, F. Bosch, R.W. Dunford, O. Klepper, C. Kozhuharov, T. Ludziejewski, B. Franzke, F. Nolden, H. Reich, P. Rymuza, Z. Stachura, M. Steck, P. Swiat, and A. Warczak, *Phys. Rev. Lett.* **85** (2000) 3109.

- [52] J.P. Briand, P. Chevallier, P. Indelicato, K.P. Ziock, and D. Dietrich, *Phys. Rev. Lett.* **65** (1990) 2761.
- [53] J.H. Lupton, D.D. Dietrich, C.J. Hailey, R.E. Stewart, K.P. Ziock, *Phys. Rev. A* **50** (1994) 2150.
- [54] A. Gumberidze, Dissertation University Frankfurt, GSI-DISS 2003-07
- [55] V.A. Yerokhin and V.M. Shabaev, *Phys. Rev. A* **64** (2001) 062507-1.
- [56] Dr. A. Gumberidze, private communication.
- [57] O.C. Brinzaescu, Dissertation University Heidelberg, GSI-DISS 2000-13 (2002)
- [58] Markus Czanta, Dissertation University Heidelberg, GSI-DISS 2001-12.
- [59] A. R. Sohval, J. P. Delvaille, K. Kalata, K. Kirby-Docken and H. W. Schnopper, *J. Phys B* **9** (1976) L25.
- [60] Th. Stöhlker, T. Ludziejewski, H. Reich, F. Bosch, R.W. Dunford, J. Eichler, B. Franzke, C. Kozhuharov, G. Menzel, P.H. Mokler, F. Nolden, P. Rymuza, Z. Stachura, M. Steck, P. Swiat, A. Warczak und T. Winkler, *Phys. Rev. A* **58** (1998) 2043.
- [61] Th. Stöhlker, Habilitationsschrift Universität Frankfurt (1998)
- [62] Th. Stöhlker, *Phys. Rev. A* **58** (1998) 2043.
- [63] J. Eichler, *Phys. Rev. A* **32** (1985) 112.
- [64] M. Stobbe, *Ann. Phys.* **7** (1930) 661.
- [65] P.H. Mokler, S. Reusch, Th. Stöhlker, R. Schuch, M. Schulz, G. Wintermeyer, Z. Stachura, A. Warczak, A. Mueller, Y. Awaya und T. Kambara, *Radiation Effects and Defects in Solids*, Vol. **110** (1989) 39.
- [66] Protic, D, Stöhlker, T.; Ebeyer, H.F.; Bojowald, J.; Borchert, G.; Gumberidze, A.; Hamacher, A.; Kozhuharov, C.; Ma, X.; Mohos, I, *IEEE Trans. Nucl. Meas* **48** (2001) 1048.
- [67] T. Stöhlker, P. H. Mokler, F. Bosch, R. W. Dunford, F. Franzke, O. Klepper, C. Kozhuharov, T. Ludziejewski, F. Nolden, H. Reich, P. Rymuza, Z. Stachura, M. Steck, P. Swiat, and A. Warczak, *Phys. Rev. Lett.* **85** (2000) 3109 and references therein.
- [68] H.F. Beyer *Nucl. Inst. Meth. A* **400** (1997) 137.

- [69] H.F. Beyer, Th. Stöhlker, D. Banas, D. Liesen, D. Protic, K. Beckert, P. Beller, J. Bojowald, F. Bosch, E. Förster, B. Franzke, A. Gumberidze, S. Hagmann, J. Hoszowska, P. Indelicato, O. Klepper, H.-J. Kluge, St. Koenig, Chr. Kozhuharov, X. Ma, B. Manil, I. Mohos, A. Oršic-Muthig, F. Nolden, U. Popp, A. Simionovici, D. Sierpowski, U. Spillmann, Z. Stachura, M. Steck, S. Tachenov, M. Trassinelli, A. Warczak, O. Wehrhan and E. Ziegler, *Spectrochim. Acta. Part B* **59** (2004) 1535.
- [70] Dr. Heinrich Beyer, private communication.
- [71] S. Chatterjee, H.F. Beyer, D. Liesen, Th. Stöhlker, A. Gumberidze, Chr. Kozhuharov, D. Banas, D. Protic, K. Beckert, P. Beller, Th. Krings, F. Bosch, B. Franzke, S. Hagmann, J. Hoszowska, P. Indelicato, H.-J. Kluge, X. Maj, B. Manil, I. Mohos, F. Nolden, U. Popp, A. Simionovici, D. Sierpowski, M. Steck, U. Spillmann, C. Brandau, E. Förster, Z. Stachura, S. Tashenov, M. Trassinelli, A. Warczak, O. Wehrhan, E. Ziegler, S. Trotsenko and R. Reuschl, *Nucl. Inst. Meth. B* **245** (2006) 67-71.
- [72] Protic, D.; Stöhlker, T.; Krings, T.; Mohos, I.; Spillmann, U, *IEEE Trans. Nucl. Meas* **52** (2005) 3194.
- [73] D. J. Skyrme, *Nucl. Inst. Meth.* **57** (1967) 61.
- [74] W.R. Leo *Techniques For Nuclear and Particle Physics Experiments*, Springer-Verlag (1994).
- [75] R.A. Kroeger, N. Gehrels, W. N. Johnson, J. D. Kurfess, B. P. Philips and J. Tueller, *Nucl. Inst. Meth. A* **422** (1999) 206.
- [76] B. Hyams and U. KoetzE. Belau, R. Klanner, G. Lutz, E. Neugebauer and A. WylieJ. Kemmer, *Nucl. Inst. Meth.* **205** (1983) 99.
- [77] E. Gatti and P.Rehak, *Nucl. Inst. Meth.* **225** (1984) 608.
- [78] Pavel Rehak, Emilio Gatti, Antonio Longoni, J. KemmerPeter Holl, Robert Klanner, Gerhard Lutz and Andrew Wylie, *Nucl. Inst. Meth. A* **235** (1985) 224.
- [79] D. Protic *et al.*, *IEEE Trans. Nucl. Meas* **32** (1985) 553.
- [80] D. Protic and T. Krings, *IEEE Trans. Nucl. Meas* **50** (2003) 998.
- [81] D.R. Dance and G.J. Day, *Phys. Med. Biol.*, **30** (1985) 259-262.
- [82] J.L. Campbell and P.L. Mcghee, *Nucl. Inst. Meth. A* **248** (1986) 393-404.
- [83] Dr. Ina Pschorn, private communication.

- [84] P. Egelhof, H. F. Beyer, D. McCammon, F. V. Feilitzsch, A. V. Kienlin, H. -J. Kluge, D. Liesen, J. Meier, S. H. Moseley and T. Stöhlker. *Inst. Meth. A* **370** (1996) 263.
- [85] Prof. Th. Stoehlker, private communication.
- [86] Dr. Chr. Kozhuharov, private communication.
- [87] NIST Standards for Fundamental Physical Constants. URL <http://physics.nist.gov/cuu/Constants/index.html>
- [88] URL <http://www.nndc.bnl.gov/decaysearchdirect.jsp?nuc=169YB>
- [89] Dr. Markus Steck, private communication.
- [90] Dr. Eric-Olivier Le Bigot, private communication.
- [91] V.A. Yerokhin, P. Indelicato, and V.M. Shabaev, *Eur. Phys. J. D* **25** (2003) 203.

# Acknowledgements

My first and deepest gratitude goes to Prof. H.-J.Kluge for giving me the opportunity to pursue the research work at world-class laboratory in GSI, and providing me the financial and the moral support through out the thesis work.

For the direct supervision of my PhD work, I am grateful to Prof. Dieter Liesen, from whom I have learnt deepest concepts of physics and always received myriads of encouragements. This work was possible for his supports and suggestions in the crucial moments.

A very special thank to Dr. Heinrich Beyer, for his vital contributions to this thesis work. It was really a pleasure to work with him and I have learnt many useful things, which gave me enormous confidence in the field of physics and technology.

I am very much thankful to Prof. Thomas Stöhlker for his unconditional helps and very important contributions, which played a key role to accomplish this work.

Behind the success of this experiment a team work is greatly acknowledged. I would like to thank my colleagues Dr. D. Banas, Dr. C. Kozhuharov, Dr. X. Ma, Prof. S. Hagmann, Prof. F. Bosch, Prof. P. Indelicato, U. Spillman, Dr. A. Gumberidze, S. Hess, Dr. B. Manil, R. Reuschl, M. Trassinelli, D. Attia and S. Trotsenko. I am also thankful to Dr. Eric-Olivier Le Bigot, Dr. K.-H. Schmidt, Dr. M. Steck, Dr. T. Beier, Dr. C. Brandau, I. Massmann, W. Enders, H. Wesp and D. Racano for vital contributions. I apologize to them who are not in the list of names, but I would like to convey my gratitude to all of them, especially to the collaborators of this project.

I am grateful to Prof. B.P. Das for introducing me to the field of atomic physics and its applicability.

Besides the PhD work I enjoyed a wonderful social life through out this period with many great friends: Alex, Serge, Regina, Sebastian, Stanislav, Christopher, Adam, Shadi, Farouk, Muaffaq, Giorgios, Davide, Kripa, Sarla, Supriya, Ankur, Manas, Saidur, Bijaya, Shashi, S. Mandal, R. Palit, P. Verma, U.D. Paramanik, Dina, to whom I am grateful.

Behind the curtain and far-off from here the people who always comforted me and gave me moral support, my parents, brother and my fiance, I dedicate this work to them.